Fakultät für Elektrotechnik und Informationstechnik

Optimisation Model of Intelligent Charging Strategies for Battery Electric Vehicles Considering the Power System and Battery Ageing

Annette Erika Trippe

Vollständiger Abdruck der von der Fakultät für Elektrotechnik und Informationstechnik der Technischen Universität München zur Erlangung des akademischen Grades eines

Doktor-Ingenieurs (Dr.-Ing.)

genehmigten Dissertation.

Vorsitzender: Prof. Dr.-Ing. Markus-Christian Amann

Prüfende der Dissertation:

1. Prof. Dr. rer. nat. Thomas Hamacher
2. Associate Prof. Hoay Beng Gooi, Ph. D. (nur schriftliche Beurteilung)
3. Prof. Dr.-Ing. Andreas Jossen (nur mündliche Prüfung)

Die Dissertation wurde am 31.05.2017 bei der Technischen Universität München eingereicht und durch die Fakultät für Elektrotechnik und Informationstechnik am 29.11.2017 angenommen.

Abstract

The emergence and upswing of battery electric vehicles fuels discussion and research on the impact of those on the power system and how they can be used beneficially. On the other hand, the battery is very sensitive to different modes of operation and can age rapidly. This can lead to high losses in value of the electric vehicle because the battery accounts for a substantial share in the cost.

In this work, an optimisation model is developed in order to generate intelligent charging strategies for battery electric vehicles. The model considers both electricity price and battery ageing and thereby allocates charging strategies representing the optimal trade-off between electricity price controlled charging and battery lifetime.

A mobility model is elaborated to simulate the energy consumption of the respective vehicles as well as the driving and parking schedules of the users. The simulated travel schedules and energy consumption serve as input for the optimisation model of intelligent charging strategies.

Experimental data of battery ageing tests, designed to mirror the operation of lithium-ion batteries in electric vehicles, are the basis for a comprehensive battery ageing model. Both cycle and calendar ageing are examined and the influence of the state of charge, charge rate, as well as range of operation on battery ageing is investigated. A calendar ageing function as well as a three-dimensional cycle ageing function are derived, modelling the battery ageing within the optimisation.

The charging optimisation model minimises the total charging costs, consisting of charging electricity cost and battery ageing cost. The mathematical optimisation problem is initially formulated as a mixed-integer non-linear programme and transformed into a mixed-integer linear programme by means of piecewise linear approximation and other linearisation techniques.

The charging optimisation model is applied to a sample of 300 battery electric vehicles and different scenarios are computed and analysed. The battery ageing cost accounts for 13 % to 45 % of the total charging costs for the different scenarios, underlining the importance of the inclusion of battery ageing into the optimisation of charging strategies. The optimal operating range lies between a battery state of charge of 10 % to 50 % in most cases. Charging times coincide with times of low electricity prices, usually correlated to valleys in the electricity demand. Almost no fast charging is applied, indicating that the higher battery ageing cost due to fast charging cannot be outweighed by a reduction in electricity cost when charging more energy during low-priced periods.

Zusammenfassung

Das Aufkommen und die Verbreitung von Elektrofahrzeugen treiben Diskussionen und Forschungsaktivitäten an, wie Elektrofahrzeuge das Stromsystem beeinflussen und wie sie dafür vorteilhaft eingesetzt werden können. Andererseits reagieren die Batterien von Elektrofahrzeugen sehr sensibel auf verschiedene Betriebsmodi und können schnell altern. Dies kann zu hohen Wertverlusten der Fahrzeuge führen, da die Batterie einen beträchtlichen Anteil der Gesamtkosten eines Elektrofahrzeuges ausmacht.

In dieser Arbeit wird ein Optimierungsmodell entwickelt, welches intelligente Ladestrategien für Elektrofahrzeuge generiert. Das Modell berücksichtigt sowohl Strompreise als auch Batteriealterung und erzeugt damit Ladestrategien, welche den optimalen Kompromiss zwischen strompreisgeführtem Laden und langer Batterielebensdauer darstellen.

Zunächst wird ein Mobilitätsmodell zur Simulation des Energieverbrauchs von Elektrofahrzeugen sowie des Fahr- und Parkverhaltens der Nutzer erarbeitet. Die simulierten Reisewege der Elektrofahrzeuge und die zugehörigen Energieverbräuche dienen später als Eingangsdaten für das Optimierungsmodell der intelligenten Ladestrategien.

Experimentelle Daten von Batteriealterungstests, welche darauf ausgerichtet wurden den Betrieb von Lithium-Ionen-Batterien in Elektrofahrzeugen widerzuspiegeln, bilden die Grundlage für ein umfassendes Batteriealterungsmodell. Sowohl die zyklische als auch die kalendarische Alterung werden untersucht und der Einfluss von Batterieladezustand, Laderate sowie Betriebsbereich auf die Batteriealterung wird analysiert. Eine kalendarische Alterungsfunktion sowie eine dreidimensionale Funktion der zyklischen Alterung werden hergeleitet. Diese Funktionen modellieren später die Batteriealterung innerhalb der Ladeoptimierung.

Das Ladeoptimierungsmodell minimiert die Gesamtkosten der Ladevorgänge, welche sich aus Ladestromkosten und Batteriealterungskosten zusammensetzen. Das mathematische Optimierungsproblem wird zunächst als gemischt-ganzzahliges, nichtlineares Problem formuliert und anschließend mithilfe von stückweise linearer Approximation und anderen Linearisierungsmethoden in ein gemischt-ganzzahliges, lineares Problem transformiert.

Das Ladeoptimierungsmodell wird auf eine Auswahl von 300 Elektrofahrzeugen angewandt und verschiedene Szenarien werden berechnet und analysiert. Der Anteil der Batteriealterungskosten liegt bei 13 % bis 45 % der gesamten Ladekosten für die verschiedenen Szenarien. Dies unterstreicht die Wichtigkeit, die Batteriealterung in die Optimierung von Ladestrategien zu inkludieren. Der optimale Betriebsbereich liegt in den meisten Fällen zwischen einem Batterieladezustand von 10 % und 50 %. Die Ladezeiten fallen mit Zeiten niedriger Strompreise zusammen, welche üblicherweise mit einer niedrigeren Stromnachfrage korrelieren. Schnellladen wird fast niemals angewandt. Dies zeigt, dass die höheren Batteriealterungskosten, verursacht durch Schnellladung, nicht durch eine Reduktion der Stromkosten durch Laden von mehr Energie in günstigen Perioden aufgewogen werden können.

Acknowledgements

First of all, I want to thank my father for putting the idea of doing a PhD into my head years ago. If it were not for his motivation and influence, it would have been much harder to get through the not so easy times within the past few years.

I am very grateful to Prof. Dr. Thomas Hamacher for his guidance and continuous support. Despite the distance and time difference, he was always available and willing to listen and mostly had a solution for problems and thoughts I was having on my mind.

I very much appreciate the opportunity I was given to work and research in Singapore, facilitated by the National Research Foundation of Singapore by initiating and funding the research project TUM CREATE. I have learned so much and experienced many unforgettable moments during my time in Singapore that I would not want to have missed.

I would like to thank my colleagues at TUM CREATE in Singapore whom it was not only great to work with but also to make friends with so many of them. When I was in Munich, the colleagues at the Chair of Renewable and Sustainable Energy Systems and the Chair of Energy Economy and Application Technology granted me asylum at their offices and warmly included me into their groups. I always enjoyed the time there, thank you!

A big thank you to all colleagues, friends, and family who contributed to this work by discussions, suggestions, advice, or proofreading, especially Patrick Osswald, Philipp Kuhn, Paul Stursberg, Magdalena Dorfner, Carola Trippe, Frederik Trippe, David Ciechanowicz, and Pablo López Hidalgo. Special thanks go to Raffaela Riemann for the countless optimisation sessions at our desks, in the coffee corner at CREATE Tower, the Italian, the taxi on the way to Rawa, ... Those were so helpful and also fun!

I want to express my gratitude to my entire family who is always there for me and gives me the boundless feeling of being home even when I was not.

Patrick, last but not least, thank you so much for your endless help and support, for ensuring and reminding me of what I should know, for getting me back on my feet when I was stumbling in front of my big mountain. I could not have done it without you.

Contents

List of Figures

List of Tables

List of Abbreviations

AC alternating current

BEV battery electric vehicle

CDF cumulative distribution function

CC constant current

CP constant power

CV constant voltage

DC direct current

DOD depth of discharge

EUR Euro

GAMS General Algebraic Modeling System

GST goods and services tax

HFEDS Highway Fuel Economy Driving Schedule

HITS Household Interview Travel Survey

ICE internal combustion engine

LP linear programme

LTA Land Transport Authority

MIP mixed-integer programme

MILP mixed-integer linear programme

MINLP mixed-integer non-linear programme

PA planning area

PHEV plug-in hybrid electric vehicle

QCQP quadratically constrained quadratic programme

QP quadratic programme

SEI solid electrolyte interphase

SGD Singapore Dollar

SOC state of charge

SOC_{start} state of charge at the beginning of charging process

SOC_{end} state of charge at the end of charging process

ΔSOC difference in state of charge, that is charged to a battery

SOS2 special ordered sets of type 2

SQL structured query language

UDDS Urban Dynamometer Driving Schedule

USD US Dollar

USEP Uniform Singapore Energy Price

Nomenclature

η_{batt} Efficiency of battery [–]

η_{chaSt} Efficiency of charging station [–]

η_{drTr} Drive train efficiency [–]

η_{eng} Engine efficiency [–]

τ Velocity based time interval $\tau_1, \ldots, \tau_4$

a Index of agent $1, \ldots, n$

b_{cha} Binary, whether vehicle is charging or not during time step t [–]

b_{park} Binary, whether vehicle is parking or not during time step t [–]

C_{ageCal} Calendar ageing cost during one time step [$]

C_{ageCyc} Cycle ageing cost of one charging process [$]

C_{ageTot} Total battery ageing cost for all charging processes of simulation [$]

C_{batt} Battery cost for each agent's vehicle [$]

$C_{specBatt}$ Specific battery cost [$/kWh]

C_{elTot} Electricity cost for all charging processes of simulation [$]

C_{tot} Total cost for all charging processes of simulation [$]

d Trip distance [km]

d_{drCy} Distance driven during driving cycle [km]

DOD Depth of discharge: state of charge range, in which a battery is cycled [–]

E_{batt} Energy stored in the battery [kWh]

E_{cons} Energy consumption of a battery electric vehicle [kWh]

E_{grid} Energy drawn from the power grid [kWh]

E_{nom} Nominal energy content of a battery [kWh]

$E_{specCons}$ Specific energy consumption of a battery electric vehicle [kWh/100km]

$e_{fade,cal}$ Energy fade due to calendar ageing [h^{-1}]

$e_{fade,cyc}$ Energy fade due to cycle ageing [Wh^{-1}]

$e_{fade,cha}$ Energy fade only during charging process [–]

$e_{fade,tot}$ Total energy fade during cycling due to calendar and cycle ageing [Wh^{-1}]

f_{age} Ageing factor for different charge rates [–]

f_{dis} Ratio of discharge ageing to total ageing [–]

f_{EOL} Share of nominal energy content at which a battery reaches its end of life [–]

f_{resale} Resale factor for a battery at end of life [–]

$f_{traLoss}$ Transmission loss factor [–]

$g_1, \ldots, g_7$ Coefficients of function on energy fade during charging process at 1 P [–]

$g_8, \ldots, g_{12}$ Coefficients of ageing factor function [–]

h_1, h_2, h_3, h_4 Coefficients of tangent hyperplane equations of cycle ageing [–]

h_5, h_6 Coefficients of linear equations of calendar ageing [h^{-1}]

i Index of parking $1, \ldots, m$

j Index of trip $1, \ldots, m$

k Index of tangent hyperplane equations of cycle ageing $1, \ldots, 142$

l Index of linear equations of calendar ageing $1, \ldots, 2$

P Charge power for each parking event and time step [kW]

P_{fix} Charge power for a parking event [kW]

P_{min} Minimum charge power [kW]

P_{max} Maximum charge power [kW]

P_{maxSys} Power limit by power system [kW]

P_{aux} Power required by auxiliaries of a battery electric vehicle [kW]

P_{road} Power to overcome road load of a battery electric vehicle [kW]

P_{veh} Power to propel and operate a battery electric vehicle [kW]

pr_{el} Electricity price for each time step [$]

r_{cha} Charge rate [–]

$r_{cha,max}$ Maximum charge rate [–]

SOC_0 State of charge at the beginning of simulation time [–]

SOC_{start} State of charge at the beginning of parking [–]

SOC_{end} State of charge at the end of parking [–]

SOC_{min} Minimum state of charge of a battery [–]

SOC_{max} Maximum state of charge of a battery [–]

t Index of time step $1, \ldots, T$

Δt Duration of one time step [h]

v Vehicle type $1, \ldots, 151$

z Time steps of driving cycles $z_1, \ldots, z_Z$

Chapter 1

Introduction

1.1 Motivation

The increasing number of battery electric vehicles (BEVs) becoming part of the transportation sector fuels discussions on whether, how, and when they might supersede internal combustion engine (ICE) vehicles.

Typical drivers for the introduction and upswing of BEVs are the enduring discussion on depletion of fossil energy carriers or reduction of local emissions in large metropolitan areas with high traffic density. Also, the use of battery electric vehicles in a smart grid, for example by levelling out fluctuations in the electricity demand and supply, is debated intensely. Drawbacks might be the limited range of BEVs combined with high cost of purchase, which can lead to low customer acceptance. The expansion and further development of (intelligent) charging infrastructure is another topic to be addressed. Research is carried out to analyse and evaluate the aforementioned aspects of BEVs and to propose solutions for the beneficial operation of BEVs.

In order to obtain the energy required to serve their transportation purpose, battery electric vehicles are directly linked to the power system. With rising numbers of BEVs, the impact of the additional electricity demand on the power system becomes noticeable. Hence, controlling the charging process of BEVs makes sense, for example, in order to avoid unfavourable increasing or additional demand peaks.

The systematic control of the charging process can be advantageous for the battery electric vehicle itself, too. Depending on how and when it is charged, the battery is affected differently and shows variable degrees of performance loss, caused by continuous degradation of the different battery components, commonly denoted as ageing.

As the battery pack accounts for a considerable share in the total vehicle cost for a BEV, this is a crucial issue to be investigated. With specific cost for lithium-ion battery packs of currently around 400 USD/kWh (Nykvist & Nilsson, 2015; Pillot, 2015), a 27.2 kWh battery would cost 10 880 USD. Regarding a BMW i3 (purely electric version with the larger battery) at a price of 36 150 EUR with a battery pack of corresponding energy content, the battery makes up for around 28 % of the total vehicle price (BMW AG, 2016). Even with declining cost of 250 USD/kWh until 2020 (Pillot, 2015), it would still be 17 %.

Since the parking duration of BEVs usually exceeds the time needed to recharge the battery, the electricity demand of BEVs is a flexible load, meaning it can be shifted within a certain time frame and scaled to different power levels. This flexibility can be used to recharge the BEVs power system friendly or battery friendly.

Charging strategies favourable to the power system imply charging as much energy as possible during periods of low grid load, usually correlated to lower electricity prices. However, this may have negative effects on the battery ageing behaviour. Battery ageing depends on various factors such as state of charge of the battery, charge power, or temperature. Fast charging with high power is generally worse for a battery than charging with low power. Hence, controlling the charging process only with regards to the power system might harm the battery. Therefore, it is important to consider both the power system and the battery ageing when searching for intelligent charging strategies.

The aim of this work is to elaborate an optimisation model which allocates optimal charging strategies for battery electric vehicles. Given a travel schedule of the vehicles and corresponding energy consumption, an optimal trade-off between electricity price controlled charging and battery lifetime shall be found.

1.2 State of the Art in Intelligent Charging Strategies

The entering of battery electric vehicles into the automotive market directly linked the automotive sector to the power sector. Hence, the notion of controlled or intelligent charging of battery electric vehicles (BEVs) or plug-in hybrid electric vehicles (PHEVs) became a focus of research in both of these fields. Controlled charging starts from a charging process which requires a little more planning than simply plugging in as soon as a vehicle arrives somewhere, and can reach up to intelligent charging strategies including steering the exact time and duration of the charging process, the charge power, location, possible rest periods, interim discharge intervals, and more.

Focus on Power System

Focusing on the power system and its constraints, comprehensive research has been and still is conducted on the influence of the intelligent use of electric vehicles.

Sortomme and El-Sharkawi (2011) propose an optimised charging algorithm for BEVs, which combines advantages for several parties: it minimises charging cost for the BEV owners, maximises profits for an aggregator bidding the combined capacity of several electric vehicles into the energy markets, and improves power system operation.

Similarly, in Gonzalez Vaya and Andersson (2015), a BEV aggregator bids into the day-ahead electricity market in order to minimise charging cost and meet the BEVs' energy demand. However in this model, the aggregator is assumed to affect market prices and the BEVs' requirements are probabilistic as driving patterns cannot be perfectly predicted.

In Sundstrom and Binding (2012), a central approach is used to control the charging of battery electric vehicles in a way that neither power nor voltage limits of the power distribution grid are reached while the vehicle owners' requirements have to be met.

In contrast, Ma et al. (2013) suggest a decentralised solution. In order to cover a very large number of electric vehicles, each BEV chooses and implements its own local charging strategy with the aim of minimising its individual charging cost. The charging strategies follow a common electricity price signal and aim for valley-filling of the power demand curve at night-time.

Also, feeding electricity from electric vehicles back to the power grid – known as vehicle-to-grid – and thereby providing ancillary services to the power systems is the topic of numerous works. Kempton and Tomić (2005a, 2005b) introduced the notion of vehicle-to-grid. The power market and different electric vehicle types were assessed in order to elaborate strategies for vehicle-to-grid implementation. Thereby, the decrease in battery lifetime played only a minor role and was considered in a very simplified way. Also Sortomme and El-Sharkawi (2012) added vehicle-to-grid to their previous model, but took battery degradation due to additional discharge/charge cycles for vehicle-to-grid into account only very rudimentarily.

All those research studies have in common that the proposed intelligent charging strategies orientate towards a favourable effect on the power system.

To evaluate the interplay between transportation sector and power system, Waraich et al. (2013) integrated an agent-based traffic demand model for the electricity demand of electric vehicles and a power system simulation. This framework offers an approach to analyse the impact of electricity demand of BEVs on transportation and electricity networks.

Focus on Battery Degradation

From the automotive sector's perspective and of course from the consumers' perspective, the battery of an electric vehicle plays a crucial role, as it contributes substantially to the total cost of a battery electric vehicle (Bernhart, 2014; Pillot, 2015). Therefore, it makes sense to investigate how specific modes of operation, including various parameters like charge and discharge current, number and depths of cycles, as well as temperature, influence the battery's lifetime. The wide field of battery research contains an uncountable number of publications on battery ageing. At this point, it shall be focused only on literature regarding battery ageing models applied to the usage of batteries in an electric vehicle.

A battery degradation model for plug-in hybrid electric vehicles (PHEVs) with lead acid batteries in hybrid electric vehicles was used by Amiri et al. (2009) to optimise power train efficiency by minimising losses in battery lifetime amongst other losses of the system.

Nowadays, lithium-ion batteries are the technology of choice used in battery electric vehicles and are the focus of the further research discussed.

The optimisation of charging patterns for PHEVs also includes energy cost beside battery degradation in the work of Bashash, Moura, Forman, and Fathy (2011) and Bashash, Moura, and Fathy (2011). A multi-objective optimiser is used to minimise both energy cost and battery degradation by altering the energy amount charged and the time when to charge. Within the battery model, degradation is reflected by growth of a resistive film at the anode, leading to an increasing internal resistance and capacity loss.

However, battery ageing exhibits multiple complex aspects. Especially the non-linearity in dependence of state of charge (SOC) and depth of discharge (DOD) is not addressed. Furthermore, the chosen cell with lithium iron phosphate cathode and graphite anode is not suitable for an application in electric vehicles due to its low energy density (Scrosati & Garche, 2010). As a consequence, the electrochemical model presented does not fit very well to the ageing data in the manufacturer's data sheet, which is used for validation. The energy consumption of PHEVs and the related fuel and electricity cost is minimised by means of an optimal power management model for the PHEV, which allocates fuel from the tank or electricity from the battery as energy source to propel the vehicle. Electricity prices or other power system constraints do not play a role in the optimisation. For a sample of trips, a pareto front of several solutions (combinations of energy cost and battery degradation corresponding to a specific charging pattern, where a decrease in energy cost would increase the battery degradation) was identified. Then, the multi-objective optimiser chooses one solution out of each pareto front, using a weighting coefficient between energy cost and battery degradation.

Guenther et al. (2013) study the impact of different load profiles on battery ageing in electric vehicles. A battery ageing model, based on available literature and comprising calendar and cycle ageing, indicates the decrease in energy storage capability of the traction battery. The ageing effects are calculated as a function of depth of discharge (DOD) for cycle ageing, as well as temperature and state of energy for calendar ageing. The state of energy is calculated equivalent to the state of charge, based on nominal energy content instead of nominal capacity of a battery. Different charge/discharge profiles to be imposed on the BEV are composed of a driving cycle, which affects the energy consumption of a BEV, the start time of charging, charge power and an optional vehicle-to-grid service for peak shaving of the power grid load. For each load profile, the resulting battery ageing effect is calculated and compared. Thereby, the influence of load profiles on battery ageing can be analysed. However, as both the battery ageing model and the charge/discharge profiles are rather simplified (with only two different charging start times and charge power levels), the deduced conclusions only give a very basic insight into the interrelation between battery ageing and charge/discharge profiles.

Focus on Power System and Battery Degradation

As an additional aspect, the effects on the power system are included in some research. An analysis of vehicle-to-grid strategies considering the state of health of battery electric vehicles is proposed by Marongiu et al. (2014). Two types of lithium-ion batteries with different battery cell chemistries are simulated, applied to a sample of 100 BEVs with different states of health. An ageing prediction model is parametrised for each cell chemistry through battery ageing tests. The calendar ageing model takes state of charge (SOC), time, and temperature into account, while the cycle ageing model considers the depth of discharge (DOD) when cycling a battery. The state of health is calculated by adding the contribution of calendar and cycle ageing to the initial state of health of a new cell. Different vehicle-to-grid strategies are evaluated. The power system requests grid regulation to be fulfilled by vehicle-to-grid from the BEVs. The resulting load profiles correspond to a certain deterioration in battery state of health, caused by additional

cycling for provision of this grid regulation services. Thereby, the influence of different vehicle-to-grid strategies on the batteries' state of health could be investigated.

Rather than merely investigating the effects of different charging/discharging patterns on the battery lifetime, some try to find optimised charging/discharging strategies taking into account battery ageing and power system effects to some extent.

A combination of battery ageing cost and power system effects included in a charging optimisation can be found in the work of Lunz, Walz, and Sauer (2011). A genetic optimisation algorithm is used to minimise battery ageing cost of PHEVs while maximising profits from a vehicle-to-grid application. SOC of the batteries as well as cycle depth play a role in calculating battery ageing cost. The calendar ageing depends on the SOC as an exponential function, cycle ageing is a power function with input cycle depth. Effects of the charge power on ageing behaviour are not regarded. In two scenarios, a constant and a two tariff energy price serves as input for the determination of energy trading cost or profits and energy cost for driving. The charge and discharge behaviour is optimised for the duration of one day.

A similar battery ageing behaviour is presented by Lunz, Yan, Gerschler, and Sauer (2012), but underlayed with experimental data. Ageing tests were conducted on lithium-ion battery cells and used to analyse calendar and cycle ageing. Calendar ageing was observed for different temperatures and at different SOCs. Both parameters worsen the calendar ageing when increasing their values. Additionally, some cells were cycled at different average SOCs with a cycle depth of 10 % ΔSOC. Cycling around a higher average SOC increases battery ageing, again. Those results are utilised to define a battery lifetime saving charging strategy – i. e. to charge as late as possible before departure. Another charging strategy is cost optimised: charging whenever electricity prices are lowest. Different scenarios are calculated using either the battery lifetime saving strategy, the cost minimising strategy, or a charging strategy including vehicle-to-grid. Rather than conducting an optimisation on charging strategies, the influence of different charging strategies on the charging electricity cost and the battery ageing cost is exemplified.

An optimisation which minimises the cost for charging (plug-in hybrid) electric vehicles consisting of electricity cost and battery degradation cost is proposed by Hoke et al. (2014). A simplified lithium-ion battery model reflects capacity and power fade of a lithium-ion battery during its lifetime. The effects on battery degradation modelled are average SOC, DOD as well as temperature, while charge power does not play a role in determining battery degradation in this model. A dependence among the three modelled effects is assumed to be non-existent. The simplified model is validated by comparing and fitting it to single data points of a more complex battery degradation model based on experimental data (cf. Hoke et al. (2011)). Given a constant or variable electricity price profile, plug-in times, and initial SOCs, the optimisation method is applied to three different vehicles. The resulting charge power profiles for the (plug-in hybrid) electric vehicles propose charging when electricity prices are low, slow charging for lower temperatures, and charging as late as possible for a lower average SOC.

Moving away from traction batteries in electric vehicles, related research questions on optimised charging arise for the application of stationary energy storage as part of the power system. In Koller et al. (2013) and Fortenbacher et al. (2014), battery degradation

cost functions are developed and used to find an optimal control of batteries for peak shaving of the power grid load. Goebel et al. (2016) optimise dispatch strategies for stationary batteries to provide ancillary services to the power system, using an electro-thermal lithium-ion battery model including battery ageing models. However, those approaches differ as other circumstances apply than for electric vehicle charging, where the option to (dis)charge depends on parking time and is not always available.

1.3 Outline

The aim of this work is to develop an optimisation model for intelligent charging strategies for battery electric vehicles (BEVs), which considers fluctuating electricity prices on the one hand and battery ageing behaviour on the other.

The objective of the optimisation problem is to minimise total charging costs, consisting of electricity cost required for recharging the BEVs as well as battery ageing cost caused by the charging process.

In Chapter 2, an agent-based model is designed to represent the mobility behaviour of BEVs. The model simulates the daily travel schedules of BEVs using the example of the city state of Singapore and provides input data for the computation of the charging optimisation model. It is based on a Singaporean travel behaviour survey and other statistical data as well as on a battery electric vehicle model. The scope of this work are private vehicles, which are simulated as battery electric vehicles. Fleet and commercial traffic is not regarded. Since the relatively low ratio of driving to parking time of private vehicles allows for a high degree of shifting charging processes in time and space, private BEVs offer substantial possibilities for optimisation concerning their charging processes. Therefore, private vehicles were chosen as a base for the charging optimisation model.

Chapter 3 describes the modelling of battery ageing. Firstly, a short introduction on the fundamentals of lithium-ion cells is given. Next, the conduction of battery ageing tests to examine cycle and calendar ageing effects is explained and the results are analysed. Ageing tests retracing driving cycles are conducted to validate the application of the battery ageing model to BEVs. Different battery ageing parameters are derived, building up a battery ageing model to be integrated into the optimisation model. The battery ageing model consists of a calendar ageing function as well as a multidimensional cycle ageing function.

In Chapter 4, the charging optimisation model is elaborated, integrating the models from Chapters 2 and 3. The charging optimisation model minimises total charging costs, consisting of charging electricity cost and battery ageing cost. The travelling schedules and corresponding energy consumption of the BEVs to be optimised are given. The charging processes are flexible and can be optimally allocated in order to make use of periods with low electricity prices and keep the battery ageing at a minimum at the same time.

A brief overview of the relevant optimisation theory is given. The battery ageing model from the preceding chapter is further transformed in order to be integrated into the charging optimisation model. The battery ageing functions serve as input to define the battery ageing cost. The initial optimisation problem is formulated as a mixed-integer

non-linear programme. The approach of piecewise linear approximation is used to adapt the non-linear cycle ageing function to suit the requirements of a convex optimisation problem. Beside piecewise linear approximation, other linearisation techniques are used. As a result, the charging optimisation problem can be reformulated as a mixed-integer linear programme, which can be solved more efficiently than a mixed-integer non-linear programme. The charging optimisation model optimises when exactly a BEV is charged, when it obtains a rest period during which it is neither charged nor discharged, in what range of state of charge it is operated, and at what charge power.

An application of the charging optimisation problem is presented in Chapter 5 for the city state of Singapore. The mobility model described in Chapter 2 delivers the input data on the mobility behaviour necessary for the charging optimisation. For a sample of 300 BEVs and a duration of four weeks, optimal charging strategies are determined and analysed. A scenario analysis is conducted to identify the influence of different input parameters on the charging patterns. General recommendations on favourable charging strategies are derived.

The work is concluded in Chapter 6 and an outlook on future research in this field is given.

Chapter 2

Mobility Behaviour in Singapore

In order to apply the charging optimisation model which will be developed in this work and to evaluate the resulting optimal charging strategies, first of all, one needs to understand and simulate the mobility behaviour of battery electric vehicles. Using the example of Singapore, a mobility model is developed picturing the driving and parking patterns of car drivers. Corresponding to the scope of this work, only private vehicles are analysed and taken into account, leaving out fleet and commercial traffic.

The elaborated mobility model is capable of simulating the mobility behaviour of a sample of vehicles over a certain time horizon. It was programmed in MATLAB 2014a (The MathWorks, Inc., 2014) and within each simulation, it creates a number of battery electric vehicles (BEVs), owned by so-called agents. For each agent and its electric vehicle, a sequence of trips and parking in between the trips is generated. Corresponding to each trip, information on departure and arrival time, origin and destination, trip distance and duration, energy consumption during the trip, as well as purpose of the trip is simulated. Accordingly, all parking events are assigned values for arrival and departure time, parking location, parking duration and purpose. All this information on travel behaviour serves as input to the charging optimisation model.

Contents of the following chapter were published in *Mobility Model for the Estimation of the Spatiotemporal Energy Demand of Battery Electric Vehicles in Singapore* (Trippe et al., 2015) and are described in an adapted form within this chapter.

2.1 Mobility Profiles

As a first step, mobility profiles are generated in order to picture the movement of vehicles throughout the day spread over the entire city. The mobility profiles used in the mobility model are based on data from the Household Interview Travel Survey (HITS) of 2012. It is a survey on travel behaviour of people in Singapore and is typically conducted every four years by the Singaporean Land Transport Authority (LTA). The detailed HITS data were made available for this analysis by LTA. The entire data set was organised into a database and by means of structured query language (SQL) queries and MATLAB scripts, information on different aspects were retrieved, for example employment, working hours, number of car drivers, and especially trips conducted by car. The HITS data proved to

be a proper representation of the Singaporean population after comparison with other Singaporean statistics from the year 2012. The employment rate among interviewed persons in HITS, 95.1 %, deviated by only 2.3 % from the employment rate in Singapore, 97.4 % (Ministry Of Manpower, 2013, p. A3). Regarding the working hours, the HITS data showed a duration of stay at work of 8.82 h per day on average, equalling 44.1 h per week. This value lay 3.3 % below the official value of 45.6 h from the Ministry Of Manpower (2013, p. C14). While 617 570 cars (Land Transport Authority, 2015b) per 1 152 000 households (Department of Statistics Singapore, 2013, p. 46) in Singapore in 2012 resulted in a ratio of 0.54, the HITS data offered a ratio of 0.43 cars per household. Hence, households with cars are slightly underrepresented within the HITS data compared to the entire city of Singapore. However, this is not a problem since only trips made by car within the HITS data are analysed. The data samples used for the mobility profiles are less extensive, but the statistical distribution thereof is expected to be the same.

After validating the HITS data with general statistical data of Singapore, mobility profiles are generated for their application within the mobility model. The relevant information on trips conducted by car is extracted from the HITS data: origin, destination, purpose, departure and arrival time. The mobility profiles serve as a basis for the simulation of travelling schedules of agents driving electric vehicles in Singapore. It is assumed that people in Singapore drive battery electric vehicles according to the same mobility patterns as conventional internal combustion engine vehicles, as it is mainly the case for persons interviewed in HITS. This is a fair assumption because due to the small geographical size of Singapore – 49 km from east to west and 25 km from north to south (Department of Statistics Singapore, 2015, p. 15) – no restrictions originating from the limited range of BEVs should arise for the drivers in their daily mobility patterns.

The routine of generating the mobility profiles for each agent and each day is pictured in Figure 2.1. Following this routine, the mobility model is simulating the mobility behaviour of car drivers in Singapore.

When running a simulation with the mobility model, agents and their travelling schedules are generated. The latter consist of a sequence of alternating trips and parking. Each of these activities as well as each agent is assigned attributes such as home address, origin, destination, departure and arrival time, duration, as well as energy consumption. The specific values are randomly picked from different probability distribution functions, which were elaborated beforehand.

At first, each agent is assigned a home address as well as a departure time in the morning. In Singapore, each address or building is distinctly defined by a postal code. Each postal code belongs to one of Singapore's 54 planning areas, a partitioning of Singapore introduced by the Urban Redevelopment Authority (2015). Instead of allocating an exact postal code as home address, the corresponding planning area is sufficiently accurate for the utilisation within the mobility model. In order to relate home addresses to the agents, the spatial distribution of car drivers' home addresses in Singapore was evaluated from the HITS data and divided into the existing 54 planning areas. According to this distribution, the homes of the agents are dispersed among the different planning areas in Singapore during a simulation and each agent obtains one planning area corresponding to his home address. Analogously, the departure times

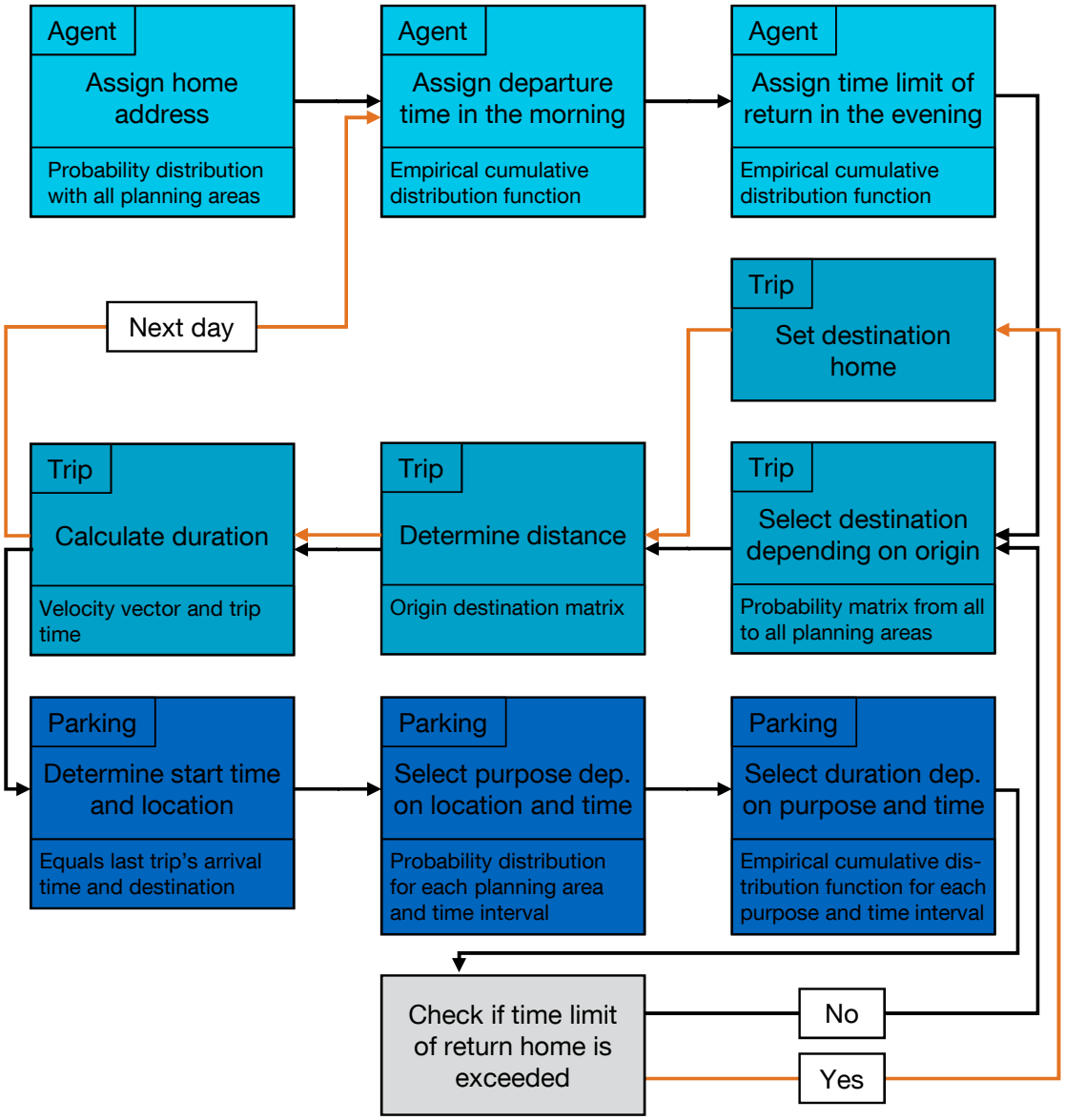

Figure 2.1 – Flow diagram of the generation of mobility profiles during a simulation with the mobility model

in the morning of persons driving a car were analysed from the HITS data and two empirical cumulative distribution functions (CDFs) were derived; one for weekdays, one for the weekend. Each agent is assigned a departure time in the morning, randomly picked from the respective empirical CDF.

After the assignment of home address and departure time in the morning, the daily travelling schedule of each agent follows, beginning with a trip. The destination of each trip is selected depending on its origin. Subsequent to each trip, a vehicle is parking and the destination of the previous becomes the origin of the next trip. The origin of the first trip in the morning is the agent's home address. In order to obtain the destinations of the

trips, all car trips within the HITS data were evaluated in terms of origin and destination and two probability matrices were deduced; one for weekdays and one for the weekend. Each row represents one origin planning area and each column one destination planning area, while the matrix elements denote the probabilities at which an agent travels from one planning area into another, summing to 100 % along each row (see Table 2.1). The

		Destination				
		PA 1	PA 2	...	PA 54	Sum
Origin	PA 1	... %	... %	... %	... %	100 %
	PA 2	... %	... %	... %	... %	100 %
	...	... %	... %	... %	... %	100 %
	PA 54	... %	... %	... %	... %	100 %

Table 2.1 – Probability matrix to travel from one planning area (PA) to another; one matrix for weekdays, one for the weekend

destination of each trip is selected according to the probability distribution corresponding to the current origin planning area, which can be read out of the respective probability matrix. In order to determine the distance travelled, an origin destination matrix was developed. The HITS data provided information on trip origin and destination in postal code format, so the web mapping service Google Maps (Google, 2015) was utilised to obtain the distance of each car trip by means of a script running automated queries. All trip distances were classified into planning areas and for each combination of origin and destination, the average distance between the respective planning areas was calculated and entered into the origin destination matrix (see Table 2.2). By knowing origin and

		Destination			
		PA 1	PA 2	...	PA 54
Origin	PA 1	... km	... km	... km	... km
	PA 2	... km	... km	... km	... km
	...	... km	... km	... km	... km
	PA 54	... km	... km	... km	... km

Table 2.2 – Origin destination matrix with average distance from one planning area (PA) to another

destination of a trip, the distance can be simply read out from the origin destination matrix. The trip duration is calculated by means of the trip distance and velocity. For the calculation, the time of day of a trip is considered and thereby, different traffic situations and densities throughout the day are reflected in the mobility model. For this purpose, a vector containing average velocities in Singapore for each 15 min over a period of 24 h – as introduced by Moecker (2014) – is used.

Each trip is followed by a parking activity, which has to be defined next. The start time and location of a parking activity equals the arrival time and destination of the preceding trip. Each parking activity holds a specific purpose and parking duration. Depending on the current location and time, different purposes are more or less likely – for example, in the central business district in the morning, the purpose of parking is

more likely to be work-related than being at home. Hence, one day was divided into five time intervals: 6:00–9:30, 9:30–13:30, 13:30–17:30, 17:30–21:00, and 21:00–6:00. The first time interval in the morning was chosen corresponding to the traffic peak period in Singapore (Land Transport Authority, 2016), when everyone drives to work. The next two time intervals split the working hours into two equally long intervals. The fourth interval coincides with the evening rush hour, followed by a time interval covering the night hours when most people are at home. The various purposes given by the HITS data were classified into three categories: *home*, *work*, and *other*. *Home* contains all activities carried out at an agent's home. All work- and education-related trips and parking are included in *work*. *Other* comprises all remaining purposes, such as leisure activities, shopping, dining, or other personal business and errands. For each time interval and planning area, a probability distribution of the three purpose categories was elaborated from the HITS data. The purpose of parking is randomly selected from the suitable probability distribution, as illustrated in Figure 2.2. The duration of stay depends on the time of

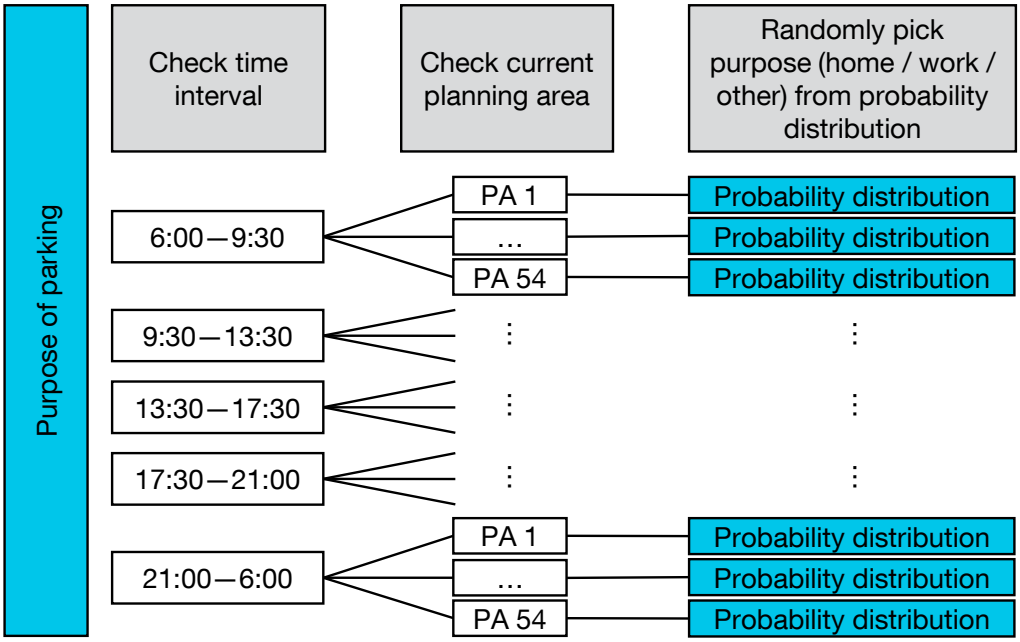

Figure 2.2 – Selection of parking purpose from different probability distributions

day as well as the purpose. Hence, the parking durations derived from the HITS data were split by the five time intervals and the three purpose categories. When classifying the data set of car trips available from the HITS data and therewith interconnected parking activities like this, each class was not sufficiently large to fit known probability distributions to the samples of parking durations. Thus, empirical CDFs were elaborated for each purpose category and time interval, with bin widths of 0.5 h. For each parking activity, the duration is drawn from the empirical CDF corresponding to the current time and purpose, as shown in Figure 2.3. During the weekends, there is no partitioning into time intervals, because daily travel patterns are not as clearly structured as during a weekday. Therefore, for an entire day, only one duration distribution per purpose category and one purpose distribution per planning area were evaluated.

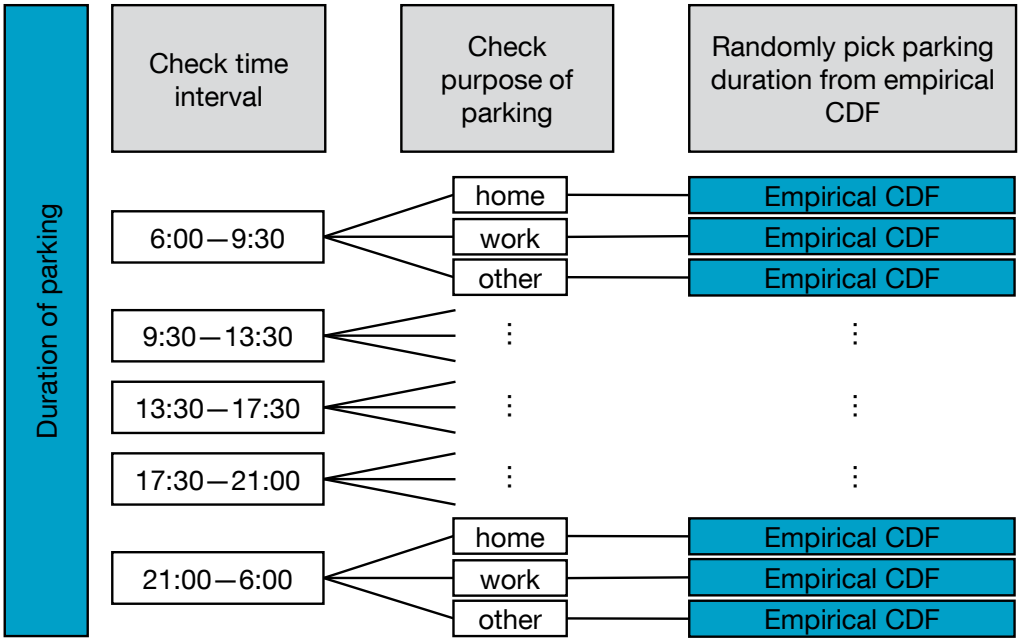

Figure 2.3 – Selection of parking duration from different empirical cumulative distribution functions (CDFs)

In order to validate the parking activities, the parking durations were compared to different sources. As mentioned before, the working hours from HITS accorded well with the ones from the Ministry of Manpower. Thus, it is assumed that the parking durations at *work* of persons within HITS driving a car also coincide with the general working hours in Singapore. Thereby, the parking durations at *work* are considered validated. In order to validate the parking durations at *other* locations, they are compared to two different data sources regarding shopping malls in Singapore: a field test at a shopping mall named ION Orchard as well as data from an online-service (Quantum Inventions, 2012) providing information on vacant parking spots in car parks of shopping malls.

The field test at ION Orchard was performed on Thursday, 8 December 2011, during which the parking durations of vehicles parking at the car park of this shopping mall were monitored. The field test data initially served as input for a previous version of the mobility model herein described, as presented by Huber, Trippe, Kuhn, and Hamacher (2012). Parking durations of trips made by car with destination *shopping centre* – a subcategory of *other* – were retrieved from the HITS data and compared to the parking durations of the field test. Figure 2.4 displays the empirical CDFs of these two data sets. The two data sets show a similar median of 2.25 h for the data set from HITS and 2.21 h for the field test data. This can also be seen in Figure 2.4, where approximately 50 % of the data overlap very well. However, the HITS data at *shopping centre* comprise a larger number of longer parking durations, mirrored by the mean value of 3.89 h in contrast to 2.39 h for the field test data. The discrepancy can be explained by the relatively small sample size of the HITS data at *shopping centre* in comparison to the field test.

Additionally, the number of cars parking at locations with purpose *other* in the course of a weekday was derived from the HITS data. It was compared to the average occupancy

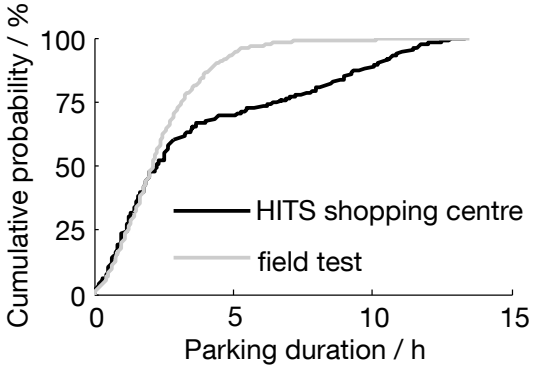

Figure 2.4 – Empirical cumulative distribution functions of parking durations from HITS data at *shopping centre* and field test at ION Orchard

of 23 car parks attached to shopping malls in Singapore on a weekday. The occupancy was elaborated from live data logged from Quantum Inventions (2012) between December 2011 and April 2012. Figure 2.5 shows this comparison and a similarity between the two curves is observed.

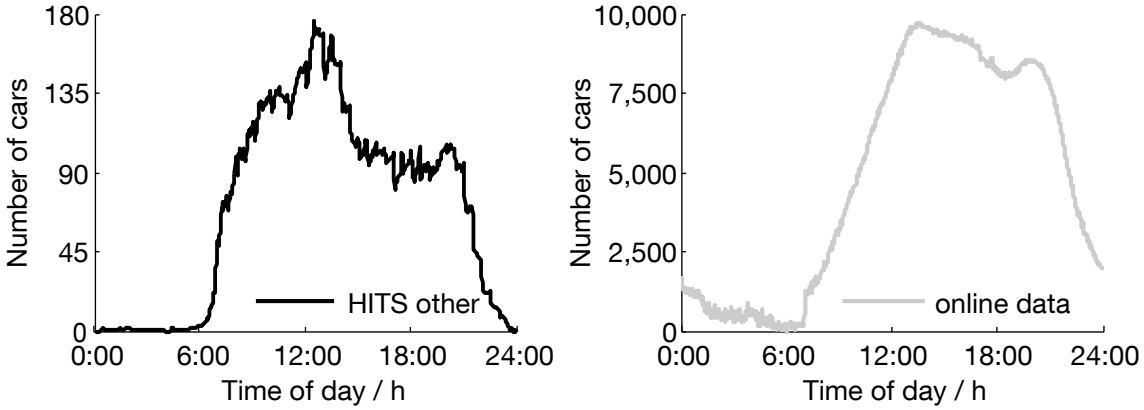

Figure 2.5 – Occupancy at *other* parking locations from HITS and at shopping mall car parks from online data

Even though the purpose category *other* contains more activities than shopping, the aforementioned two comparisons shall serve as validation for the parking durations at *other* locations. During the remaining time, when the agents are not driving or parking at *work* or *other* locations, they return *home*.

In order to determine the time to return home in the evening for each agent, the HITS data were examined in terms of last car trips of the day. Two empirical distribution functions for weekdays and weekend were elaborated thereof. According to this, each agent is randomly assigned a time limit for his return during a simulation. After each parking activity, it is checked whether the time limit is already exceeded and if so, the agent returns home with his next trip.

2.2 Vehicle Population

Besides the generation of mobility profiles, the vehicle population of battery electric vehicles (BEVs) is simulated. These days, the vehicle population of Singapore mainly consists of conventional internal combustion engine (ICE) vehicles and only a few BEVs (Land Transport Authority, 2015a). Therefore, a mere extrapolation of the current population is not sufficient to forecast the future number and vehicle type distribution of BEVs. Hence, the current distribution of ICE vehicles as well as the presently commercially available BEVs were used to elaborate the future BEV population of Singapore.

In order to determine the numbers and distribution of the various vehicle types in Singapore, statistics on the total car population (Land Transport Authority, 2015b), the car population by manufacturer (Land Transport Authority, 2014b), and by cubic capacity rating (Land Transport Authority, 2014a) were analysed. The various vehicle types were clustered into classes according to their kerb weight and engine power, while the power was weighted with the particular engine efficiency – $\eta_{eng} = 0.89$ for electric, $\eta_{eng} = 0.43$ for diesel, and $\eta_{eng} = 0.36$ for petrol engines (Braess & Seiffert, 2011, pp. 113, 162) – so that classes became comparable. Further commercially available BEVs were assigned to the different classes in order to generate a BEV population equivalent to the initial ICE vehicle population. Thereby, each class was complemented with the BEV specific parameters. The vehicle parameters of the internal combustion engine as well as battery electric vehicles were obtained from data sheets and official websites of the various automotive manufacturers. Since the battery of a BEV contributes a considerable part to the total weight, the mass of the ICE vehicles needed to be recalculated in order to reflect the additional weight of a battery within the equivalent BEV population. Within each class, the median energy content of all BEV batteries and an energy density of 120 Wh/kg (Braess & Seiffert, 2011, p. 117) on system level was used for the calculation of the additional weight of the ICE vehicles. In cases in which not all vehicle parameters could be obtained, the median value of the parameter within the affected class was used.

Each ICE vehicle type was adapted and complemented to an equivalent BEV type. In every class, various vehicle types occurred differently often, according to the initial distribution of the car population in Singapore. Thus, a BEV population equivalent to the present car population was obtained. During a simulation with the mobility model, a vehicle type from the distribution of the equivalent BEV population is picked for each agent.

2.3 Energy Consumption

When trip details and vehicle parameters are known, the energy consumption can be calculated. The energy consumption $E_{cons}(a, j)$ during agent a's trip j equals the sum of the partial energy consumption over the time intervals during which the trip is taking place (see equation (2.1)). The specific energy consumption value $E_{specCons}(v, \tau)$ of vehicle type v for each time interval τ is multiplied by the distance d covered during this interval. Each agent a owns one of the 151 vehicle types v. The share of the total distance of trip j by agent a during time interval τ is covered by $d(a, j, \tau)$. The four time intervals

τ_1 to τ_4 were selected based on the average velocity distribution in Singapore provided by Moecker (2014): 7:00–9:30, 9:30–17:30, 17:30–21:00, and 21:00–7:00[1]. Usually, a trip falls into only one or two time intervals due to the relatively long duration of the time intervals compared to the duration of a trip.

$$E_{cons}(a,j) = \sum_{\tau=\tau_1}^{\tau_4} E_{specCons}(v,\tau) \cdot d(a,j,\tau) \tag{2.1}$$

$E_{specCons}(v,\tau)$ holds a different value for each vehicle type v and time interval τ. Each time interval is represented by one driving cycle, which was selected and adapted in such a way that the driving conditions of the respective time interval are met; i. e. the average velocity of the driving cycle equals the average velocity in Singapore during the corresponding time interval. For the creation of the different driving cycles, the principle of the test procedure introduced in SAE International (2012) was used, which consists of a sequence of several instances of the Urban Dynamometer Driving Schedule (UDDS) and the Highway Fuel Economy Driving Schedule (HFEDS) (EPA United States Environmental Protection Agency, 2015). The concatenation and composition of the two driving schedules were altered in order to reflect, for example, traffic congestions during rush hours or a higher speed during the night hours. Thus, each of the four concatenated driving cycles mirrors the ratio between dense, urban traffic and highway driving patterns typical for Singapore within the respective time interval. A vehicle power profile $P_{veh}(v,\tau,z)$ appertaining to the driving cycle of time interval τ for each vehicle type v over all time steps z of the driving cycle was computed. The various values of $E_{specCons}$ were calculated by means of integration of the vehicle power P_{veh} of a specific vehicle over the duration of the respective driving cycle, divided by the distance driven during the driving cycle $d_{drCy}(\tau)$ (see equation (2.2)).

$$E_{specCons}(v,\tau) = \frac{1}{2} \sum_{i=1}^{Z-1} \left(P_{veh}(v,\tau,z_{i+1}) + P_{veh}(v,\tau,z_i)\right) \cdot (z_{i+1} - z_i) \cdot \frac{1}{d_{drCy}(\tau)} \tag{2.2}$$

P_{veh} is composed of the power required by the auxiliaries P_{aux} and the power to overcome the road load P_{road}. The latter is either divided by or multiplied with the efficiency of the drive train η_{drTr}, depending on whether the drive train transfers power to the wheels or vice versa. A positive value of P_{road} implies that power is delivered from the drive train to the wheels.

$$P_{veh}(v,\tau,z) = \begin{cases} \dfrac{1}{\eta_{drTr}} \cdot P_{road}(v,\tau,z) + P_{aux}, & \text{for } P_{road}(v,\tau,z) \geq 0 \\ \eta_{drTr} \cdot P_{road}(v,\tau,z) + P_{aux}, & \text{for } P_{road}(v,\tau,z) < 0 \end{cases} \tag{2.3}$$

P_{road} was computed by means of the road load equation based on the driving resistance as in (Braess & Seiffert, 2011, pp. 34–35), consisting of drag, rolling resistance,

[1]The velocity based time intervals for the energy consumption differ slightly from the previously mentioned time intervals for the selection of parking duration and purpose. This is due to the fact that the energy consumption is affected by velocity and therewith traffic, while parking duration and purpose depend on people's daily routine.

climbing resistance, and acceleration resistance. $P_{road}(v, \tau, z)$ and therewith $P_{veh}(v, \tau, z)$ as well as $E_{specCons}(v, \tau)$ were calculated beforehand for each BEV type v and each time interval τ. Hence, during a simulation with the mobility model, only $E_{cons}(a, j)$ has to be calculated for each trip j of a BEV.

2.4 Input Data for the Charging Optimisation Model

Resulting from a simulation with the mobility model, one obtains a sequence of trips and parking events with their specific attributes – i. e. start and stop time, energy consumption during a trip, location, and purpose – for a sample of BEVs. In view of the charging optimisation model, three of these attributes are of importance: the start and stop times of each trip and parking as well as the energy consumption during each trip. Therewith, the changes in the state of charge (SOC) of each BEV's battery due to a trip can be calculated and the possible times for recharging the batteries are defined.

Figure 2.6 displays a schematic diagram of a trip-parking-sequence obtained from the mobility model, which serves as input data for the charging optimisation. Starting in the

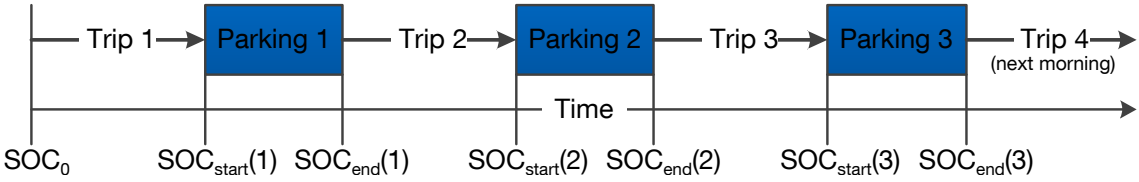

Figure 2.6 – Schematic diagram of a trip-parking-sequence generated by the mobility model

morning with a certain SOC_0, the subsequent $SOC_{start}(i)$ and $SOC_{end}(i)$ at the beginning and end of each parking i are calculated based on the preceding SOC values and depend on how much energy is consumed during a trip or recharged while parking. While the energy consumption of each trip as well as the times of each trip and parking is given by the mobility model simulation, the energy amount recharged during each parking will be determined by the charging optimisation model.

Besides the information regarding the trip and parking sequence, the mobility model delivers the nominal energy content of the BEVs' batteries as input data for the charging optimisation.

Chapter 3

Modelling of Battery Ageing

The charging optimisation model takes into account the electricity price as well as battery ageing cost. Hence, a model is developed to depict the battery ageing behaviour and to derive the battery ageing cost therefrom.

A short overview on the fundamentals of lithium-ion cells is given to understand the underlying ageing mechanisms. Battery ageing tests were conducted and analysed and form the basis of the battery ageing model. Ageing effects in a lithium-ion battery occur both during cycling and storage of the battery, called cycle ageing and calendar ageing. Different ageing parameters are derived from the battery ageing tests and are used to model the battery ageing behaviour. This battery ageing model is further used to calculate battery ageing cost within the charging optimisation model, which will be elaborated within the subsequent chapter.

3.1 Fundamentals of Lithium-Ion Cells

Lithium-ion cells are differentiated in primary and secondary cells. While primary cells often allow for higher energy density, secondary cells have a crucial advantage: their ability to be recharged. Two electrodes, electronically separated by a thin polymer layer, are connected ionically by an electrolyte as illustrated in Figure 3.1. An electrode consists of an active material, coated on a thin, current collecting metal foil. The active material has the ability to intercalate lithium-ions, meaning the reversible insertion of lithium-ions. In an ideal scenario, the active material acts as a host structure without interfering with the intercalated lithium-ion, and its physical and electrochemical properties remain unchanged during this process.

While discharging the cell, lithium-ions are de-intercalated from the anode (negative electrode). While the positively charged lithium-ions move through the electrolyte, the corresponding electrons are forced via an external circuit and an attached load. At the cathode (positive electrode), lithium-ions are intercalated and recombine with the electrons. In electrochemistry, the procedure is described as a redox reaction, where a reduction occurs at the cathode and the respective oxidation occurs at the anode. During the charging process, where an external charger is connected and energy is added to the system, the process is reversed.

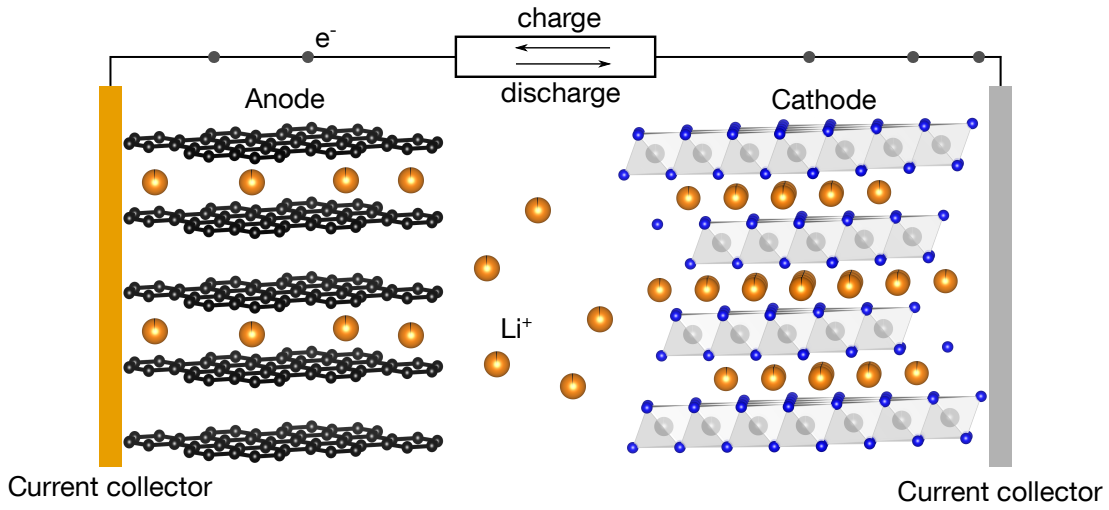

Figure 3.1 – Working principle of a lithium-ion cell

3.1.1 Components in Lithium-Ion Cells

Lithium-ion cells consist of various components which are optimised for the particular purpose of application, for example high energy density, high power capability, or long lifetime. The most important ones will be briefly discussed in the following.

Anode Materials

Lithium metal is the most suitable anode material for lithium-ion cells due to its low voltage and high energy density, but is currently not used in secondary lithium-ion cells due to major safety concerns. During the charging process, lithium is not equally deposited on the electrode, but rather tends to form irreversible dendrites (small, multi-branching, tree-like structures). Beside the induced capacity fade due to the loss of cyclable lithium, after numerous charging and discharging processes, the size of the dendrite can become so large that it penetrates the separator, leading to a short circuit of the cell and in a worst case scenario to a thermal runaway of the cell. A safer and the most common anode material used in commercial lithium-ion cells is graphite, a crystalline form of carbon which allows the intercalation of up to one lithium ion per six carbon atoms (LiC_6) (Dahn, 1991). During the first charging process, a surface layer – denoted as solid electrolyte interphase (SEI) – is formed on the anode, consuming lithium and electrolyte to some extent, but also passivating the electrode to minimise further side reactions.

Cathode Materials

Depending on the requirements regarding energy density, power capability, price, and cycle stability, a large variation of cathode materials is used in lithium-ion cells. The first commercially available cell, introduced in 1991 by Sony, contained lithium cobalt oxide

($LiCoO_2$) as cathode material. Extensive research efforts led to the reduction of cost by replacing the expensive and toxic cobalt (Co) partially with other transition metals such as nickel (Ni), manganese (Mn) and aluminium (Al).

Focussing on automotive application, the field of possible cathode materials can be narrowed down to $LiNi_{0.8}Co_{0.15}Al_{0.05}O_2$ (NCA) (Madhavi, Rao, Chowdari, & Li, 2001) and $LiNi_xMn_yCo_zO_2$ (NMC) (Pan et al., 2013). Various combinations of NMCXYZ are available, denoted as, for example, NMC111, NMC442, and NMC622, where the ratio of the used metals has been varied. Other materials like $LiFePO_4$ (LFP) or $LiMn_2O_4$ (LMO) play currently only a minor role in automotive applications due to their low voltage (Padhi, Nanjundaswamy, & Goodenough, 1997) or low cycle stability (Choi & Manthiram, 2006).

Separator

Separators in lithium-ion cells have to fulfil a large number of requirements. Beside a low price, high mechanical as well as chemical stability in various media over a large voltage range is required. A high porosity in combination with a small pore size enables fast lithium diffusion through the layer. In wound cells like cylindrical or prismatic cells, most commonly polymer separators are used. Stacked cells also allow the use of glass fibre or ceramic coated polymer separators, which are usually not as flexible as their polymer-only counterparts, but offer high mechanical stability and easier handling during production.

Electrolyte

Non-aqueous electrolytes are used for lithium-ion cells, containing a combination of various organic solvents and a conducting salt. The solvent is, depending on the application and the used active materials in the cell, a mixture of different carbonates (e. g. ethylene carbonate (EC), dimethyl carbonate (DMC)). The conducting salt in commercial cells is lithium hexafluoride ($LiPF_6$).

Various additives enhancing the cell performance are reported in literature. A special focus is set on the graphite surface layer, as a smooth and homogeneous passivation of the anode is a crucial requirement for a long cycle life. Furthermore, a stabilising effect on the electrolyte for high and very low voltages is desired, as the electrolyte is only electrochemically stable within a certain potential range, usually ranging from 0.4 V to 4.8 V (Xu, Ding, & Jow, 1999).

3.1.2 Battery Degradation

During operation but also when the cell is stored under open circuit conditions (i. e. not charged or discharged), a continuous loss of power capability and energy density can be observed in lithium-ion cells, commonly denoted as ageing of the battery (Barré et al., 2013; Broussely et al., 2005; Vetter et al., 2005).

The power capability loss originates from an increased overpotential due to higher impedance. The energy density loss is caused by capacity fade and impedance rise. The

energy density shall be used to quantify the ageing effects in the further course of this work.

The cause for the capacity fade is divided into two effects. The first one is loss of active material, where the active material of the electrodes loses electrical contact to the current collector or is consumed by parasitic chemical side reactions. As a consequence, it loses its capability to reversibly intercalate lithium-ions. The second possibility is the loss of lithium inventory. During operation, the electrochemical stability window of the electrolyte is frequently violated. As described in Section 3.1.1, this leads to the formation of a surface layer denoted as SEI during the first cycles, which is supposed to insulate the anode and prevent further reaction. Due to the mechanical stress during cycling, the layer is constantly damaged, which leads to further side reactions, consuming lithium, which is actually supposed to shuttle between the two electrodes. This process is accelerated by elevated temperatures (Safari & Delacourt, 2011). The increasing thickness of the layer leads to a higher impedance of the cell, as the intercalation of the lithium-ions is impeded. This is reflected by a larger potential drop during the discharging process or an increased potential rise when charging.

The described ageing mechanisms occur both during cycle and calendar ageing. However, the ratio of the effects may vary for the two ageing modes.

The inactive components of a cell as separator (Peabody & Arnold, 2011) and current collector (Braithwaite et al., 1999) also undergo certain degradation, but their effect on the overall performance of the cell is rather small.

3.2 Battery Ageing Tests

In order to perform the ageing tests, a set of lithium-ion rechargeable cells of the model ICR18650-22FM manufactured by Samsung SDI was used. The cells have a capacity of 2200 mAh and a nominal voltage of 3.6 V, resulting in a nominal energy content of 7.92 Wh (Samsung SDI Co., Ltd., 2008). Regarding battery testing, the constant current (dis)charge mode established as a standard and therewith the use of the C-rate to determine the (dis)charge current. The C-rate is commonly defined by the relation of charge or discharge current to the nominal capacity:

$$\text{C-rate} = \text{(dis)charge current} / \text{nominal capacity} \tag{3.1}$$

It indicates what share of the nominal capacity can be (dis)charged within 1 h. This means that for a C-rate of 1 C it takes 1 h to fully charge or discharge a battery, for 2 C 0.5 h, and for 0.5 C 2 h. The maximum charge and discharge rate for the test cells is 1 C and 2 C, respectively (Samsung SDI Co., Ltd., 2008).

3.2.1 Cycle Ageing Tests

Cycle tests were conducted according to the test matrix in Table 3.1 in order to examine the ageing of the cell under various operating conditions. The test matrix was designed to investigate the different parameters affecting the performance of the cell while keeping the effort of the test matrix to a reasonable size. For the purpose of the charging

optimisation model, which deals with physical quantities as energy and power, a P-rate analogous to the C-rate was introduced. As the C-rate is based on current and nominal capacity, the P-rate is based on power and nominal energy content:

$$\text{P-rate} = \text{(dis)charge power} / \text{nominal energy content} \tag{3.2}$$

During the cycle ageing tests, the cells were charged with constant power (CP) and an optional constant voltage (CV) phase where necessary. Towards the end of a full charge, the cell reaches its cut-off voltage, defined by the manufacturer. To reach a state of charge (SOC) of 100 %, the voltage is kept constant at the level of the cut-off voltage and the charging process is continued with decreasing current and power. This is called constant voltage (CV) phase. The higher the charge rate, the earlier the cut-off voltage is reached due to the increasing overpotential, caused by the cell's impedance.

Test no.	SOC_{start}	SOC_{end}	DOD	Charge rate	Discharge rate	Temperature
1	0 %	80 %	80 %	0.2 P	1 C	26 °C
2	0 %	80 %	80 %	0.5 P	1 C	26 °C
3	0 %	80 %	80 %	1 P	1 C	26 °C
4	0 %	80 %	80 %	1.5 P	1 C	26 °C
5	30 %	60 %	30 %	1 P	1 C	26 °C
6	30 %	80 %	50 %	1 P	1 C	26 °C
7	30 %	100 %	70 %	1 P	1 C	26 °C
8	10 %	60 %	50 %	1 P	1 C	26 °C
9	50 %	100 %	50 %	1 P	1 C	26 °C
10	35 %	80 %	45 %	1 P	ARTEMIS	26 °C

Table 3.1 – Test matrix for cycle ageing tests

Another reason for choosing constant power charge mode – beside the advantage of compatibility with the charging optimisation model – was that it is used for BEV charging as measured by the student project InCharge (Lehrstuhl für Energiewirtschaft und Anwendungstechnik, Technische Universität München, Jan Vincke, 2013) during charging processes of a CITROËN C-Zero. Furthermore, previous ageing tests performed in the context of a charge rate dependent ageing model for a charging optimisation by Trippe et al. (2014) showed no considerable difference in ageing behaviour between constant current (CC) and constant power (CP) charge mode (see Figure A.1 in Appendix A).

In test no. 1 to 4, the impact of the charge power was investigated by cycling the cells between 0 % and 80 %. The range of SOC in which a battery is cycled is the depth of discharge (DOD), in this case 80 %. The cells were discharged with a constant current of 1 C and charged the with a constant power of 0.2, 0.5, 1, and 1.5 P. Tests no. 5 to 9 were conducted with a constant charge and discharge rate of 1 P and 1 C, respectively. As a full charge and discharge of the cell is unlikely to occur in operation, the effect of different SOC_{start} and SOC_{end} and the resulting variations in the DOD were studied. Test no. 10 included the ARTEMIS drive cycle and will be discussed in detail later in this section.

The test temperature was set to be 26 °C, which was considered a reasonable ambient temperature in real-live applications in Singapore. The tests were conducted in a Memmert IPP 200 incubator with a Peltier cooling element. To reduce the temperature variations in the chamber, generated during the cycling of the cells, additional fans were added. Each set of cells was equipped with a temperature sensor to monitor the temperature increase, especially under high current conditions. The maximum temperature was measured to be 30 °C for cells of test no. 4 at the end of the 1.5 P charging process.

Three cells were tested for each test condition in order to identify and exclude outliers and manufacturing defects of the testing cells. Generally, the ageing behaviour of the different cells for one test condition coincided very well. Only for test no. 4 and 6, one and two cells, respectively, showed an early sudden sharp decline in the otherwise linear drop. Hence, the affected cells were neglected in the further analysis of the cycle ageing test data.

In order to measure and document the ageing process, characterisation cycles were conducted in periodical intervals after a certain number of ageing test cycles. The characterisation cycles consisted of a pause followed by a full charge and discharge at 0.2 C each. At this C-rate, the manufacturer determines the nominal capacity. Thereby, the measured values of residual capacity and energy content during the characterisation cycles become comparable to the nominal values given by the manufacturer and the different cycle ageing tests can be compared to each other.

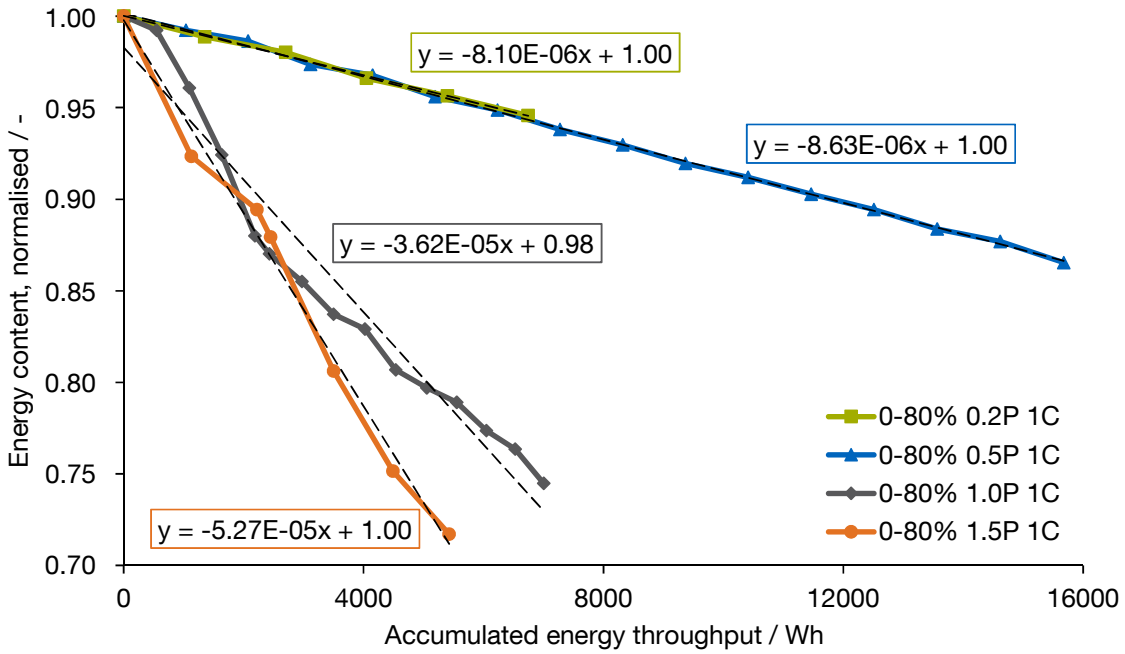

Figure 3.2 – Energy content of test cells versus accumulated charging energy throughput for different charge rates

As mentioned before, the physical quantity used to describe the ageing behaviour in the charging optimisation model is the energy content of the cells. The energy content (as

product of capacity and voltage) already includes the two different mechanisms lowering the cell's performance during the ageing study: the decreasing capacity as well as a declining average discharge voltage caused by an increasing cell impedance. Figure 3.2 displays the energy content, normalised to the nominal energy content of the cell, versus the duration of the cycle ageing tests with different charge rates of 0.2 P, 0.5 P, 1.0 P, and 1.5 P (test no. 1 to 4). The normalised energy content of the cells has an initial value of 1, equal to 100 % of the cells' nominal energy content.

The total energy throughput consists of energy during charging and discharging processes, while one is positive and the other negative. The energy content in Figure 3.2 is plotted versus the accumulated energy throughput during charging processes only, as the ageing during these is the focus of the charging optimisation model. In a later step, the share of ageing during discharging processes will be eliminated from the ageing model. An energy throughput of 4000 Wh corresponds to 505 full cycles. As we see in Figure 3.2, the energy content decreases linearly and the curves are approximated by straight lines. The corresponding linear equations are given in the graph. The drop of the energy content for 0.2 P and 0.5 P charge rate lies in the same range while 0.5 P causes a slightly higher energy fade. For 1.0 P and 1.5 P, the difference is more obvious: the higher the P-rate, the higher the drop of energy content.

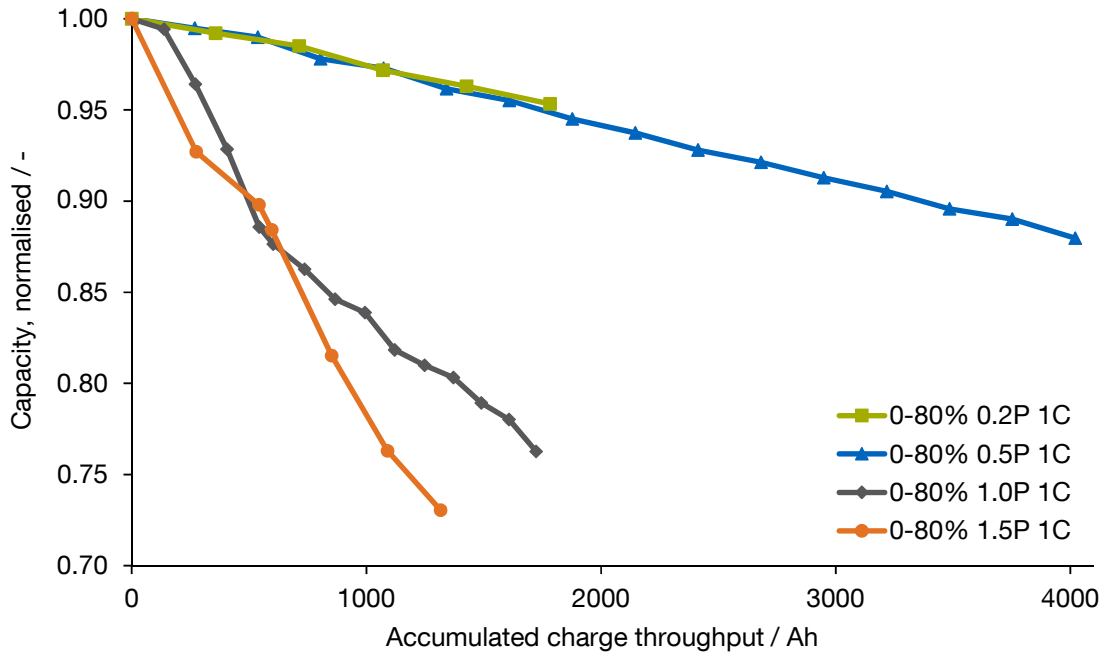

Figure 3.3 – Capacity of test cells versus accumulated charging charge throughput for different charge rates

The development of the capacity of the cells of test no. 1 to 4 is pictured in Figure 3.3. The axis of ordinates gives the normalised capacity based on the nominal capacity while the axis of abscissae shows the accumulated charge throughput during the cycle ageing tests. Analogously to the energy throughput, only the charge throughput during charging processes and not during discharging processes is plotted. The run of the

curve of the capacity resembles the one of the energy content in Figure 3.2 and higher charge power causes also a faster drop in capacity. The capacity fade was examined and displayed as validation of the energy fade data.

Figure 3.4 depicts the results of the cycle ageing tests between different SOCs (test no. 5 to 10). As in Figure 3.2, the normalised energy content is plotted versus the accumulated energy throughput and again, the curves are approximated with straight lines. As for tests no. 1 to 4, the energy content and the capacity over the duration of tests no. 5 to 10 show a qualitatively similar development (cf. Figure 3.4 and Figure A.2 in Appendix A). Based on the data presented in Figure 3.4, it can be concluded that a larger DOD leads to a higher energy fade. Cycling with a DOD of 70 % between 30 and 100 % is worse than between 30 and 80 % and 30 and 60 %. But the SOCs also have

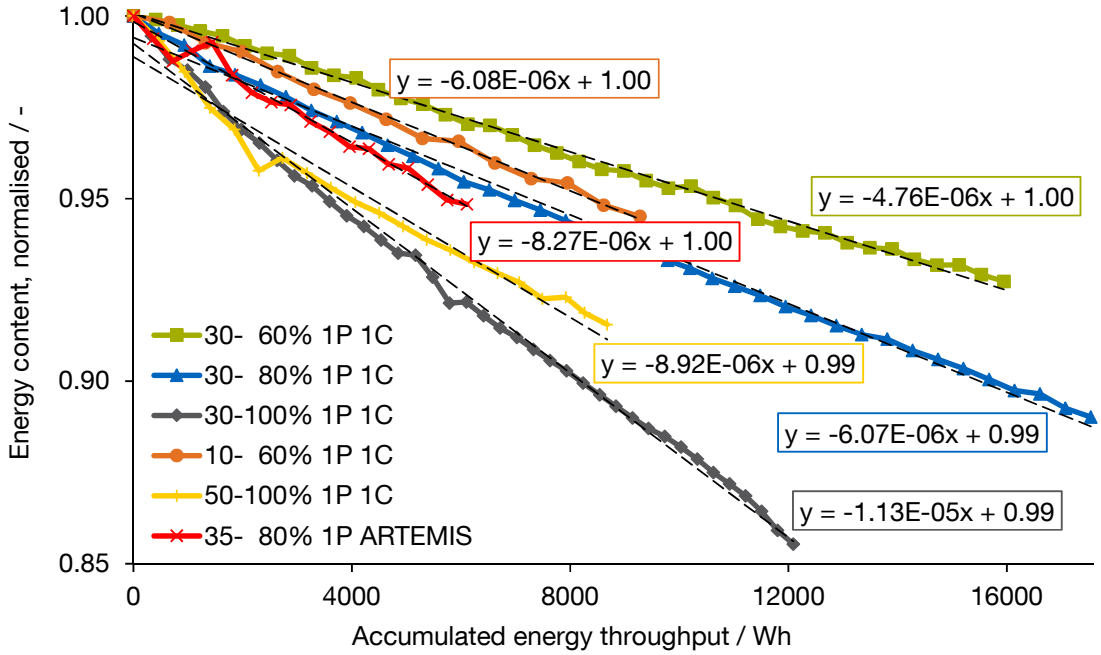

Figure 3.4 – Energy content of test cells versus accumulated charging energy throughput for different SOCs

an effect. Comparing cycling from 10 % to 60 %, 30 % to 80 %, and 50 % to 100 % shows that cycling in higher SOC ranges – i. e. the closer one gets to an SOC of 100 % – causes faster battery ageing. Beside charging to very high SOCs, discharging to very low SOCs accelerates battery ageing, as well. This can be deduced from a comparison of test no. 7 (30 % to 100 %, 1 P/1 C) to test no. 3 (0 % to 80 %, 1 P/1 C) in Figure 3.2, which reaches a normalised energy content of 0.85 already after approximately 4000 Wh accumulated energy throughput. Even though the DOD of test no. 3 is only 10 % higher than that of test no. 7, the energy fade for test no. 3 is more than three times as high. Hence, a deep discharge to an SOC of 0 % has a substantial influence on battery ageing.

ARTEMIS Discharge Profile

As mentioned before, for one of the cycle ageing tests (test no. 10), a different discharge mode than constant current was chosen. Test no. 10 was charged at 1 P and discharged with a power profile corresponding to a driving cycle called ARTEMIS. It was developed within the ARTEMIS project, which aimed to generate real-world driving cycles (André, 2004). The cycle ageing test using this driving cycle was conducted to be able to assess the question how realistic ageing tests with a constant discharge rate of 1 C are for an application associated with BEVs. ARTEMIS consists of three different driving cycles, namely urban, rural, and motorway (André, 2004). A sequence of these was concatenated (urban – rural – motorway – rural – urban) whereas the motorway driving cycle has been cut at a maximum speed of 130 km/h in order to reflect the speed limits on most motorways. The speed profile corresponding to the driving cycles was converted into a power profile drawn from the battery of a BEV. Thus, a discharging pattern as it would occur in BEVs while driving was created. The conversion of speed to power profiles was performed analogously to the procedures and equations described in Section 2.3. The power profiles were computed for a BEV with a battery pack with a usable energy content of 18.8 kWh and maximum power of 125 kW (BMW AG, 2016).

For the usage within ageing test no. 10, the discharge power profile generated from the driving cycles was scaled down proportionally to the energy content from 18.8 kWh of the battery pack to 7.92 Wh of the testing cell. The ageing test starts at SOC 80 %. 980 mAh are discharged during one cycle, equivalent to 45 % DOD of the 2200 mAh cell. Accordingly, during the ARTEMIS ageing test, the cells were cycled between 35 % and 80 % SOC. As the SOC range of ageing test no. 6 (30 % to 80 %, 1 P, 1 C; blue curve in Figure 3.4) is very similar to the one of the Artemis ageing test no. 10 (35 % to 80 %, 1 P, ARTEMIS; red curve), these two tests are used for a comparison. As expected, similar ageing behaviour can be observed in Figure 3.4. The gradients of the two corresponding linear fits are $-6.07 \cdot 10^{-6}\,\mathrm{Wh}^{-1}$ for test no. 6 and $-8.27 \cdot 10^{-6}\,\mathrm{Wh}^{-1}$ for test no. 10. The energy fade of the ageing test with a 1 C discharge profile lies 27 % below the energy fade of the ageing test with the ARTEMIS discharge profile. This difference is assigned to the Artemis discharge profile in contrast to a 1 C discharge profile. As the energy fade values of the two tests lie in the same order of magnitude, discharging the cells with a constant current rate of 1 C instead of using a realistic discharge profile according to ARTEMIS driving cycles is a reasonable method to accelerate and simplify the cycle ageing tests. The ageing behaviour during the charging process, which is the focus of the charging optimisation model, is assumed not to be influenced noticeably by the different discharge methods. Hence, the results of the cycle ageing tests are relevant and suitable for the modelling of electric vehicle charging.

(Dis)Charge Efficiencies

In order to introduce efficiencies during the charging and discharging processes, we temporarily switch the perspective from cell to battery pack level. While charging and discharging the battery of a BEV, energy losses occur at several points. On the energy's way from the power grid to the BEV's propulsion system, two efficiency factors play a

role. Their relation is explained in the following equations.

$$E_{batt} = E_{grid} \cdot \eta_{chaSt} \tag{3.3}$$

$$E_{cons} = E_{batt} \cdot \eta_{batt} \tag{3.4}$$

When a battery is charged, the energy drawn from the grid E_{grid} reduced according to the efficiency factor of the charging station η_{chaSt} is stored in the battery of the BEV: E_{batt}. While charging and discharging a battery, the cell's impedance leads to an overpotential and heat losses due to Joule heating inside the battery. These losses are reflected in the efficiency factor of the battery η_{batt}. The energy E_{batt} diminished by the heat losses in the battery according to η_{batt} can be consumed by the power train and other systems of the BEV to operate and propel the vehicle: E_{cons}. Further losses from E_{cons} during its conversion to kinetic energy were considered earlier in the simulation of the mobility behaviour and are explained in equations (2.1) to (2.3) in Section 2.3.

η_{chaSt} includes the losses from the grid to the battery. For alternating current (AC) charging stations, losses between the power socket and the plug of the BEV are mainly wire resistance of the charging cable and are neglected here, resulting in an AC charging station efficiency of 100 %. Losses between the BEV plug and the battery occur at the on-board charger including the rectifier, which features an efficiency of 93 % (BRUSA Elektronik AG, 2015). Direct current (DC) charging stations hold a lower efficiency of 94 % (ABB EV Charging Infrastructure, 2014) compared to AC charging stations (100 %), since the rectifier is included in the charging station. However, the combined losses of charging station and rectifier do not differ very much for the two options of AC or DC charging. Hence, a value of 93 % is assumed for the efficiency from grid to battery η_{chaSt} for both AC and DC charging stations.

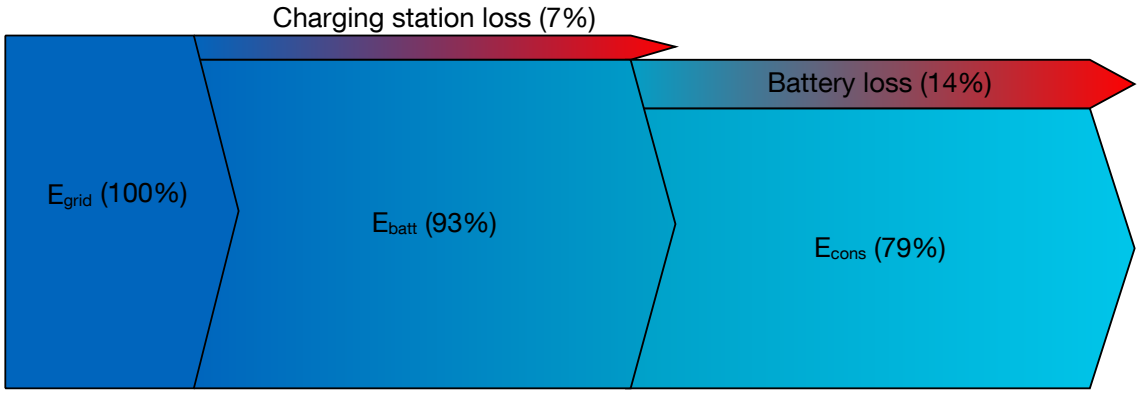

Figure 3.5 – Sankey diagram of energy flows while charging and discharging a BEV

It is assumed that the battery efficiency η_{batt} on battery pack level is the same as on cell level. In order to determine the losses while cycling a battery and obtain a value for η_{batt}, the energy flow of the first cycle into and out of the cells was measured by the battery tester for different cycle ageing tests (tests no. 3, 6, and 10) and compared to each other. For test no. 3 between 0 % and 80 % SOC with 80 % DOD, the battery tester charged 7.038 Wh into the cell and discharged 5.907 Wh from the cell. This yields an

efficiency of 83.93 % for η_{batt}. η_{batt} of test no. 6 holds a value of 82.39 %, while for test no. 10 the value is 88.29 %. It can be seen that the efficiency values vary for different test conditions, originating from the increasing losses with increasing (dis)charge rate. However, since the maximum difference between the values is less than 6 %, the average value is used for the further calculations in this work. Thus, the battery efficiency factor η_{batt} results in a value of 85 %. Another aspect of the battery efficiency – which is however neglected in the charging optimisation model – is that losses increase along with the ageing process of the cells. In future work, different battery efficiencies can be included depending on the state of health of the BEV's battery pack.

Figure 3.5 visualises the energy flows and accompanying losses from the grid to the battery to the propulsion system during charging and discharging, which are derived from the efficiency factors

$$\eta_{chaSt} = 93\,\%,$$
$$\eta_{batt} = 85\,\%.$$

3.2.2 Calendar Ageing Tests

During the calendar ageing tests, cells were stored at different temperatures as well as different SOCs and after periodical time intervals, characterisation cycles were conducted. Table 3.2 contains the test conditions for the different calendar ageing tests with test no. 11 to 30.

Test no.	SOC	Temperature	Test no.	SOC	Temperature
11	20 %	20 °C	21	20 %	40 °C
12	40 %	20 °C	22	40 %	40 °C
13	60 %	20 °C	23	60 %	40 °C
14	80 %	20 °C	24	80 %	40 °C
15	100 %	20 °C	25	100 %	40 °C
16	20 %	26 °C	26	20 %	60 °C
17	40 %	26 °C	27	40 %	60 °C
18	60 %	26 °C	28	60 %	60 °C
19	80 %	26 °C	29	80 %	60 °C
20	100 %	26 °C	30	100 %	60 °C

Table 3.2 – Test matrix for calendar ageing tests

For this work, the calendar ageing tests performed at 26 °C (tests no. 16 to 20) are of importance as the cycle ageing tests were operated at the same temperature and thus, both are comparable. The tests at higher temperatures are used to accelerate the degradation and the obtained data help to give an estimate on whether it is reasonable to extrapolate the data gained at 26 °C. Based on the Arrhenius equation (Jossen & Weydanz, 2006, p. 21), an increase of 10 °C will lead to a doubling of the side reactions in the cell, which are responsible for the continuous fade of cell performance during storage.

The decrease of the normalised energy content of the test cells over the duration of the calendar ageing tests at 26 °C are pictured in Figure 3.6. The development of the normalised energy content at 20 °C, 40 °C, and 60 °C (tests no. 11 to 15, 21 to 25, 26 to 30) can be found in Figures A.3, A.4, and A.5 in Appendix A.

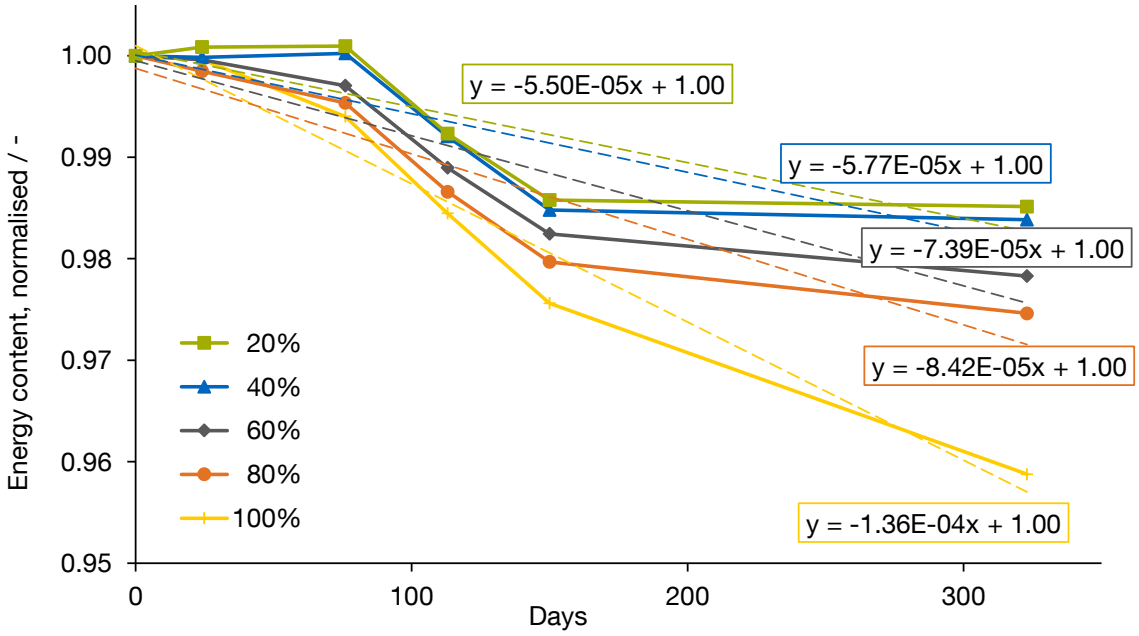

Figure 3.6 – Energy content of test cells versus time for different static SOCs at 26 °C

It is observed – especially at 20 °C, 40 °C, and 60 °C – that the decrease of energy content over the course of time is linear for the different temperatures and SOCs. At 26 °C (see Figure 3.6), the energy content does not decrease as linearly as for the other temperatures. However, small variations in the energy content determination can be caused by slight, unintentional changes of the characterisation test conditions. Those variations can become visible when the general decrease of the energy content is very small, as it is the case here. In more than 300 days, the energy content declines by only 4 % in the worst case of storage at 100 % SOC, and for the other SOCs even only 2 % or less. Therefore, for all calendar ageing tests including the ones at 26 °C, the decrease of the energy content is assumed to be linear and the curves are approximated with straight lines, analogously to the procedures for the cycle ageing tests as explained in Section 3.2.1. Generally, it can be said that a higher SOC causes a faster decrease of the cell's energy content, which is in well agreement with available literature (Keil et al., 2016).

3.3 Derivation of Battery Ageing Parameters

The battery ageing tests discussed in the preceding Section 3.2 are further elaborated in order to obtain applicable parameters for a battery ageing model, later to be used in the charging optimisation model. Firstly, the calendar ageing at different SOCs is evaluated.

Secondly, the ageing behaviour during cycling with different charge rates and between different SOCs is analysed.

3.3.1 Energy Fade due to Calendar Ageing

The values describing the ageing behaviour during the different calendar ageing tests can be derived from the straight lines given in Figures 3.6, A.3, A.4, and A.5. The gradients of these lines represent the normalised energy fade at the various static SOCs for different temperatures. Table 3.3 summarises the energy fade values derived from those graphs. As the normalised energy content is dimensionless, the energy fade is given as relative

Test no.	SOC	Temperature	Energy fade / day^{-1}	Energy fade / h^{-1}
11	20 %	20 °C	$4.34 \cdot 10^{-5}$	$1.81 \cdot 10^{-6}$
12	40 %	20 °C	$5.24 \cdot 10^{-5}$	$2.18 \cdot 10^{-6}$
13	60 %	20 °C	$6.89 \cdot 10^{-5}$	$2.87 \cdot 10^{-6}$
14	80 %	20 °C	$7.88 \cdot 10^{-5}$	$3.28 \cdot 10^{-6}$
15	100 %	20 °C	$1.13 \cdot 10^{-4}$	$4.71 \cdot 10^{-6}$
16	20 %	26 °C	$5.50 \cdot 10^{-5}$	$2.29 \cdot 10^{-6}$
17	40 %	26 °C	$5.77 \cdot 10^{-5}$	$2.40 \cdot 10^{-6}$
18	60 %	26 °C	$7.39 \cdot 10^{-5}$	$3.08 \cdot 10^{-6}$
19	80 %	26 °C	$8.42 \cdot 10^{-5}$	$3.51 \cdot 10^{-6}$
20	100 %	26 °C	$1.36 \cdot 10^{-4}$	$5.67 \cdot 10^{-6}$
21	20 %	40 °C	$4.81 \cdot 10^{-5}$	$2.00 \cdot 10^{-6}$
22	40 %	40 °C	$5.98 \cdot 10^{-5}$	$2.49 \cdot 10^{-6}$
23	60 %	40 °C	$1.24 \cdot 10^{-4}$	$5.17 \cdot 10^{-6}$
24	80 %	40 °C	$1.45 \cdot 10^{-4}$	$6.04 \cdot 10^{-6}$
25	100 %	40 °C	$3.78 \cdot 10^{-4}$	$1.58 \cdot 10^{-5}$
26	20 %	60 °C	$1.82 \cdot 10^{-4}$	$7.58 \cdot 10^{-6}$
27	40 %	60 °C	$2.74 \cdot 10^{-4}$	$1.14 \cdot 10^{-5}$
28	60 %	60 °C	$3.10 \cdot 10^{-4}$	$1.29 \cdot 10^{-5}$
29	80 %	60 °C	$3.64 \cdot 10^{-4}$	$1.52 \cdot 10^{-5}$
30	100 %	60 °C	$6.83 \cdot 10^{-4}$	$2.85 \cdot 10^{-5}$

Table 3.3 – Energy fade for different calendar ageing tests

energy fade per day. Additionally, the values are transformed to energy fade per hour for comparison to the cycle ageing tests and for a better handling within the charging optimisation model later on. The energy fade per hour due to calendar ageing is called $e_{fade,cal}$.

In Figure 3.7a, the energy fade per hour from Table 3.3 is plotted versus the static SOCs at different temperatures. The values at 20 °C and 26 °C show a similar development along the increasing static SOC, which can be explained by the relatively small difference in temperature. Only for an SOC of 100 %, the energy fade at 26 °C is slightly higher than at 20 °C. At 40 °C for 20 % and 40 % SOC, the energy fade coincides with the values at the lower temperatures. For higher SOCs, the energy fade increases faster with a steep rise between 80 % and 100 %. The calendar ageing tests at 60 °C produced a similar

trend as the 40 °C values, however with higher absolute energy fade values. All calendar ageing tests showed faster ageing with higher static SOCs, while higher temperatures accelerate the ageing processes further, especially at very high SOCs.

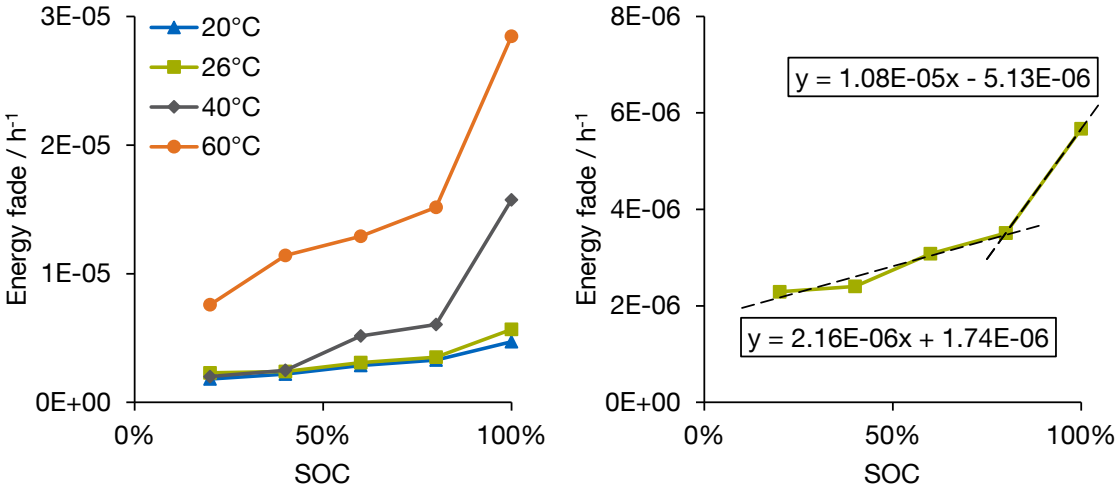

(a) 20 °C, 26 °C, 40 °C, and 60 °C (b) 26 °C

Figure 3.7 – Energy fade per hour for different static SOCs at different temperatures due to calendar ageing

Since all cycle ageing tests were conducted at 26 °C and the ambient temperature is assumed to be in this temperature range, a closer look is taken at the calendar ageing test series at 26 °C in Figure 3.7b. Those ageing tests (tests no. 16 to 20) are most suitable for a comparison to the cycle ageing tests and for future application in the charging optimisation model. The curve in Figure 3.7b is approximated by two straight lines, as displayed. The linear equations fitted to the measured data points yield calendar ageing parameters to be used in the charging optimisation model:

$$e_{fade,cal} = \begin{cases} 2.16 \cdot 10^{-6}\,\mathrm{h}^{-1} \cdot SOC + 1.74 \cdot 10^{-6}\,\mathrm{h}^{-1}, & \text{for } SOC \leq 80\,\% \\ 1.08 \cdot 10^{-5}\,\mathrm{h}^{-1} \cdot SOC - 5.13 \cdot 10^{-6}\,\mathrm{h}^{-1}, & \text{for } SOC > 80\,\% \end{cases} \tag{3.5}$$

3.3.2 Ageing Factor for Different Charge Rates and State of Charge Dependent Energy Fade

The cycle ageing tests are analysed in order to derive parameters describing the cycle ageing behaviour. The gradients of the straight lines in Figures 3.2 and 3.4, which display the decreasing energy content, reveal values for the energy fade during the different cycle ageing tests. The gradients indicate the normalised energy fade per Wh that is charged and are summarised in Table 3.4 as $e_{fade,tot}$.

The total energy fade $e_{fade,tot}$ during cycling the test cells consists of energy fade due to calendar and cycle ageing. Multiplying the values per Wh by the amount of cycled energy ($E_{nom} \cdot DOD = 7.92\,\mathrm{Wh} \cdot DOD$) results in the total energy fade per cycle.

For reasons of comparison, the energy fade due to calendar ageing $e_{fade,cal}$ at 26 °C is derived from Table 3.3 by means of linear interpolation and the following values result

Test no.	SOC_{start} to SOC_{end}	Average SOC	Charge / discharge rate	Energy fade total $e_{fade,tot}$ / Wh^{-1}	Energy fade total $e_{fade,tot}$ / $cycle^{-1}$
1	0 % to 80 %	40 %	0.2 P / 1 C	$8.10 \cdot 10^{-6}$	$5.13 \cdot 10^{-5}$
2	0 % to 80 %	40 %	0.5 P / 1 C	$8.63 \cdot 10^{-6}$	$5.47 \cdot 10^{-5}$
3	0 % to 80 %	40 %	1 P / 1 C	$3.62 \cdot 10^{-5}$	$2.29 \cdot 10^{-4}$
4	0 % to 80 %	40 %	1.5 P / 1 C	$5.27 \cdot 10^{-5}$	$3.34 \cdot 10^{-4}$
5	30 % to 60 %	45 %	1 P / 1 C	$4.76 \cdot 10^{-6}$	$1.13 \cdot 10^{-5}$
6	30 % to 80 %	55 %	1 P / 1 C	$6.07 \cdot 10^{-6}$	$2.40 \cdot 10^{-5}$
7	30 % to 100 %	65 %	1 P / 1 C	$1.13 \cdot 10^{-5}$	$6.26 \cdot 10^{-5}$
8	10 % to 60 %	35 %	1 P / 1 C	$6.08 \cdot 10^{-6}$	$2.41 \cdot 10^{-5}$
9	50 % to 100 %	75 %	1 P / 1 C	$8.92 \cdot 10^{-6}$	$3.53 \cdot 10^{-5}$

Test no.	Duration charge + discharge	Energy fade calendar ageing $e_{fade,cal}$ / $cycle^{-1}$	Energy fade cycle ageing $e_{fade,cyc}$ / $cycle^{-1}$	Energy fade cycle ageing $e_{fade,cyc}$ / Wh^{-1}
1	4 h + 0.8 h	$1.15 \cdot 10^{-5}$	$3.98 \cdot 10^{-5}$	$6.28 \cdot 10^{-6}$
2	1.6 h + 0.8 h	$5.77 \cdot 10^{-6}$	$4.89 \cdot 10^{-5}$	$7.72 \cdot 10^{-6}$
3	0.8 h + 0.8 h	$3.85 \cdot 10^{-6}$	$2.26 \cdot 10^{-4}$	$3.56 \cdot 10^{-5}$
4	0.53 h + 0.8 h	$3.21 \cdot 10^{-6}$	$3.31 \cdot 10^{-4}$	$5.22 \cdot 10^{-5}$
5	0.33 h + 0.33 h	$1.72 \cdot 10^{-6}$	$9.59 \cdot 10^{-6}$	$4.04 \cdot 10^{-6}$
6	0.5 h + 0.5 h	$2.91 \cdot 10^{-6}$	$2.11 \cdot 10^{-5}$	$5.34 \cdot 10^{-6}$
7	0.7 h + 0.7 h	$4.46 \cdot 10^{-6}$	$5.82 \cdot 10^{-5}$	$1.05 \cdot 10^{-5}$
8	0.5 h + 0.5 h	$2.38 \cdot 10^{-6}$	$2.17 \cdot 10^{-5}$	$5.48 \cdot 10^{-6}$
9	0.5 h + 0.5 h	$3.40 \cdot 10^{-6}$	$3.19 \cdot 10^{-5}$	$8.06 \cdot 10^{-6}$

Table 3.4 – Energy fade for different cycle ageing tests (part I)

for the different average SOCs of the cycle ageing tests:

$$
\begin{aligned}
e_{fade,cal}(40\,\%, 26\,^\circ\mathrm{C}) &= 2.40 \cdot 10^{-6}\,\mathrm{h}^{-1} \quad \text{(for test no. 1–4)},\\
e_{fade,cal}(45\,\%, 26\,^\circ\mathrm{C}) &= 2.57 \cdot 10^{-6}\,\mathrm{h}^{-1} \quad \text{(for test no. 5)},\\
e_{fade,cal}(55\,\%, 26\,^\circ\mathrm{C}) &= 2.91 \cdot 10^{-6}\,\mathrm{h}^{-1} \quad \text{(for test no. 6)},\\
e_{fade,cal}(65\,\%, 26\,^\circ\mathrm{C}) &= 3.19 \cdot 10^{-6}\,\mathrm{h}^{-1} \quad \text{(for test no. 7)},\\
e_{fade,cal}(35\,\%, 26\,^\circ\mathrm{C}) &= 2.38 \cdot 10^{-6}\,\mathrm{h}^{-1} \quad \text{(for test no. 8)},\\
e_{fade,cal}(75\,\%, 26\,^\circ\mathrm{C}) &= 3.40 \cdot 10^{-6}\,\mathrm{h}^{-1} \quad \text{(for test no. 9)}.
\end{aligned}
$$

Using these values and the duration of one cycle (charge and discharge) given in Table 3.4, the calendar ageing share during the cycle ageing tests is calculated and displayed as $e_{fade,cal}$ per cycle in Table 3.4.

The cycle ageing share during the cycle ageing tests $e_{fade,cyc}$ is found by subtracting the calendar ageing share $e_{fade,cal}$ from the total energy fade $e_{fade,tot}$:

$$e_{fade,cyc} = e_{fade,tot} - e_{fade,cal} \tag{3.6}$$

Dividing $e_{fade,cyc}$ per cycle by the amount of cycled energy leads to the energy fade due to cycle ageing $e_{fade,cyc}$ per Wh.

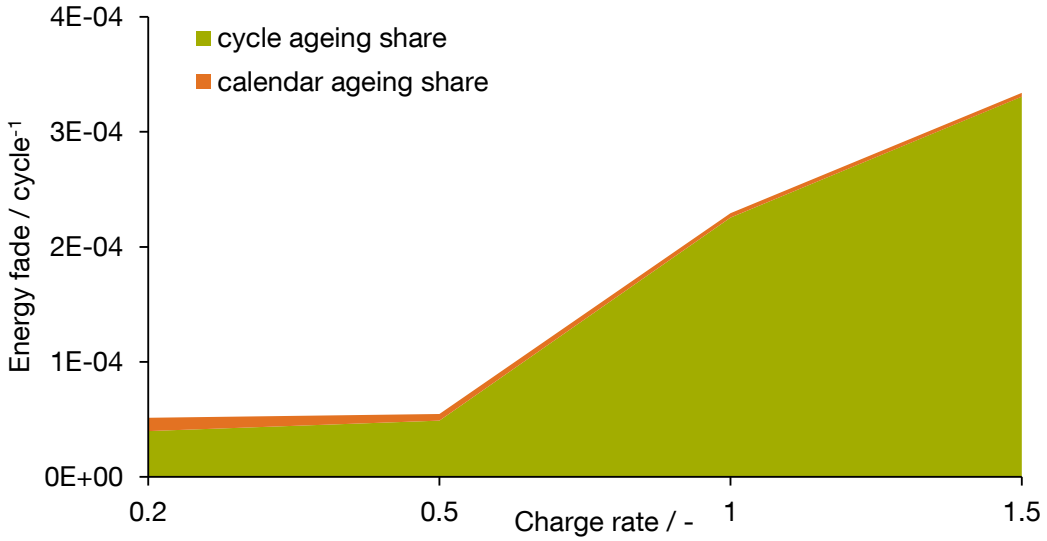

Figure 3.8 – Energy fade during cycle ageing tests versus charge rate: Calendar and cycle ageing share of energy fade per cycle

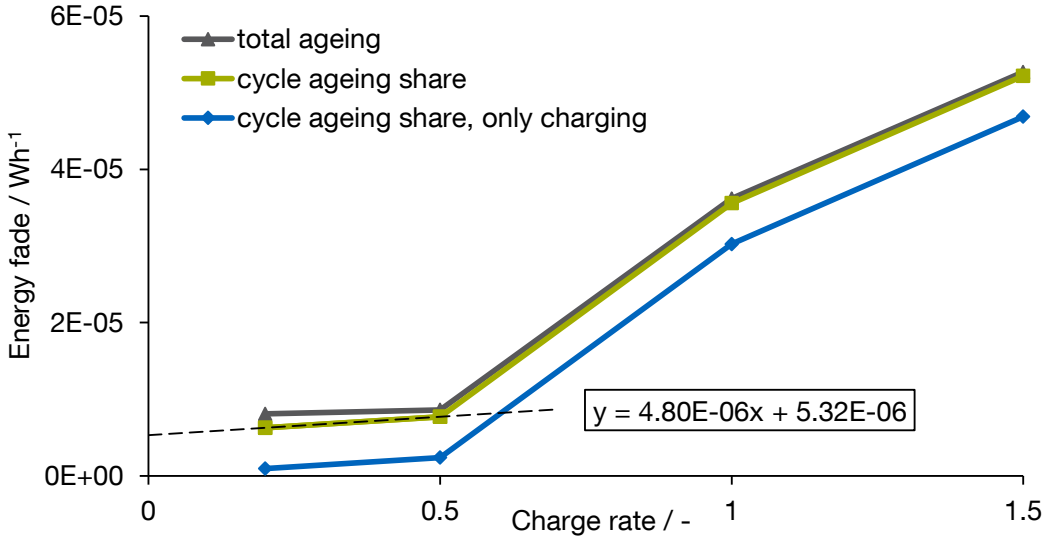

Figure 3.9 – Energy fade during cycle ageing tests versus charge rate: Shares of total ageing, cycle ageing and ageing related to charging process of energy fade per Wh

For tests no. 1 to 4, Figure 3.8 shows the total energy fade during the cycle ageing tests $e_{fade,tot}$ and the shares of calendar and cycle ageing therein, $e_{fade,cal}$ and $e_{fade,cyc}$. The energy fade due to calendar ageing $e_{fade,cal}$ per cycle (displayed in orange) declines along increasing charge rates. The energy fade per hour is the same for tests no. 1 to 4

($2.40 \cdot 10^{-6}$/h), but the cycle duration shortens with higher charge rates. Hence, the energy fade per cycle decreases (cf. Table 3.4).

In Figure 3.9, again the total energy fade and the energy fade due to cycle ageing can be seen, in this case with the unit Wh^{-1}. Looking at energy fade due to cycle ageing in green, one can see the influence of slow and fast charging. It can be understood that the differences between the cycle ageing energy fade values originate solely from the different charge rates (because discharge rate and average SOC were identical for tests no. 1–4) and that a certain constant component of the total energy fade is associated with the discharging process. It is assumed that the energy fade declines linearly between a charge rate of 0.5 P and 0.2 P and linearly continues down to a hypothetical charge rate of 0 P, indicated by the dotted line. Consequently, the cycle ageing energy fade at 0 P – i. e. the y-intercept of the linear equation displayed in Figure 3.9 – can be interpreted as the share of ageing due to the discharging process. Hence, when cycling a cell between 0 % and 80 % SOC at a discharge rate of 1 C, the energy fade assigned to the discharging process amounts to $5.32 \cdot 10^{-6}\,\mathrm{Wh}^{-1}$. This value is subtracted from the energy fade values $e_{fade,cyc}$ of test no. 1 to 4 (green curve, cf. last column of Table 3.4), resulting in the energy fade related to the charging process only, $e_{fade,cha}$, which is represented by the blue curve in Figure 3.9.

$$e_{fade,cha} = e_{fade,cyc} - 5.32 \cdot 10^{-6}\,\mathrm{Wh}^{-1} \tag{3.7}$$

For tests no. 1 to 4, the energy fade assigned to the discharging process of $5.32 \cdot 10^{-6}\,\mathrm{Wh}^{-1}$ is divided by $e_{fade,cyc}$, yielding the ratio of discharge ageing to total ageing:

$$f_{dis} = 5.32 \cdot 10^{-6}\,\mathrm{Wh}^{-1} / e_{fade,cyc} \tag{3.8}$$

Test no. 3 was cycled at 1 P/1 C, as were tests no. 5 to 9. Therefore, it is assumed that the relation between ageing while charging and discharging is the same for these tests. Hence, the ratio of discharge ageing for test no. 3 (14.95 %) is also applied to tests no. 5 to 9. The ratio of discharge ageing f_{dis} is listed in Table 3.5.

Test no.	Ratio of discharge to total ageing f_{dis} / –	Energy fade charging process $e_{fade,cha}$ / Wh^{-1}	Energy fade charging process $e_{fade,cha}$ / –
1	84.73 %	$9.59 \cdot 10^{-7}$	$6.07 \cdot 10^{-6}$
2	68.92 %	$2.40 \cdot 10^{-6}$	$1.52 \cdot 10^{-5}$
3	14.95 %	$3.03 \cdot 10^{-5}$	$1.92 \cdot 10^{-4}$
4	10.19 %	$4.69 \cdot 10^{-5}$	$2.97 \cdot 10^{-4}$
5	14.95 %	$3.43 \cdot 10^{-6}$	$8.16 \cdot 10^{-6}$
6	14.95 %	$4.54 \cdot 10^{-6}$	$1.80 \cdot 10^{-5}$
7	14.95 %	$8.93 \cdot 10^{-6}$	$4.95 \cdot 10^{-5}$
8	14.95 %	$4.66 \cdot 10^{-6}$	$1.85 \cdot 10^{-5}$
9	14.95 %	$6.86 \cdot 10^{-6}$	$2.72 \cdot 10^{-5}$

Table 3.5 – Energy fade for different cycle ageing tests (part II)

As explained before, the energy fade related only to the charging process $e_{fade,cha}$ for tests no. 1 to 4 is calculated as in equation (3.7). Regarding tests no. 5 to 9, $e_{fade,cha}$ is

derived by means of the ratio for discharge ageing:

$$e_{fade,cha} = (100\,\% - f_{dis}) \cdot e_{fade,cyc} \tag{3.9}$$

All values for $e_{fade,cha}$ can be found in the third column of Table 3.5.

So far, the energy fade related to charging only ($e_{fade,cha}$) is given as normalised energy fade per Wh charged with the unit Wh^{-1}. However, for the further use of the battery ageing model in the charging optimisation, the energy fade related to the entire charging process is of importance. Hence, the energy fade per Wh related to the charging process is multiplied by the energy amount charged within one charging process ($E_{nom} \cdot DOD = 7.92\,\mathrm{Wh} \cdot DOD$). As a result, the energy fade during one charging process $e_{fade,cha}$ caused only by charging can be found in the last column of Table 3.5.

For the cycle ageing tests no. 1 to 4 between 0 % and 80 % SOC with different charge rates, the charging-related energy fade for each charge rate $e_{fade,cha}$(0-80 %, r_{cha}) is related to the energy fade value of charging with 1 P $e_{fade,cha}$(0-80 %, 1P). Thus, a charge rate dependent ageing factor is calculated:

$$f_{age}(r_{cha}) = \frac{e_{fade,cha}(\text{0-80 \%}, r_{cha})}{e_{fade,cha}(\text{0-80 \%}, \text{1P})} \tag{3.10}$$

Charging with 1 P is set to an ageing factor of 100 % and a slower or faster charge rate will decrease or increase the energy fade accordingly. For different charge rates, the ageing factor is:

$$\begin{aligned} f_{age}(0.2\,\mathrm{P}) &= 3.17\,\%, \\ f_{age}(0.5\,\mathrm{P}) &= 7.93\,\%, \\ f_{age}(1.0\,\mathrm{P}) &= 100.00\,\%, \\ f_{age}(1.5\,\mathrm{P}) &= 154.84\,\%. \end{aligned}$$

The ageing factor for 1.5 P is neglected in the further course of this work. For a charge rate of 1.5 P, the overpotential is so high that the CV phase is entered before the SOC of 80 % is reached and the charge power decreases. Therefore, the actual average charge rate is lower than 1.5 P resulting in a lower energy fade value. Furthermore, the test conditions exceed the cell specifications given by the manufacturer (Samsung SDI Co., Ltd., 2008). Hence, the ageing factor for 1.5 P is not comparable to the other values and disregarded from this point onwards. Figure 3.10 contains the ageing factors for the different charge rates, derived from the cycle ageing tests no. 1 to 3. It is assumed that changing the charge rate while keeping the rest of the test conditions constant results in the same relation of energy fade as it did for tests no. 1 to 3. This means that the ageing factors are applied not only to cycling between 0 % and 80 %, but between any other SOCs and DODs. As the ageing factor for 1 P is 100 %, the energy fade values $e_{fade,cha}$ for tests no. 5 to 9 remain the same, as they were also charged with 1 P.

In order to allow any possible charge rate between 0.2 P and 1 P, the development of the three ageing factors was fitted with an exponential function as displayed in Figure 3.10. The function fitted to the ageing factors depending on the charge rate is

$$\begin{aligned} f_{age}(r_{cha}) = {} & 0.91667 \cdot \exp\left[2.9667 \cdot (r_{cha} - 1.3333)\right] \\ & + 6.65 \cdot 10^{-6} \cdot \exp\left[11.5 \cdot r_{cha}\right] \end{aligned} \tag{3.11}$$

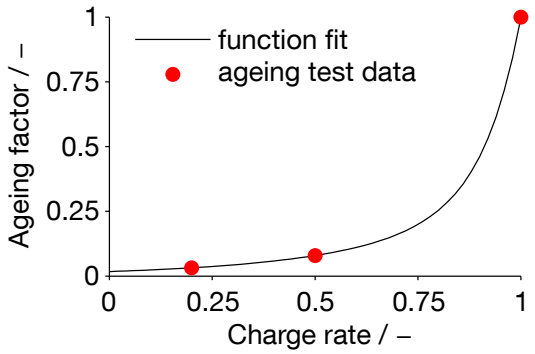

Figure 3.10 – Ageing factor for different charge rates

or, in a more general form with the coefficients replaced by the alphabetic characters g_8, ..., g_{12}

$$f_{age}(r_{cha}) = g_8 \cdot \exp\left[g_9 \cdot (r_{cha} - g_{10})\right] + g_{11} \cdot \exp\left[g_{12} \cdot r_{cha}\right]. \tag{3.12}$$

The deviation between function values and ageing test values are only 0.4 %, 0.2 %, and −0.3 % for a charge rate of 0.2 P, 0.5 P, and 1 P.

To identify the influence of SOC and DOD on the ageing behaviour, tests no. 3 and 5 to 9 are compared. For all those tests, the charge rate is the same with 1 P, but SOC and DOD vary. Hence, the energy fade during these cycle ageing tests depends on two parameters, SOC_{start} and SOC_{end}. The energy fade per charging process $e_{fade,cha}$ (see Table 3.5, last column, tests no. 3, 5-9) is plotted versus SOC_{start} and SOC_{end} in a three-dimensional graph. Figure 3.11 depicts the measured energy fade values from Table 3.5 as well as a two-dimensional function fitted to the measured data. The function

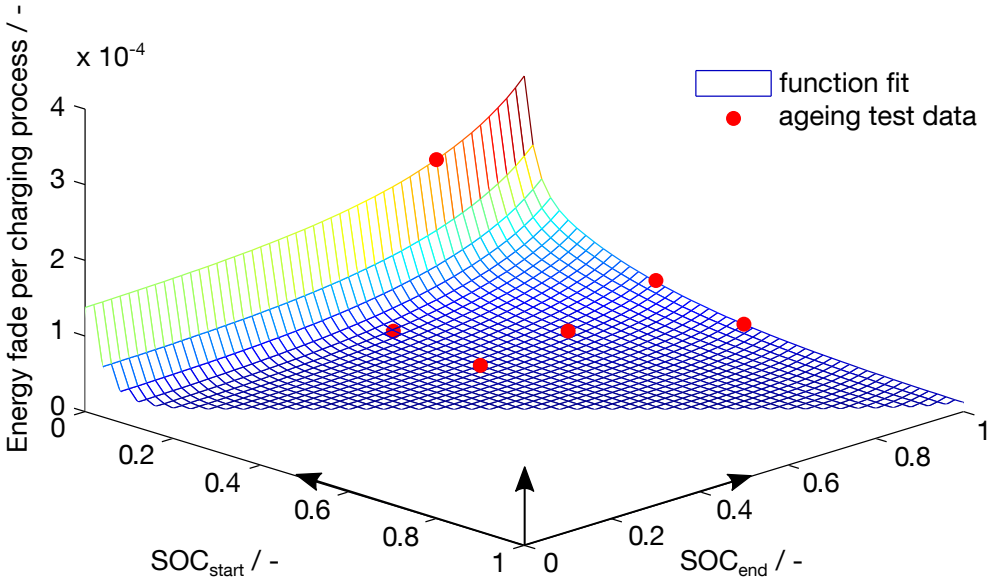

Figure 3.11 – SOC-dependent energy fade for a charge rate of 1 P

fitted to the energy fade values depending on SOC_{start} and SOC_{end} at a charge rate of 1 P

has the form:

$$\begin{aligned} e_{fade,cha}(SOC_{start}, SOC_{end}, 1P) = \\ g_1 \cdot \exp\left[g_2 \cdot (SOC_{end} - SOC_{start} - g_3)\right] \\ + g_4 \cdot \exp\left[g_5 \cdot (1 - SOC_{start})\right] \\ + g_6 \cdot \exp\left[g_7 \cdot (SOC_{end} - 1)\right] \end{aligned} \tag{3.13}$$

The first summand of the function equation describes the dependence on the ΔSOC, which is the difference between SOC_{end} and SOC_{start}. The function value rises with increasing ΔSOC along the diagonal of the SOC_{start}-SOC_{end}-plane, displayed as the middle arrow in Figure 3.11. The second summand reflects how a higher SOC_{start} reduces the energy fade during charging. The third summand mirrors the increase of energy fade along with an increasing SOC_{end}. Both directions are shown as arrows in Figure 3.11. All three effects have been already described in the interpretation of Figures 3.2 and 3.4 in Section 3.2.1.

g_1	$2.5935 \cdot 10^{-6}$
g_2	3.8703
g_3	$4.1246 \cdot 10^{-3}$
g_4	$2.0801 \cdot 10^{-23}$
g_5	43.3173
g_6	$9.4748 \cdot 10^{-6}$
g_7	17.3891
g_8	0.91667
g_9	2.9667
g_{10}	1.3333
g_{11}	$6.65 \cdot 10^{-6}$
g_{12}	11.5

Table 3.6 – Coefficients of the energy fade function and the ageing factor function

The exact values for the coefficients $g_1, \ldots, g_7$ are determined by means of a MATLAB script and are listed in Table 3.6. The script assigns a range of values to each of the seven coefficients. For all possible combinations of coefficients $g_1, \ldots, g_7$, function values for the energy fade are calculated with equation (3.13) and compared to the data points from the ageing test data. The combination of coefficients resulting in the energy fade values closest to the measured data is used as starting points for the next iteration. A narrower value range is chosen and placed around the new starting points and the next iteration is conducted. This procedure continues until an acceptable level of deviation between function values and measured data points is reached. Applying the coefficient values obtained by this method reveal the following equation:

$$\begin{aligned} e_{fade,cha}(SOC_{start}, SOC_{end}, 1P) = \\ 2.5935 \cdot 10^{-6} \cdot \exp\left[3.8703 \cdot \left(SOC_{end} - SOC_{start} - 4.1246 \cdot 10^{-3}\right)\right] \\ + 2.0801 \cdot 10^{-23} \cdot \exp\left[43.3173 \cdot (1 - SOC_{start})\right] \\ + 9.4748 \cdot 10^{-6} \cdot \exp\left[17.3891 \cdot (SOC_{end} - 1)\right] \end{aligned} \tag{3.14}$$

The deviation between function values and measured values is negligibly small for four out of the six data points. For the data points at 30 % to 100 % and 10 % to 60 % SOC, deviations of –3.4 % and 5.4 % occur. These inaccuracies are accepted, as also errors of measurement can arise during the ageing tests.

To fit a more precise function to the ageing data, it would be desirable to have more data points as input for the function fit. This means further ageing tests would have to be conducted at different test conditions. For example, cycle ageing tests at 1 P/1 C between SOCs 10 % and 80 %, 10 % and 100 %, or 0 % and 100 % make sense to expand the coverage of probable BEV charging patterns.

In order to obtain energy fade values for any combination of SOC, ΔSOC, and charge rate, equations (3.12) and (3.13) are multiplied. Visually expressed, this is the product of Figures 3.10 and 3.11. Equation (3.13) describes the energy fade during one charging process $e_{fade,cha}$ at a charge rate of 1 P. The ageing factor f_{age}, defined in equation (3.12), gives the ratio how much a different charge rate reduces or increases the energy fade. Hence, the product of these two functions results in a function applicable to an arbitrary combination of SOC_{start}, SOC_{end}, and r_{cha}:

$$\begin{aligned} &e_{fade,cha}(SOC_{start}, SOC_{end}, r_{cha}) = \\ &e_{fade,cha}(SOC_{start}, SOC_{end}, 1P) \cdot f_{age}(r_{cha}) = \\ &\quad \{g_1 \cdot \exp\left[g_2 \cdot (SOC_{end} - SOC_{start} - g_3)\right] \\ &\quad + g_4 \cdot \exp\left[g_5 \cdot (1 - SOC_{start})\right] + g_6 \cdot \exp\left[g_7 \cdot (SOC_{end} - 1)\right]\} \\ &\quad \cdot \{g_8 \cdot \exp\left[g_9 \cdot (r_{cha} - g_{10})\right] + g_{11} \cdot \exp\left[g_{12} \cdot r_{cha}\right]\} \end{aligned} \tag{3.15}$$

3.4 General Assumptions of the Battery Ageing Model

The determination of the SOC for the battery ageing tests was conducted via ampere-hour counting – i. e. integrating the (dis)charge current – and then related to the nominal capacity, which is a widespread method (Jossen & Weydanz, 2006, p. 209). For the charging optimisation and the therewith interconnected battery ageing model – described in the following chapter –, the SOC is calculated based on the energy that is charged or discharged. This is due to the fact that the optimisation objectives are based on energy and power calculations for the charging strategies for BEVs and a compatibility between the battery ageing model and the charging optimisation model is necessary. However, the energy-based SOC can differ from the SOC calculated by means of ampere-hour counting. This originates from the cell voltage, which increases along with the SOC of the battery. Hence, for a DOD of 10 % between 90 % and 100 %, more energy is (dis)charged than between 10 % and 20 %, while the amount of Ah is the same. Despite this deviation in the SOC calculation through Wh instead of Ah, the SOC is calculated based on energy flows in the further course of this work in order to achieve compatibility between the battery ageing and the charging optimisation model. A possible effect is that the energy fade values derived from the ageing tests might occur at slightly different energy-based SOCs. This can be avoided when already during the design of the battery ageing tests, the SOCs for the test conditions are defined by means of the energy (dis)charged instead of integrating the (dis)charge current. However, this might be a rather complicated task,

since the amount of cycled Ah needs to be permanently down-regulated during the course of the ageing tests. The internal resistance increases along with the age of a battery and a higher overpotential occurs. Thus, the (dis)charge current needs to be adapted to lower levels in order to keep the energy cycled and therewith the energy-based SOC constant. Due to these reasons, it is refrained in this work from this procedure and the inaccuracy between Ah- and Wh-based SOC calculation is accepted.

The ageing tests described and evaluated in this chapter were conducted with a sample of cells and a battery ageing model was derived. For the further use of the cell-based battery ageing model in the context of a charging optimisation model for BEVs, it is assumed that the battery ageing in a battery pack consisting of a multitude of cells happens in the same way as in the test cells.

Chapter 4

Development of the Charging Optimisation Model

After modelling the mobility behaviour of battery electric vehicles to serve as input data and deriving a battery ageing model, the centrepiece of this work – the charging optimisation model – is developed. The battery ageing model is the basis for the battery ageing costs being part of the optimisation model.

Aim of the charging optimisation model is to minimise total charging costs. The total charging costs consist of charging electricity cost as well as battery ageing costs due to cycle and calendar ageing. The decision when and how fast to charge a BEV has an influence on the charging electricity cost due to fluctuating electricity prices. Additionally, it affects the ageing process within the BEV's battery. The charging optimisation model finds the optimal trade-off between charging during low electricity price periods and charging in a battery performance sustaining manner.

The optimisation problem consists of an objective function minimising the total charging costs subject to several constraints, which describe the relation between charging process, battery ageing behaviour, and power system. Initially, it is formulated as a mixed-integer non-linear programme (MINLP). In order to find a global optimal solution, it is then reformulated into a mixed-integer linear programme (MILP).

This chapter firstly provides an overview of the relevant theory of optimisation problems. Next, the charging optimisation model is described, starting with the methodology used to integrate the battery ageing model, followed by the elaboration, formulation, and linearisation of the optimisation problem itself. Finally, an alternative approach for more complex battery ageing data is outlined.

4.1 Fundamentals of Convex Optimisation, Linear Programmes, and Mixed-Integer Linear Programmes

The explanations and definitions of convex optimisation and its corresponding types of optimisation problems presented in this section are taken from Boyd and Vandenberghe (2004, pp. 7, 14, 67, 136, 146, 152 f.).

It is desirable to formulate a problem as a convex optimisation problem since it can be solved efficiently and a global optimum can be found. Convex optimisation problems have the form

$$\begin{array}{lll} \text{minimise} & f_0(x) & \\ \text{subject to} & f_i(x) \leq 0, & i = 1, \ldots, m \\ & a_i^T x = b_i, & i = 1, \ldots, p, \end{array} \tag{4.1}$$

where x is the decision variable and all the functions $f_0, \ldots, f_m : \mathbb{R}^n \to \mathbb{R}$ are convex. The functions are convex if $f_i(\theta x + (1-\theta)y) \leq \theta f_i(x) + (1-\theta) f_i(y)$ is satisfied for all x, y in the domain of f_i ($\operatorname{dom} f_i$) and for all θ with $0 \leq \theta \leq 1$. Visually, this means that the line between any two points $(x, f(x))$ and $(y, f(y))$ on the function f lies above the graph of the function, as shown in Figure 4.1.

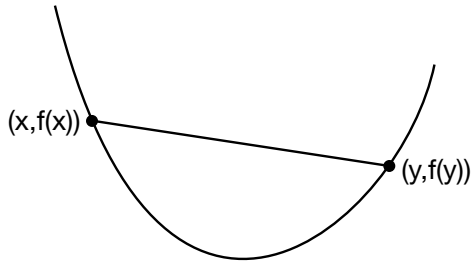

Figure 4.1 – Visualisation of a convex function

A linear programme (LP), which is also a convex optimisation problem, is defined as

$$\begin{array}{ll} \text{minimise} & c^T x + d \\ \text{subject to} & Gx \leq h \\ & Ax = b, \end{array} \tag{4.2}$$

where x is the decision variable, $G \in \mathbb{R}^{m \times n}$ and $A \in \mathbb{R}^{p \times n}$. $\mathbb{R}^{m \times n}$ represents the set of $m \times n$ matrices of real numbers and $\mathbb{R}^{p \times n}$ accordingly $p \times n$ matrices. An LP consists of a linear objective function and linear inequality as well as equality constraints.

Next, a quadratic programme (QP) is specified as

$$\begin{array}{ll} \text{minimise} & \frac{1}{2} x^T P x + q^T x + r \\ \text{subject to} & Gx \leq h \\ & Ax = b, \end{array} \tag{4.3}$$

where again x is the decision variable, $P \in \mathbb{S}_+^n$, $G \in \mathbb{R}^{m \times n}$, and $A \in \mathbb{R}^{p \times n}$. $\mathbb{S}_+^n$ indicates the set of symmetric positive semidefinite $n \times n$ matrices. The difference between a QP and LP is obviously the quadratic objective function. The objective is a convex

quadratic function since the matrix P is positive semidefinite. If the matrix P is not positive semidefinite, it is not a convex optimisation problem anymore.

LPs are special cases of QPs, with $P = 0$ in equation (4.3).

If, additionally to the objective, also the inequality constraints are convex quadratic functions, we have a quadratically constrained quadratic programme (QCQP):

$$\begin{aligned} \text{minimise} \quad & \frac{1}{2}x^T P_0 x + q_0^T x + r_0 \\ \text{subject to} \quad & \frac{1}{2}x^T P_i x + q_i^T x + r_i \leq 0, \qquad i = 1, \ldots, m \\ & Ax = b, \end{aligned} \tag{4.4}$$

where $P_i \in \mathbb{S}_+^n$ for $i = 0, 1, \ldots, m$.

QPs are special cases of QCQPs, with $P_i = 0$ for $i = 1, \ldots, m$ in equation (4.4).

From convex optimisation problem to QCQP to QP to LP, each is a special form of the previous one and the definitions on the form of objective function and constraints become more restrictive. Generally, it can be said, the more specific the form of the optimisation problem becomes, the more efficiently it can be solved.

Aside from convex optimisation problems, the definition of a mixed-integer linear programme (MILP) with binary variables shall be mentioned here, because the final charging optimisation problem is formulated as such a problem:

$$\begin{aligned} \text{minimise} \quad & c^T x + d^T y \\ \text{subject to} \quad & Gx + Hy \leq h \\ & Ax + By = b \\ & x \in \mathbb{R}^n \\ & y \in \{0, 1\}^q, \end{aligned} \tag{4.5}$$

where x is a vector of n continuous decision variables and y a vector of q binary decision variables, $G \in \mathbb{R}^{m \times n}$, $H \in \mathbb{R}^{m \times q}$, $A \in \mathbb{R}^{p \times n}$, and $B \in \mathbb{R}^{p \times q}$ (Floudas, 1995, p. 96), (Conejo et al., 2006, p. 244 f.).

If the objective function and / or the equality as well as inequality constraints are non-linear, it is a mixed-integer non-linear programme (MINLP) with binary variables:

$$\begin{aligned} \text{minimise} \quad & f(x, y) \\ \text{subject to} \quad & g_i(x, y) \leq 0, \qquad i = 1, \ldots, m \\ & h_i(x, y) = 0, \qquad i = 1, \ldots, p \\ & x \in \mathbb{R}^n \\ & y \in \{0, 1\}^q, \end{aligned} \tag{4.6}$$

with x being a vector of n continuous decision variables and y a vector of q binary decision variables (Floudas, 1995, p. 111).

4.2 Integration of Battery Ageing Functions into the Optimisation Model

Regarding the formulation of the charging optimisation problem, the modelling of battery ageing plays a significant role. The battery ageing functions for calendar and cycle ageing elaborated in Chapter 3 become part of the charging optimisation model. They are included as constraints and the approach used will be explained in this section.

4.2.1 Three-Dimensional Cycle Ageing Function

Reflecting the comments on convex optimisation in the previous section, it becomes clear how important it is to formulate a problem by means of convex functions.

The function describing the energy fade caused by the charging process of a battery can be found in equation (3.15) in Section 3.3.2 and is displayed again here:

$$\begin{aligned} & e_{fade,cha}(SOC_{start}, SOC_{end}, r_{cha}) = \\ & e_{fade,cha}(SOC_{start}, SOC_{end}, 1P) \cdot f_{age}(r_{cha}) = \\ & \quad \{g_1 \cdot \exp\left[g_2 \cdot (SOC_{end} - SOC_{start} - g_3)\right] \\ & \quad + g_4 \cdot \exp\left[g_5 \cdot (1 - SOC_{start})\right] + g_6 \cdot \exp\left[g_7 \cdot (SOC_{end} - 1)\right]\} \\ & \quad \cdot \{g_8 \cdot \exp\left[g_9 \cdot (r_{cha} - g_{10})\right] + g_{11} \cdot \exp\left[g_{12} \cdot r_{cha}\right]\} \end{aligned} \tag{3.15}$$

It consists of two factors, which are multiplied. The first part or factor of the function – i. e. $e_{fade,cha}(SOC_{start}, SOC_{end}, 1P)$ in equation (3.13) – is the sum of three positive exponential functions. Positive exponential functions are convex, as is the sum of such functions. Figure 3.11 also shows clearly the convexity of the function in equation (3.13) and (3.14), respectively. The second part or factor is the sum of two positive exponential functions – i. e. f_{age} in equation (3.12) – and hence convex, which can also be seen in Figure 3.10. The function combining the two factors as a product – i. e. $e_{fade,cha}(SOC_{start}, SOC_{end}, r_{cha})$ in equation (3.15) – is presented in its expanded form here:

$$\begin{aligned} & e_{fade,cha}(SOC_{start}, SOC_{end}, r_{cha}) = \\ & \quad g_1 \cdot g_8 \cdot \exp\left[g_2 \cdot (SOC_{end} - SOC_{start} - g_3) + g_9 \cdot (r_{cha} - g_{10})\right] \\ & \quad + g_1 \cdot g_{11} \cdot \exp\left[g_2 \cdot (SOC_{end} - SOC_{start} - g_3) + g_{12} \cdot r_{cha}\right] \\ & \quad + g_4 \cdot g_8 \cdot \exp\left[g_5 \cdot (1 - SOC_{start}) + g_9 \cdot (r_{cha} - g_{10})\right] \\ & \quad + g_4 \cdot g_{11} \cdot \exp\left[g_5 \cdot (1 - SOC_{start}) + g_{12} \cdot r_{cha}\right] \\ & \quad + g_6 \cdot g_8 \cdot \exp\left[g_7 \cdot (SOC_{end} - 1) + g_9 \cdot (r_{cha} - g_{10})\right] \\ & \quad + g_6 \cdot g_{11} \cdot \exp\left[g_7 \cdot (SOC_{end} - 1) + g_{12} \cdot r_{cha}\right] \end{aligned} \tag{4.7}$$

with the coefficients $g_1, \ldots, g_{12}$ listed in Table 3.6.

As can be seen, the expanded form of the function is again the sum of positive exponential functions and therefore still a convex function. The convex form of the cycle ageing function plays a significant role in formulating the charging optimisation problem as well as in solving it later on. The three-dimensional function $e_{fade,cha}(SOC_{start}, SOC_{end}, r_{cha})$ in equation (3.15) or (4.7) cannot be plotted, but can be imagined as the product of the

function graphs in Figures 3.10 and 3.11, with the input values SOC_{start}, SOC_{end}, and charge rate r_{cha} on the first three axes and the corresponding energy fade values on the fourth axis.

4.2.2 Derivation of Piecewise Linear Approximation of a Three-Dimensional Function

The cycle ageing function in equation (4.7) is a convex exponential function (and neither a convex quadratic nor a linear function). Hence, the charging optimisation problem cannot be a QP, QCQP or LP, but a general convex optimisation problem. However, to make use of efficient solving algorithms, the cycle ageing constraint containing the convex exponential function is replaced by linear constraints, as required for an LP.

For this purpose, the approach of piecewise linear approximation is used. A non-linear function is approximated with a set of straight lines – either tangents or secants – as drafted in Figure 4.2 as an example with tangents.

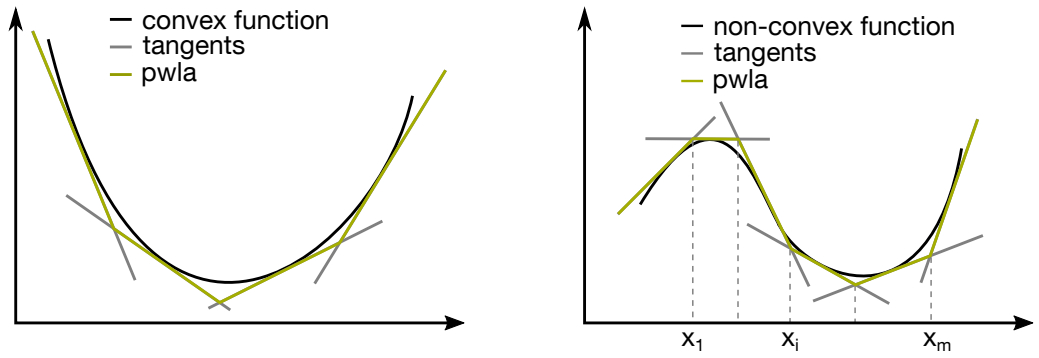

(a) Convex function (b) Non-convex function

Figure 4.2 – Piecewise linear approximation (pwla) of a convex and non-convex function with tangents

Given the function is convex, the approximated function can be expressed as a piecewise linear function (Boyd & Vandenberghe, 2004, p. 150)

$$f(x) = \max_{i=1,\dots,m} (a_i^T x + b_i). \tag{4.8}$$

If this piecewise linear function is to be minimised, it can be transformed to the following LP

$$\begin{aligned} &\text{minimise} && t \\ &\text{subject to} && \max_{i=1,\dots,m} (a_i^T x + b_i) \leq t, \end{aligned} \tag{4.9}$$

where t is to be minimised under the constraint that it must lie above or on the piecewise linear function (Boyd & Vandenberghe, 2004, p. 150). So, in the optimum, t will lie on the piecewise linear function. Since the original function as well as the piecewise linear

function are convex, the previous LP can be further transformed into the following LP

$$\begin{aligned} &\text{minimise} && t \\ &\text{subject to} && a_i^T x + b_i \leq t, \qquad i = 1, \ldots, m, \end{aligned} \tag{4.10}$$

where the inequality constraint is separated into several inequalities (Boyd & Vandenberghe, 2004, p. 151).

The importance of the convexity of the function which is to be approximated becomes clear in Figure 4.2. For a convex function, all tangents together form a lower border of the function (see Figure 4.2a in green). Hence, for convex functions, the functional equation of each straight line $1, \ldots, m$ approximating the original function can simply be added as an inequality constraint to an LP, as it is described in equation (4.10). On the other hand, for non-convex functions (see Figure 4.2b), each of the tangents' functional equations $\hat{f}_1, \ldots, \hat{f}_m$ needs to be defined only for the domain where it is approximating the original function: $\operatorname{dom} \hat{f}_i = \{x | x_i \leq x \leq x_{i+1}\}$. Thus, it is guaranteed that the tangents build a lower border for t which matches the original function and can serve as constraint for a minimisation problem similar to the one in equation (4.10). The difference is that each of the constraints $a_i^T x + b_i \leq t$ is defined only for its specific domain $\operatorname{dom} \hat{f}_i$. If the tangents' functional equations are not defined for the corresponding domain only, some lines would in some segments lie above the tangent relevant in this segment. In this case, the lower border serving as constraint for the minimisation problem would not match the original function anymore. The different domains of definition of the inequality constraints require a lot of additional equations and also computation time. Therefore, it is desirable to have a convex function as a base for the optimisation problem, as it is the case for the cycle ageing function elaborated in Section 4.2.1. An approach for non-convex battery ageing functions is described in Section 4.5.

The approach of piecewise linear approximation to integrate battery ageing behaviour into a charging optimisation model for BEVs was already used in previous work (Trippe et al., 2014). The relation between charge rate and battery ageing was modelled and approximated by a set of straight lines. Analogous to piecewise linear approximation of one-dimensional functions with lines – as it was applied by Trippe et al. (2014) – or of two-dimensional functions with planes, three-dimensional hyperplanes in the four-dimensional space are used to approximate the cycle ageing function in equation (3.15) or (4.7). As tangents or tangent planes are used for the piecewise linear approximation of one- or two-dimensional functions, tangent hyperplanes are generated for the three-dimensional cycle ageing function. For that purpose, at several points of the cycle ageing function, the derivatives with respect to each of the three input axes – SOC_{start}, SOC_{end}, and r_{cha} – are calculated and used to build the equations of the tangent hyperplanes.

$$\begin{aligned} \frac{\partial e_{fade,cha}}{\partial SOC_{start}} = &- g_2 \cdot g_1 \cdot g_8 \cdot \exp\left[g_2 \cdot (SOC_{end} - SOC_{start} - g_3) + g_9 \cdot (r_{cha} - g_{10})\right] \\ &- g_2 \cdot g_1 \cdot g_{11} \cdot \exp\left[g_2 \cdot (SOC_{end} - SOC_{start} - g_3) + g_{12} \cdot r_{cha}\right] \\ &- g_5 \cdot g_4 \cdot g_8 \cdot \exp\left[g_5 \cdot (1 - SOC_{start}) + g_9 \cdot (r_{cha} - g_{10})\right] \\ &- g_5 \cdot g_4 \cdot g_{11} \cdot \exp\left[g_5 \cdot (1 - SOC_{start}) + g_{12} \cdot r_{cha}\right] \end{aligned} \tag{4.11}$$

$$\begin{aligned}\frac{\partial e_{fade,cha}}{\partial SOC_{end}} = \quad & g_2 \cdot g_1 \cdot g_8 \cdot \exp\left[g_2 \cdot (SOC_{end} - SOC_{start} - g_3) + g_9 \cdot (r_{cha} - g_{10})\right] \\ & + g_2 \cdot g_1 \cdot g_{11} \cdot \exp\left[g_2 \cdot (SOC_{end} - SOC_{start} - g_3) + g_{12} \cdot r_{cha}\right] \\ & + g_7 \cdot g_6 \cdot g_8 \cdot \exp\left[g_7 \cdot (SOC_{end} - 1) + g_9 \cdot (r_{cha} - g_{10})\right] \\ & + g_7 \cdot g_6 \cdot g_{11} \cdot \exp\left[g_7 \cdot (SOC_{end} - 1) + g_{12} \cdot r_{cha}\right]\end{aligned} \tag{4.12}$$

$$\begin{aligned}\frac{\partial e_{fade,cha}}{\partial r_{cha}} = \quad & g_9 \cdot g_1 \cdot g_8 \cdot \exp\left[g_2 \cdot (SOC_{end} - SOC_{start} - g_3) + g_9 \cdot (r_{cha} - g_{10})\right] \\ & + g_{12} \cdot g_1 \cdot g_{11} \cdot \exp\left[g_2 \cdot (SOC_{end} - SOC_{start} - g_3) + g_{12} \cdot r_{cha}\right] \\ & + g_9 \cdot g_4 \cdot g_8 \cdot \exp\left[g_5 \cdot (1 - SOC_{start}) + g_9 \cdot (r_{cha} - g_{10})\right] \\ & + g_{12} \cdot g_4 \cdot g_{11} \cdot \exp\left[g_5 \cdot (1 - SOC_{start}) + g_{12} \cdot r_{cha}\right] \\ & + g_9 \cdot g_6 \cdot g_8 \cdot \exp\left[g_7 \cdot (SOC_{end} - 1) + g_9 \cdot (r_{cha} - g_{10})\right] \\ & + g_{12} \cdot g_6 \cdot g_{11} \cdot \exp\left[g_7 \cdot (SOC_{end} - 1) + g_{12} \cdot r_{cha}\right]\end{aligned} \tag{4.13}$$

Equations (4.11) to (4.13) contain the partial derivatives with respect to SOC_{start}, SOC_{end}, and r_{cha}, respectively. For several specific points of the cycle ageing function (4.7), which are marked with indices x and defined through specific quadruples $(SOC^x_{start}, SOC^x_{end}, r^x_{cha}, e^x_{fade,cha})$, the partial derivatives as well as the function value are calculated. The results yield the coefficients of the tangent hyperplane equation in that specific point $(SOC^x_{start}, SOC^x_{end}, r^x_{cha}, e^x_{fade,cha})$. The resultant equations of the tangent hyperplanes in different points x appear as follows:

$$\begin{aligned}e^{tanHyp}_{fade,cha}(x) = \quad & \text{coefficient}^{\,x}_{SOC_{start}} \cdot SOC_{start} \\ & + \text{coefficient}^{\,x}_{SOC_{end}} \cdot SOC_{end} \\ & + \text{coefficient}^{\,x}_{r_{cha}} \cdot r_{cha} \\ & + \text{constant}\end{aligned} \tag{4.14}$$

$$\begin{aligned}= \quad & \frac{\partial e_{fade,cha}}{\partial SOC_{start}}(SOC^x_{start}, SOC^x_{end}, r^x_{cha}) \cdot SOC_{start} \\ & + \frac{\partial e_{fade,cha}}{\partial SOC_{end}}(SOC^x_{start}, SOC^x_{end}, r^x_{cha}) \cdot SOC_{end} \\ & + \frac{\partial e_{fade,cha}}{\partial r_{cha}}(SOC^x_{start}, SOC^x_{end}, r^x_{cha}) \cdot r_{cha} \\ & + e_{fade,cha}(SOC^x_{start}, SOC^x_{end}, r^x_{cha}) \\ & - \frac{\partial e_{fade,cha}}{\partial SOC_{start}}(SOC^x_{start}, SOC^x_{end}, r^x_{cha}) \cdot SOC^x_{start} \\ & - \frac{\partial e_{fade,cha}}{\partial SOC_{end}}(SOC^x_{start}, SOC^x_{end}, r^x_{cha}) \cdot SOC^x_{end} \\ & - \frac{\partial e_{fade,cha}}{\partial r_{cha}}(SOC^x_{start}, SOC^x_{end}, r^x_{cha}) \cdot r^x_{cha}\end{aligned} \tag{4.15}$$

Figures 4.3 and 4.4 indicate at which points x the tangent hyperplanes are created. The 36 black crosses in Figure 4.3 show the SOC_{start}-SOC_{end}-combinations, each further combined with a charge rate r_{cha} of 0.2, 0.5, 0.75 and 1 P (see black crosses in Figure 4.4), resulting in a total of 144 locations for the tangent hyperplanes.

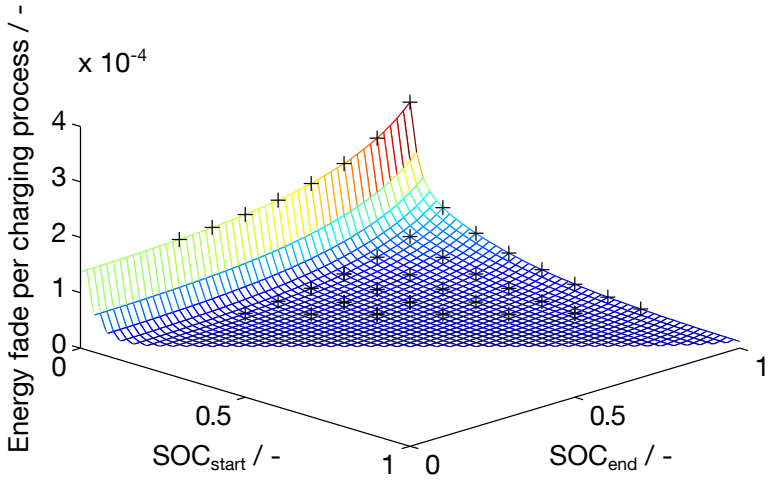

Figure 4.3 – Locations of tangent hyperplanes for different SOC_{start}-SOC_{end}-combinations

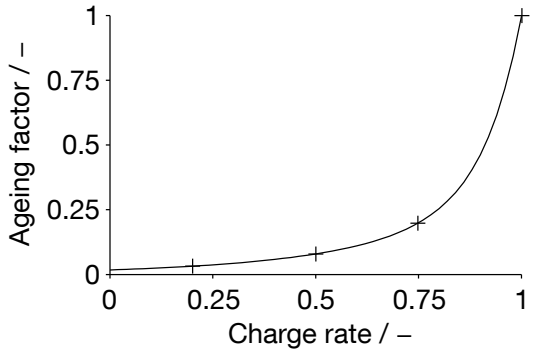

Figure 4.4 – Locations of tangent hyperplanes for different charge rates

As the cycle ageing function consists of a sum of exponential functions without any offset, the function value representing the energy fade never reaches 0. However, at the diagonal where SOC_{start} equals SOC_{end} ($\Delta SOC = 0\,\%$, diagonal is indicated in Figure 4.5), the battery is not charged at all and the energy fade should be equal to 0. In order to reflect this fact, the course of the energy fade is assumed to be linear between the diagonal where $SOC_{end} = SOC_{start} + 30\,\%$ ($\Delta SOC = 30\,\%$, diagonal is highlighted in Figure 4.5) and the $\Delta SOC = 0\,\%$ diagonal. It means that no tangent hyperplanes at or close to the $\Delta SOC = 0\,\%$ diagonal are created. The closest tangent hyperplanes are located at the $\Delta SOC = 30\,\%$ diagonal. Those tangent hyperplanes are steeper than the cycle ageing function in the region of the $\Delta SOC = 0\,\%$ diagonal. Thereby, the tangent hyperplanes at $\Delta SOC = 30\,\%$ reach energy fade values of 0 or slightly below at the $\Delta SOC = 0\,\%$ diagonal. By means of a constraint defined in Section 4.3, it is guaranteed

that the energy fade cannot be negative. Thus, within the charging optimisation model, the energy fade for charging with a ΔSOC of 0 % or very close to it obtains a value of 0.

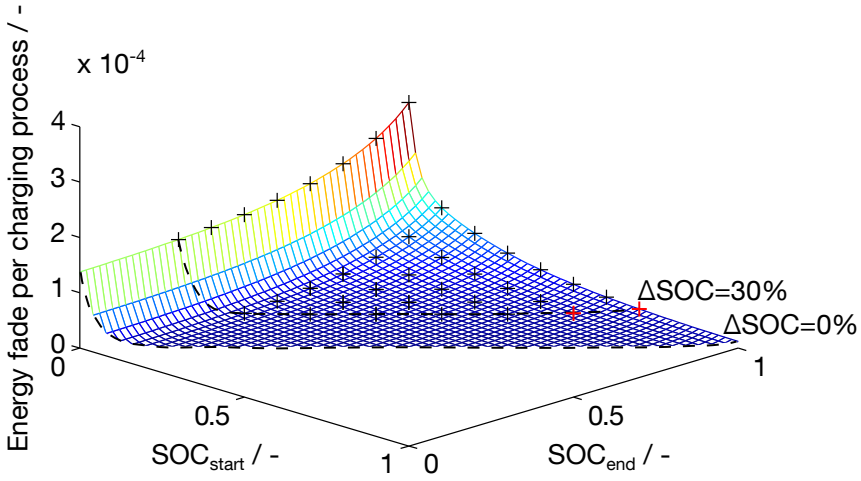

Figure 4.5 – Locations of tangent hyperplanes with ΔSOC = 30 % and ΔSOC = 0 % diagonals

However, in some points of the ΔSOC = 0 % diagonal, the energy fade is still positive. This is only a problem for a charge rate r_{cha} of 0.2 P. This can be explained by a short lookahead on the functionality of the charging optimisation model. When solving the optimisation problem described in Section 4.3, it might be the case that the solver sets SOC_{start} and SOC_{end} to equal values. Then, it is not charged and the charge power P_{fix} is irrelevant to the solution. Therefore, the solver sets P_{fix} to its lower bound in order to minimise the charge rate r_{cha} and thereby also the cycle ageing cost C_{ageCyc} (cf. equations (4.27) and (4.39)). Consequentially, only the points with positive energy fade values on the ΔSOC = 0 % diagonal at a charge rate r_{cha} of 0.2 P have to be examined.

As can be guessed from Figure 4.5, for $SOC_{start} = SOC_{end} \leq 10\,\%$, the energy fade approximated by the tangent hyperplanes shows values higher than 0. However, as the formulation of the optimisation problem does not allow an SOC below 10 % (see Sections 4.3 and 5.1.4), this is irrelevant. Also, for $SOC_{start} = SOC_{end} \geq 89\,\%$, the energy fade values are slightly positive instead of 0, caused by the tangent hyperplanes in the points $(SOC^x_{start}, SOC^x_{end}, r^x_{cha}) = (70\,\%, 100\,\%, 0.2\,\mathrm{P})$ and $(60\,\%, 90\,\%, 0.2\,\mathrm{P})$; i. e. the outer two points of the area where tangent hyperplanes were created, marked as red crosses in Figure 4.5. As a solution to this problem, those two tangent hyperplanes were removed from the set of 144 hyperplanes approximating the original cycle ageing function in equation (4.7). As a result, the approximation consisting of the remaining 142 tangent hyperplanes produces positive energy fade values at the ΔSOC = 0 % diagonal only for $SOC_{start} = SOC_{end} \geq 99\,\%$. Those values are – even though positive – negligibly small (order of magnitude 10^{-8} compared to energy fade during the charging process in order of magnitude 10^{-6} or more, see last column of Table 3.4) and therefore are accepted as a sufficiently close approximation of the cycle ageing function at the ΔSOC = 0 % diagonal. Furthermore, it is unlikely that a BEV's battery SOC is 99 % after a trip and therefore

this point will be reached very seldom within the charging optimisation.

Summing up, the convex, three-dimensional cycle ageing function is piecewise-linearly approximated by 142 tangent hyperplanes. The 142 hyperplane equations and their coefficients according to equation (4.14) can be found in Appendix B.

It is pointed out that the constant voltage (CV) phase at the end of a charging process is not regarded in the optimisation model. This simplification is used as the charging optimisation seldom charges the BEVs to 100 % SOC and most of the times with a rather low charge rate (cf. results of base scenario in Section 5.2.1, especially Figures 5.4 and 5.7). So, a CV phase would occur rarely. A further advantage is a reduction in complexity of the charging optimisation model.

4.2.3 Calendar Ageing Function

Equation (3.5) describes the energy fade per hour due to calendar ageing, displayed in Figure 3.7b. As shown before, calendar ageing decreases with lower SOC. Within the charging optimisation, a minimum battery SOC is included as a buffer to avoid break-downs of BEVs due to depleted batteries. This buffer is formulated as a constraint in equation (4.22) of the optimisation problem. Because the BEV's SOC is not allowed to drop below 10 % (cf. Section 5.1.4), a minimum calendar ageing effect occurs, which cannot be further diminished by the charging optimisation. This energy fade value can be calculated by entering 10 % SOC into equation (3.5), resulting in an energy fade per hour due to calendar ageing of $1.956 \cdot 10^{-6}$/h.

Since the minimum energy fade cannot be influenced by the charging optimisation, it should be excluded from the calculation of the total charging costs within the optimisation. Thereby, only factors influenceable by the charging optimisation are included and compared to each other. The calendar ageing function in equation (3.5) is reduced by an offset of $1.956 \cdot 10^{-6}$/h, which equals the minimum energy fade per hour at 10 % SOC. As a result, the adapted calendar ageing function to be used in the charging optimisation produces the energy fade per hour due to calendar ageing influenceable by the charging optimisation:

$$e_{fade,cal,offset} = \begin{cases} 2.16 \cdot 10^{-6}\,\mathrm{h}^{-1} \cdot SOC - 2.16 \cdot 10^{-7}\,\mathrm{h}^{-1}, & \text{for } SOC \leq 80\,\% \\ 1.08 \cdot 10^{-5}\,\mathrm{h}^{-1} \cdot SOC - 7.086 \cdot 10^{-6}\,\mathrm{h}^{-1}, & \text{for } SOC > 80\,\% \end{cases} \quad (4.16)$$

4.3 Formulation of the Optimisation Problem

In this section, the formulation of the initial optimisation problem will be elaborated. The objective function minimises the total charging costs and is subject to constraints related to the vehicle, battery, and power system. The battery ageing functions in Sections 4.2.1 and 4.2.3 will be integrated as battery ageing constraints. The initial optimisation problem will be formulated as a mixed-integer non-linear programme (MINLP). The two non-linear components of the optimisation problem (the term describing the charge power and the cycle ageing function) will be linearised and thereby the transformation into a mixed-integer linear programme (MILP) is achieved. The resulting linearised problem will be detailed in the subsequent section.

Sets	
a	Index of agent/BEV
i	Index of parking respectively preceding trip
k	Index of tangent hyperplane equations of cycle ageing
l	Index of linear equations of calendar ageing
t	Index of time step

Parameters	
η_{batt}	Efficiency of battery
η_{chaSt}	Efficiency of charging station
$b_{park}(a,i,t)$	Binary parameter, whether vehicle is parking or not during time step t
$C_{batt}(a)$	Battery cost for each BEV
$C_{specBatt}$	Specific battery cost
$E_{cons}(a,i)$	Energy consumption of a BEV during a trip
$E_{nom}(a)$	Nominal energy content of battery for each BEV
f_{EOL}	Share of nominal energy content at which a battery reaches end of life
f_{resale}	Resale factor for a battery at end of life
$f_{traLoss}$	Transmission loss factor
$g_1, \ldots, g_{12}$	Coefficients of function on energy fade during charging process
h_1, h_2, h_3, h_4	Coefficients of tangent hyperplane equations of cycle ageing
h_5, h_6	Coefficients of linear equations of calendar ageing
$P_{max}(a)$	Maximum charge power for each BEV
$P_{maxSys}(t)$	Power limit by power system for each time step
P_{min}	Minimum charge power
$pr_{el}(t)$	Electricity price for each time step
$r_{cha,max}$	Maximum charge rate
SOC_0	State of charge at the beginning of simulation time
SOC_{min}	Minimum state of charge of a battery
SOC_{max}	Maximum state of charge of a battery
Δt	Duration of one time step

Decision variables	
$b_{cha}(a,i,t)$	Binary variable, whether vehicle is charging or not during time step t
$C_{ageCal}(a,i,t)$	Calendar ageing cost during one time step
$C_{ageCyc}(a,i)$	Cycle ageing cost of the charging process during one parking event
C_{ageTot}	Total ageing cost of all charging processes during simulation horizon
C_{elTot}	Electricity cost of all charging processes during simulation horizon
C_{tot}	Total cost of all charging processes during simulation horizon
$P(a,i,t)$	Charge power for each parking event and time step
$P_{fix}(a,i)$	Charge power for each parking event
$r_{cha}(a,i)$	Charge rate for each parking event
$SOC_{start}(a,i)$	State of charge at the beginning of parking
$SOC_{end}(a,i)$	State of charge at the end of parking

Table 4.1 – Overview of sets, parameters, and decision variables

Formulating the optimisation problem corresponding to the charging optimisation model requires a number of sets, parameters, and decision variables. Sets are synonymic to indices, parameters are fixed values which are not changed during the optimisation, and decision variables are assigned their optimal values by the optimisation programme. Table 4.1 lists all sets, parameters, and decision variables used in the charging optimisation problem and provides a short explanation for each.

The parameters, which serve as fixed input data for the charging optimisation model, comprise (i) conditions of the power system and charging stations, (ii) characteristics of the BEV batteries and their ageing behaviour, as well as (iii) information on the driving and parking schedule of the BEVs including the energy consumption during their trips. It is assumed to have a perfect forecast of the travelling schedules. This forecast provides a frame of constraints for the charging optimisation, within which the charging processes can be optimally allocated. The notion of a perfect forecast of travelling schedules might seem unrealistic at first, but considering the field of machine learning, travelling patterns might be captured by learning algorithms deployed in BEVs in the future.

The optimisation programme assigns values to different decision variables whereas the most important decision variables are the ones defining the charge power. The other decision variables concerning SOC, charge rate, battery ageing cost and electricity cost can be derived from those decision variables.

4.3.1 Initial Optimisation Problem – Formulated as Mixed-Integer Non-Linear Programme

The initial formulation of the mathematical model is presented in equations (4.17) to (4.34) as follows.

$$\begin{aligned}\text{Minimise} \quad & C_{tot} \\ & = C_{elTot} && + C_{ageTot} \\ & = \sum_{a,i,t} \left[\frac{P_{fix}(a,i) \cdot b_{cha}(a,i,t)}{\eta_{chaSt}} \cdot \Delta t \cdot f_{traLoss} \cdot pr_{el}(t) \right] && + \sum_{a,i} C_{ageCyc}(a,i) \\ & && + \sum_{a,i,t} C_{ageCal}(a,i,t)\end{aligned} \tag{4.17}$$

subject to

$$SOC_{start}(a, i_{first}) = SOC_0 - \frac{E_{cons}(a, i_{first})/\eta_{batt}}{E_{nom}(a)} \qquad \forall\, a, i_{first} \tag{4.18}$$

$$SOC_{start}(a,i) = SOC_{end}(a,i-1) - \frac{E_{cons}(a,i)/\eta_{batt}}{E_{nom}(a)} \qquad \forall\, a,i \tag{4.19}$$

$$SOC_{end}(a,i) = SOC_{start}(a,i) + \frac{\sum_t P_{fix}(a,i) \cdot b_{cha}(a,i,t) \cdot \Delta t}{E_{nom}(a)} \qquad \forall\, a,i \tag{4.20}$$

$$SOC_{end}(a, i_{last}) \geq SOC_0 \qquad \forall\, a, i_{last} \tag{4.21}$$

$$SOC_{start}(a,i) \geq SOC_{min} \qquad \forall\, a,i \tag{4.22}$$

$$SOC_{end}(a,i) \leq SOC_{max} \qquad \forall\, a,i \tag{4.23}$$

$$P_{min} \leq P_{fix}(a,i) \leq P_{max}(a) \qquad \forall\, a,i \qquad (4.24)$$

$$b_{cha}(a,i,t) = 0, \quad \text{if} \quad b_{park}(a,i,t) = 0 \qquad \forall\, a,i,t \qquad (4.25)$$

$$b_{cha}(a,i,t) \in \{0,1\} \qquad \forall\, a,i,t \qquad (4.26)$$

$$r_{cha}(a,i) = P_{fix}(a,i)/E_{nom}(a) \qquad \forall\, a,i \qquad (4.27)$$

$$\begin{aligned} C_{ageCyc}(a,i) \geq \\ &\{g_1 \cdot g_8 \cdot \exp\left[g_2 \cdot (SOC_{end}(a,i) - SOC_{start}(a,i) - g_3) + g_9 \cdot (r_{cha}(a,i) - g_{10})\right] \\ &+ g_1 \cdot g_{11} \cdot \exp\left[g_2 \cdot (SOC_{end}(a,i) - SOC_{start}(a,i) - g_3) + g_{12} \cdot r_{cha}(a,i)\right] \\ &+ g_4 \cdot g_8 \cdot \exp\left[g_5 \cdot (1 - SOC_{start}(a,i)) + g_9 \cdot (r_{cha}(a,i) - g_{10})\right] \\ &+ g_4 \cdot g_{11} \cdot \exp\left[g_5 \cdot (1 - SOC_{start}(a,i)) + g_{12} \cdot r_{cha}(a,i)\right] \\ &+ g_6 \cdot g_8 \cdot \exp\left[g_7 \cdot (SOC_{end}(a,i) - 1) + g_9 \cdot (r_{cha}(a,i) - g_{10})\right] \\ &+ g_6 \cdot g_{11} \cdot \exp\left[g_7 \cdot (SOC_{end}(a,i) - 1) + g_{12} \cdot r_{cha}(a,i)\right]\} \\ &\cdot \frac{1}{1 - f_{EOL}} \cdot C_{batt}(a) \qquad \forall\, a,i \end{aligned} \qquad (4.28)$$

$$C_{ageCyc}(a,i) \geq 0 \qquad \forall\, a,i \qquad (4.29)$$

$$\begin{aligned} C_{ageCal}(a,i,t) \geq \\ &\left\{ \left[SOC_{start}(a,i) + \sum_{\bar{t}=1}^{t} \left(P_{fix}(a,i) \cdot b_{cha}(a,i,\bar{t}) \right) \cdot \Delta t / E_{nom}(a) \right] \cdot h_5(l) + h_6(l) \right\} \\ &\cdot \Delta t \cdot \frac{1}{1 - f_{EOL}} \cdot C_{batt}(a) \qquad \forall\, a,i,t,l \text{ where } b_{park}(a,i,t) = 1 \end{aligned} \qquad (4.30)$$

$$C_{ageCal}(a,i,t) \geq 0 \qquad \forall\, a,i,t \qquad (4.31)$$

Equation (4.17) displays the objective function of the charging optimisation problem, which minimises the total charging costs consisting of electricity cost and battery ageing cost. Constraints (4.18) to (4.23) calculate the SOCs at the beginning and end of the different trips and charging processes. The charge power is determined by constraints (4.24) to (4.27), while constraints (4.28) to (4.31) define the battery ageing costs.

The parameters $P_{max}(a)$ and $C_{batt}(a)$ are defined by the following two equations and are calculated before the execution of the optimisation.

$$P_{max}(a) = E_{nom}(a) \cdot r_{cha,\,max} \qquad (4.32)$$

$$C_{batt}(a) = E_{nom}(a) \cdot C_{specBatt} \cdot [1 - f_{resale}] \qquad (4.33)$$

An additional constraint can be added for scenarios where a power system restriction is taken into account.

$$\sum_{a,i} \left(P_{fix}(a,i) \cdot b_{cha}(a,i,t) \right) \leq P_{maxSys}(t) \qquad \forall\, t \qquad (4.34)$$

Detailed explanations of each constraint will be given in Section 4.4. But first, the linearisation of two non-linear components within the initial optimisation problem is elaborated.

4.3.2 Linearisation of the Charge Power Term

The non-linearity of the optimisation problem presented above originates from the non-linear term $P_{fix}(a,i) \cdot b_{cha}(a,i,t)$, which occurs in the objective function (4.17), the SOC_{end} constraint (4.20), the calendar ageing constraint (4.30), as well as the power system constraint (4.34).

For each parking event, it is decided by the charging optimisation whether the BEV is charged at all, at which charge rate and during which time steps of the parking duration it is charged. The charge rate and with it the charge power level is constant within one parking event. This means the charge power cannot be altered during one charging process, it can merely be turned on or off. This is in consistency with the cycle ageing tests elaborated in Section 3.2.1. For each of the ageing tests listed in Table 3.1, the SOC_{start}, SOC_{end}, and the charge rate r_{cha} is fixed for the duration of the ageing test. Hence, cycle ageing tests with altering charge rates were not examined and no conclusions can be drawn on ageing effects of such charging profiles.

Focussing again on the mathematical formulation of the charging optimisation model, the term $P_{fix}(a,i) \cdot b_{cha}(a,i,t)$ defines the actual charge power for each parking i of each BEV a for every single time step t. Thereby, the continuous decision variable P_{fix} indicates the charge power level, which is fixed for each parking event, and b_{cha} is a binary decision variable displaying whether it is charged or not during the specific time step.

Hence, the charge power is the product of one continuous and one binary variable. It is namely a quadratic term, however it cannot be formulated by means of a positive semidefinite matrix as in a QP defined in equation (4.3). Consequently, the functions containing the term are non-linear, non-convex functions and thus the optimisation problem is of the form MINLP. The non-linear term $P_{fix}(a,i) \cdot b_{cha}(a,i,t)$ is now linearised by applying the reformulation-linearisation technique originally presented by Sherali and Adams (1994). Therefore, a new variable is introduced to replace the product of a continuous and binary variable: $P(a,i,t) = P_{fix}(a,i) \cdot b_{cha}(a,i,t)$. Additionally, the following set of linear constraints is created:

$$P(a,i,t) \leq P_{max}(a) \cdot b_{cha}(a,i,t) \qquad \forall\, a,i,t \qquad (4.35)$$

$$P(a,i,t) \geq P_{min} \cdot b_{cha}(a,i,t) \qquad \forall\, a,i,t \qquad (4.36)$$

$$P(a,i,t) \leq P_{fix}(a,i) - P_{min} \cdot [1 - b_{cha}(a,i,t)] \qquad \forall\, a,i,t \qquad (4.37)$$

$$P(a,i,t) \geq P_{fix}(a,i) - P_{max}(a) \cdot [1 - b_{cha}(a,i,t)] \qquad \forall\, a,i,t \qquad (4.38)$$

If the binary $b_{cha}(a,i,t) = 0$ (meaning it is not charged), constraints (4.35) and (4.36) force $P(a,i,t) \leq 0$ and $P(a,i,t) \geq 0$ and thus $P(a,i,t) = 0$. For $b_{cha}(a,i,t) = 1$, the two constraints limit P by P_{min} and P_{max}, which are the bounds for the charge power level P_{fix} (see constraint (4.24)). So, when a BEV is charged during a time step, the charge power lies within the limits for the charge power levels. Constraints (4.37) and (4.38) force $P(a,i,t) = P_{fix}(a,i)$ if it is charged ($b_{cha}(a,i,t) = 1$). For $b_{cha}(a,i,t) = 0$, those two

constraints appear as $0 \leq P_{fix}(a,i) - P_{min}$ and $0 \geq P_{fix}(a,i) - P_{max}$ which is always true due to constraint (4.24). All of these four constraints (4.35) to (4.38) are linear, as they consist of products of one variable and one parameter or of sums thereof. They ensure that for $b_{cha}(a,i,t) = 0 \Rightarrow P(a,i,t) = 0$, and for $b_{cha}(a,i,t) = 1 \Rightarrow P(a,i,t) = P_{fix}(a,i)$. Hence, this set of linear constraints is equivalent to the non-linear term $P_{fix}(a,i) \cdot b_{cha}(a,i,t)$.

4.3.3 Linearisation of the Cycle Ageing Function

A second source of the non-linearity of the initial optimisation problem is the convex, exponential cycle ageing function (4.7) (Section 4.2.1), which is included in constraint (4.28).

The exponential function is piecewise-linearly approximated by 142 tangent hyperplanes as elaborated in Section 4.2.2. Therefore, equation (4.14) (Section 4.2.2), which defines the tangent hyperplanes, replaces the cycle ageing function in the cycle ageing cost constraint (4.28). The tangent hyperplane equation can be found as the numerator of the fraction in the reformulated version of constraint (4.28):

$$C_{ageCyc}(a,i) \geq \frac{h_1(k) \cdot SOC_{start}(a,i) + h_2(k) \cdot SOC_{end}(a,i) + h_3(k) \cdot r_{cha}(a,i) + h_4(k)}{1 - f_{EOL}} \cdot C_{batt}(a) \qquad \forall\, a,i,k \tag{4.39}$$

The linearised constraint occurs 142 times, one constraint for each tangent hyperplane.

4.4 Linearised Optimisation Problem – Reformulated as Mixed-Integer Linear Programme

In order to convert the charging optimisation problem from an MINLP into an MILP, the reformulation-linearisation technique elaborated in Section 4.3.2 is implemented in the mathematical formulation of the optimisation problem. The non-linear term $P_{fix}(a,i) \cdot b_{cha}(a,i,t)$ is replaced by $P(a,i,t)$ in the objective function (4.17) as well as in the constraints (4.20), (4.30), and (4.34). Furthermore, the linear constraints (4.35) to (4.38) are added to the mathematical formulation of the optimisation problem.

Concomitant, constraint (4.25) is reformulated as

$$P(a,i,t) = 0, \quad \text{if} \quad b_{park}(a,i,t) = 0 \qquad \forall\, a,i,t. \tag{4.40}$$

Additionally, the exponential cycle ageing constraint (4.28) of the initial optimisation problem is replaced by its linearised version in equation (4.39) in Section 4.3.3.

Adopting the aforementioned amendments to the mathematical formulation of the optimisation problem, we obtain a linear objective function as well as linear constraints. All decision variables are continuous variables with exception of the binary variable b_{cha}. This meets the definition of a MILP defined in equation (4.5). The reformulated, linearised optimisation problem appears as follows. Extensive discussions of all equations will be given in the subsequent sections.

Minimise C_{tot}

$$= C_{elTot} + C_{ageTot}$$

$$= \sum_{a,i,t} \left[\frac{P(a,i,t)}{\eta_{chaSt}} \cdot \Delta t \cdot f_{traLoss} \cdot pr_{el}(t) \right] + \sum_{a,i} C_{ageCyc}(a,i) + \sum_{a,i,t} C_{ageCal}(a,i,t) \quad (4.41)$$

subject to

$$SOC_{start}(a, i_{first}) = SOC_0 - \frac{E_{cons}(a, i_{first})/\eta_{batt}}{E_{nom}(a)} \quad \forall\, a, i_{first} \quad (4.18)$$

$$SOC_{start}(a,i) = SOC_{end}(a, i-1) - \frac{E_{cons}(a,i)/\eta_{batt}}{E_{nom}(a)} \quad \forall\, a, i \quad (4.19)$$

$$SOC_{end}(a,i) = SOC_{start}(a,i) + \frac{\sum_t P(a,i,t) \cdot \Delta t}{E_{nom}(a)} \quad \forall\, a, i \quad (4.42)$$

$$SOC_{end}(a, i_{last}) \geq SOC_0 \quad \forall\, a, i_{last} \quad (4.21)$$

$$SOC_{start}(a,i) \geq SOC_{min} \quad \forall\, a, i \quad (4.22)$$

$$SOC_{end}(a,i) \leq SOC_{max} \quad \forall\, a, i \quad (4.23)$$

$$P_{min} \leq P_{fix}(a,i) \leq P_{max}(a) \quad \forall\, a, i \quad (4.24)$$

if $b_{park}(a,i,t) = 0$

$$P(a,i,t) = 0 \quad \forall\, a, i, t \quad (4.40)$$

if $b_{park}(a,i,t) = 1$

$$P(a,i,t) \leq P_{max}(a) \cdot b_{cha}(a,i,t) \quad \forall\, a, i, t \quad (4.35)$$

$$P(a,i,t) \geq P_{min} \cdot b_{cha}(a,i,t) \quad \forall\, a, i, t \quad (4.36)$$

$$P(a,i,t) \leq P_{fix}(a,i) - P_{min} \cdot [1 - b_{cha}(a,i,t)] \quad \forall\, a, i, t \quad (4.37)$$

$$P(a,i,t) \geq P_{fix}(a,i) - P_{max}(a) \cdot [1 - b_{cha}(a,i,t)] \quad \forall\, a, i, t \quad (4.38)$$

$$b_{cha}(a,i,t) \in \{0,1\} \quad \forall\, a, i, t \quad (4.26)$$

$$r_{cha}(a,i) = P_{fix}(a,i)/E_{nom}(a) \quad \forall\, a, i \quad (4.27)$$

$$C_{ageCyc}(a,i) \geq \frac{h_1(k) \cdot SOC_{start}(a,i) + h_2(k) \cdot SOC_{end}(a,i) + h_3(k) \cdot r_{cha}(a,i) + h_4(k)}{1 - f_{EOL}} \cdot C_{batt}(a) \quad \forall\, a, i, k \quad (4.39)$$

$$C_{ageCyc}(a,i) \geq 0 \quad \forall\, a, i \quad (4.29)$$

(4.43)

$$C_{ageCal}(a,i,t) \geq \left\{ \left[SOC_{start}(a,i) + \sum_{\bar{t}=1}^{t} P(a,i,\bar{t}) \cdot \Delta t / E_{nom}(a) \right] \cdot h_5(l) + h_6(l) \right\} \cdot \Delta t \cdot \frac{1}{1 - f_{EOL}} \cdot C_{batt}(a) \qquad \forall\, a,i,t,l \text{ where } b_{park}(a,i,t) = 1 \tag{4.44}$$

$$C_{ageCal}(a,i,t) \geq 0 \qquad \forall\, a,i,t \tag{4.31}$$

with the definition of two parameters $P_{max}(a)$ and $C_{batt}(a)$, which can be calculated beforehand

$$P_{max}(a) = E_{nom}(a) \cdot r_{cha,max} \tag{4.32}$$

$$C_{batt}(a) = E_{nom}(a) \cdot C_{specBatt} \cdot [1 - f_{resale}]\,. \tag{4.33}$$

An additional constraint can be added for scenarios where a power system restriction is taken into account:

$$\sum_{a,i} P(a,i,t) \leq P_{maxSys}(t) \qquad \forall\, t \tag{4.45}$$

4.4.1 Objective Function

The objective of the charging optimisation model is to minimise the total charging costs C_{tot} and is described by the objective function (4.41). The total charging costs of all BEVs during the entire simulation horizon consist of the total charging electricity cost C_{elTot} and the total ageing cost C_{ageTot}.

C_{elTot} can be calculated by multiplication of the electricity price with the electricity consumed for charging the BEVs. The charge power $P(a,i,t)$ for agent a's BEV during parking i in time step t multiplied by the duration of one time step Δt results in the energy charged during one time step into one vehicle. Dividing by η_{chaSt} adds the losses within the charging station and the factor $f_{traLoss}$ includes transmission losses occurring within the power grid, leading to the amount of energy extracted from the power grid to charge one vehicle during one time step. Multiplying this with the electricity price $pr_{el}(t)$ of the respective time step yields the electricity cost for one vehicle during one time step. The total charging electricity costs C_{elTot} are obtained by adding up the previous over all vehicles, parking events, and time steps.

The total ageing costs C_{ageTot} are further divided into cycle and calendar ageing cost, C_{ageCyc} and C_{ageCal}. The cycle ageing cost contains one value for each parking i of each agent/vehicle a and are therefore summed over all a and i. The calendar ageing cost is calculated for each vehicle a, parking i, and time step t and are accordingly added up to produce the the total ageing costs C_{ageTot}. The cycle and calendar ageing costs are further defined by the battery ageing constraints (4.39), (4.29), (4.44), and (4.31), which will be detailed later on.

The objective function is the sum of decision variables P, C_{ageCyc}, and C_{ageCal}, some of them multiplied by parameters. Hence, it is a linear objective function as defined in equation (4.2).

4.4.2 SOC Constraints

Constraints (4.18) to (4.23) define the calculation of each battery's SOC as well as SOC limits and therewith associated the decision variables SOC_{start} and SOC_{end}.

Constraint (4.18) describes the calculation of SOC_{start} of the initial parking i_{first} for each BEV. It results from SOC_0 at the beginning of the simulation period minus the ΔSOC that is consumed during the first trip. The subtrahend ΔSOC is the energy consumed during the trip E_{cons}, divided by the battery efficiency η_{batt}, divided by the nominal energy content of the battery E_{nom}. $E_{cons}(a, i_{first})/\eta_{batt}$ includes the losses while cycling a battery and represents the energy amount the battery must provide in order to fulfil the trip. Division by the nominal energy content E_{nom} yields the ΔSOC referring to the energy consumed during the trip. Constraint (4.19) defines the SOC_{start} of all following parking events i and is calculated analogously, with the minuend replaced by the SOC_{end} at the end of the previous parking $i-1$.

The SOC at the end of a parking event SOC_{end} is set by constraint (4.42) as the sum of the SOC at the beginning of the parking SOC_{start} and the ΔSOC that is charged during the respective parking event. In this case, ΔSOC is the sum of the decision variable for charge power P over the duration of the parking event, multiplied by the time step duration Δt, divided by the nominal energy content E_{nom}. Constraint (4.21) ensures that for each BEV, the SOC_{end} of the last parking event of the simulation period i_{last} is greater than or equal to the SOC at the beginning of the simulation period. Otherwise, the charging optimisation would not schedule any charging processes towards the end of the simulation period and deplete the batteries as much as possible to reduce charging cost.

Constraints (4.22) and (4.23) limit SOC_{start} and SOC_{end} to a lower and upper bound to guarantee a realisable battery operation.

4.4.3 Charge Power Constraints

The constraints regarding the charge power are given in equations (4.24), (4.40), (4.35) to (4.38), (4.26), and (4.27).

The decision variable P_{fix} specifies the charge power level which is fixed for each parking event. As can be seen in constraint (4.24), it is limited by P_{min}, which is a general value for all BEVs and P_{max}, which is determined for each BEV individually according to equation (4.32).

The actual charge power for each parking i of each BEV a for every single time step t is defined through $P(a, i, t)$. As long as the BEV is driving and not parking anywhere, it cannot be charged and the charge power $P(a, i, t)$ has to equal 0 for these time steps t, which is ensured by constraint (4.40).

For a parking BEV, the charge power is defined through constraints (4.35) to (4.38). Those were introduced as additional constraints in line with the reformulation-linearisation technique as elaborated in Section 4.3.2. In order to linearise the mathematical optimisation problem, the quadratic term $P_{fix}(a, i) \cdot b_{cha}(a, i, t)$ was replaced by $P(a, i, t)$ and the aforementioned constraints were added.

b_{cha} is defined as a binary variable in constraint (4.26).

Constraint (4.27) defines the charge rate r_{cha} analogously to the definition in equation (3.2) in Section 3.2.1. The charge rate is necessary for the further determination of the battery ageing costs explained next.

4.4.4 Battery Ageing Constraints

The cycle and calendar ageing costs C_{ageCyc} and C_{ageCal} are variables that are minimised in the objective function. Constraints (4.39) and (4.44) represent the battery ageing functions elaborated in Section 4.2. The constraints serve as lower bound for the decision variables C_{ageCyc} and C_{ageCal}. As the solver tries to minimise them as far as possible, they will obtain values lying on the lower bounds implemented by the constraints (4.39) and (4.44). Hence, the values of the decision variables correspond to battery ageing costs derived from the battery ageing functions in Section 4.2.

Regarding cycle ageing, constraint (4.39) contains equation (4.14) (Section 4.2.2), which defines the tangent hyperplanes approximating the cycle ageing function in equation (4.7) (Section 4.2.1). The linearisation of this constraint was explained earlier in Section 4.3.3. The cycle ageing cost constraint occurs with $k = 142$ different coefficient sets, one set for each tangent hyperplane as explained in Section 4.2.2. The exact values for the coefficients h_1, h_2, h_3, and h_4 are listed in Appendix B. The numerator of the constraints, equalling the hyperplane equation (4.14), represents the dimensionless energy fade during a specific charging process defined through SOC_{start}, SOC_{end}, and r_{cha}. The energy fade is divided by $1 - f_{EOL}$. f_{EOL} indicates the share of the nominal energy content of a battery when it reaches its end of life. Hence, $1 - f_{EOL}$ represents the share of the nominal energy content which is fading due to ageing of the battery during its lifetime. The fraction of energy fade during a charging process and total energy fade during its lifetime produces the share of the battery's value lost during a specific charging process. A monetisation of this loss in value is reached by multiplication with the battery cost C_{batt}, resulting in the cycle ageing cost C_{ageCyc}.

The calendar ageing cost C_{ageCal} is calculated for each time step t in constraint (4.44). Similar to constraint (4.39), constraint (4.44) includes an ageing function, too. In this case, it is the calendar ageing function in equation (4.16) (Section 4.2.3), which can be found within the outer squared brackets in constraint (4.44). It describes the energy fade per hour due to calendar ageing which can be influenced by the charging optimisation. The coefficients h_5 and h_6 have two value sets for $l = 1$ and 2 according to equation (4.16). The energy fade due to calendar ageing depends on the current SOC, which is determined by the term $SOC_{start}(a, i) + \sum_{\bar{t}=1}^{t} P(a, i, \bar{t}) \cdot \Delta t / E_{nom}(a)$ within the inner square brackets in constraint (4.44). The current SOC for each time step t is the SOC_{start} at the beginning of the current parking event plus the ΔSOC charged up to the present, which is the added-up charge power P times time step duration Δt divided by the nominal energy content E_{nom}. The therewith calculated energy fade per hour within the outer square brackets is multiplied with time step duration Δt to receive the actual energy fade within the current time step. Analogously to the cycle ageing cost C_{ageCyc} in constraint (4.39), the dimensionless energy fade is divided by the factor $1 - f_{EOL}$ and multiplied with the battery cost C_{batt} in order to obtain the calendar ageing cost C_{ageCal}.

Constraints (4.29) and (4.31) define C_{ageCyc} and C_{ageCal} as positive variables, implying that no negative battery ageing costs exist.

4.4.5 Parameter Definitions and Further Constraints

Equation (4.32) defines the parameter P_{max}. In accordance with the conducted cycle ageing tests (see Section 3.2.1), a maximum charge rate $r_{cha,max}$ of 1.5 P was chosen for the charging optimisation. So, the charge power for each BEV is capped at a charge rate of 1.5 P and the maximum charge power P_{max} is calculated according to equation (3.2) in Section 3.2.1.

The parameter C_{batt} is determined in equation (4.33). The battery cost C_{batt} for the renewal of a battery pack at the end of its lifetime consists of the price for a new pack minus the resale value of the depleted pack. This is reflected by the factor $1 - f_{resale}$ with f_{resale} being the percentage of the original price realised at resale. The battery price is calculated by the specific battery cost per kWh $C_{specBatt}$ times the nominal energy content E_{nom} of the battery pack.

An additional constraint to the described charging optimisation problem is given in equation (4.45). The original optimisation problem minimises the total charging costs for a sample of BEVs under consideration of fluctuating electricity prices as well as battery ageing behaviour. When an analysis of a considerably larger sample of BEVs is desired, the charging optimisation model should also take into account possible effects on the power system. Therefore, constraint (4.45) is provided which puts a limitation of the total charge power of all BEVs at each time step into place. The constraint ensures that the total charge power does not exceed a power limit on system level P_{maxSys}, which is a certain load allowed for BEV charging on top of the total electricity load in Singapore. The purpose is to avoid a further increase of load peaks and rather use load valleys for BEV charging. The derivation of P_{maxSys} is detailed in Section **??**.

The specific values of all parameters listed in Table 4.1, which are used when solving the optimisation problem, can be found in Section 5.1.

4.5 Alternative Solution for Non-Convex Battery Ageing Data

As battery ageing behaviour is very complex and appears to be non-linear, a case might occur (e. g. for other cell types or chemistries), in which the battery ageing function has no convex form anymore.

As already outlined in Section 4.2.2, there is an option of piecewise linear approximation for non-convex functions. Figure 4.2b offers a schematic diagram of a non-convex function and its piecewise linear approximation. Each tangent approximating the function is defined for its specific domain dom $\hat{f}_i$ only. Another option to piecewise-linearly approximate a function is to interpolate pairs of points lying on the curve. The interpolated lines mark secants of the curve, as pictured in Figure 4.6. In the following explanations, we focus on the piecewise linear approximation with secants using interpolation.

The approach of interpolation is elaborated for different dimensions, starting with one-dimensional interpolation of a one-dimensional function and adding a dimension each time up to three-dimensional interpolation. The approach of interpolation of a three-dimensional function is then applied to the battery ageing function of the charging optimisation model. An approach similar to the one evolved in this section was developed by Misener and Floudas (2010).

4.5.1 Interpolation of a 1-D Function

Within mathematical modelling of optimisation problems, the use of interpolation in order to piecewise-linearly approximate a function can be addressed by means of special ordered sets of type 2 (SOS2), initially proposed by Beale and Tomlin (1970). Special ordered sets of type 2 are sets of variables with at most two non-zero members, and if there are two variables which are non-zero, they must be adjacent (Beale & Forrest, 1976).

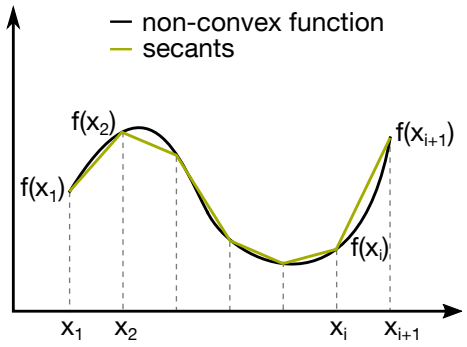

Figure 4.6 – Piecewise linear approximation of a non-convex function with secants

In an optimisation problem, the piecewise linear function drafted in Figure 4.6, which is approximating the original non-convex function, can be modelled by the following set of equations:

$$\hat{x} = \sum_i \lambda_i x_i \tag{4.46}$$

$$\hat{f}(\hat{x}) = \sum_i \lambda_i f(x_i) \tag{4.47}$$

$$\sum_i \lambda_i = 1 \tag{4.48}$$

$$\lambda_i \geq 0 \tag{4.49}$$

$$\lambda_i \quad SOS2, \tag{4.50}$$

with λ_i being SOS2 variables, meaning that at most two λ's can be non-zero and they must be adjacent. This guarantees that only two adjacent points are activated at all times. This set of equations describes any point $(\hat{x}, \hat{f}(\hat{x}))$ on the piecewise linear function and mirrors the interpolation between two adjacent points $(x_i, f(x_i))$ and $(x_{i+1}, f(x_{i+1}))$, in which λ_i and λ_{i+1} represent the weights of the two adjacent points.

4.5.2 Interpolation of a 2-D Function

Transferring this approach from one to two dimensions, each point on a two-dimensional function $f(x, y)$ can be approximated by interpolating three points on the function. For this purpose, triangulation is used: the two-dimensional domain of f (dom f) is divided into an orthogonal grid with additional diagonals, as drafted in Figure 4.7a. Each triangle is uniquely specified by choosing two adjacent vertical lines, two adjacent horizontal lines, and two adjacent diagonal lines.

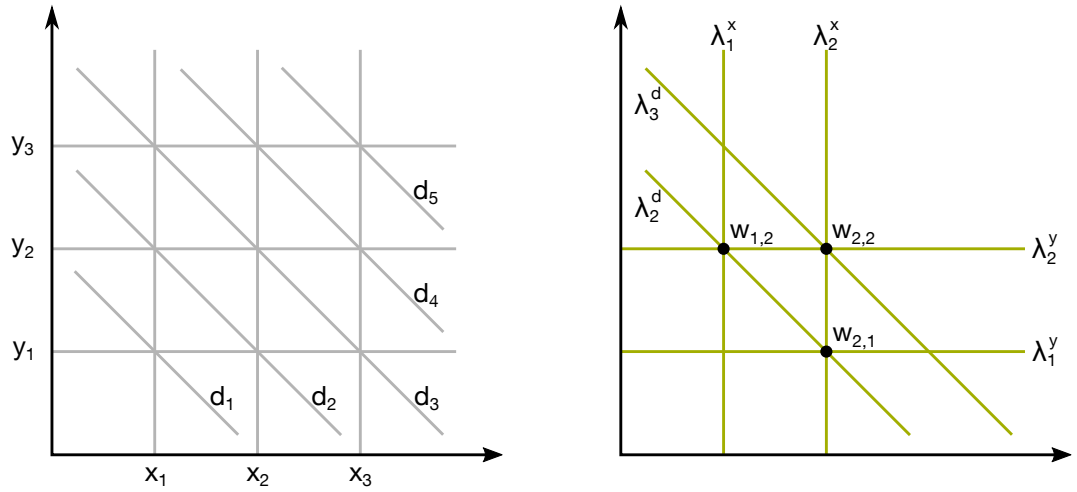

(a) Triangulation of the domain of a two-dimensional function $f(x, y)$

(b) Activation of three grid points by means of line weights λ and point weights w

Figure 4.7 – Approach for interpolation of grid points on a two-dimensional function $f(x, y)$ (topview)

Each point $(x, y) \in \text{dom}\, f$ can be expressed by a convex combination of the three grid points forming the triangle surrounding the point. The mathematical framework to determine the interpolated point $(\hat{x}, \hat{y})$ and its corresponding approximated function value $\hat{f}(\hat{x}, \hat{y})$ is given by:

$$\hat{x} = \sum_{i,j} w_{i,j} \cdot x_i \tag{4.51}$$

$$\hat{y} = \sum_{i,j} w_{i,j} \cdot y_j \tag{4.52}$$

$$\hat{f}(\hat{x}, \hat{y}) = \sum_{i,j} w_{i,j} \cdot f(x_i, y_j) \tag{4.53}$$

$$\sum_i \lambda_i^x = 1 \tag{4.54}$$

$$\sum_j \lambda_j^y = 1 \tag{4.55}$$

$$\sum_k \lambda_k^d = 1 \tag{4.56}$$

$$\lambda_i^x = \sum_j w_{i,j} \tag{4.57}$$

$$\lambda_j^y = \sum_i w_{i,j} \tag{4.58}$$

$$\lambda_k^d = \sum_{(i,j):\, i+j-1=k} w_{i,j} \tag{4.59}$$

$$w_{i,j} \geq 0 \tag{4.60}$$

$$\lambda_i^x, \lambda_j^y, \lambda_k^d \geq 0 \tag{4.61}$$

$$\lambda_i^x, \lambda_j^y, \lambda_k^d \quad SOS2. \tag{4.62}$$

Equations (4.51) to (4.53) compute the interpolated values $(\hat{x},\, \hat{y},\, \hat{f}(\hat{x},\hat{y}))$, whereas $w_{i,j}$ represent the point weights of the three grid points of the surrounding triangle. Equations (4.54) to (4.56) are the convexity constraints. λ_i^x, λ_j^y, and λ_k^d are SOS2 variables and activate exactly two adjacent lines in x-, two in y- and two in diagonal direction. Those six lines build a triangle and its vertices are used for the interpolation. Each line weight λ is split up into the corresponding point weights $w_{i,j}$ of the vertices lying on that specific line, as formulated in equations (4.57) to (4.59). Figure 4.7b illustrates this approach of two-dimensional interpolation by means of SOS2 variables.

4.5.3 Interpolation of a 3-D Function

When adding another dimension, we obtain three-dimensional interpolation of four points in a four-dimensional space. Analogously to the triangle (or 2-simplex) defined by three vertices in the previously described case of two-dimensional interpolation, now, a tetrahedron (or 3-simplex) with four vertices is used for interpolation. In Figure 4.7, the domain of the two-dimensional function was triangulated. Analogously, the domain $\operatorname{dom} f$ of a three-dimensional function $f(x,y,z)$ is partitioned into non-overlapping tetrahedrons (3-simplices), each between four grid points. This is achieved by dividing the domain with planes in x-, y-, and z-direction as well as in three different diagonal directions. Figure 4.8 illustrates the division of the three-dimensional domain into the six different directions. As a result, we obtain the partitioning of the three-dimensional domain space into non-overlapping tetrahedrons. In the centre of Figure 4.9, six of such non-overlapping tetrahedrons are displayed.

When approximating any point of the three-dimensional function $f(x,y,z)$ by means of interpolation, the corresponding tetrahedron of the domain space, within which the desired point is lying, has to be selected. This is achieved by activating pairs of adjacent grid planes in the six different directions as drafted in Figure 4.8. The intersection of the selected plane pairs produces four grid points, serving as vertices of the specific tetrahedron. Depending on which pairs of grid planes are selected, six different types of tetrahedrons appear. Those six types are sketched in Figure 4.9.

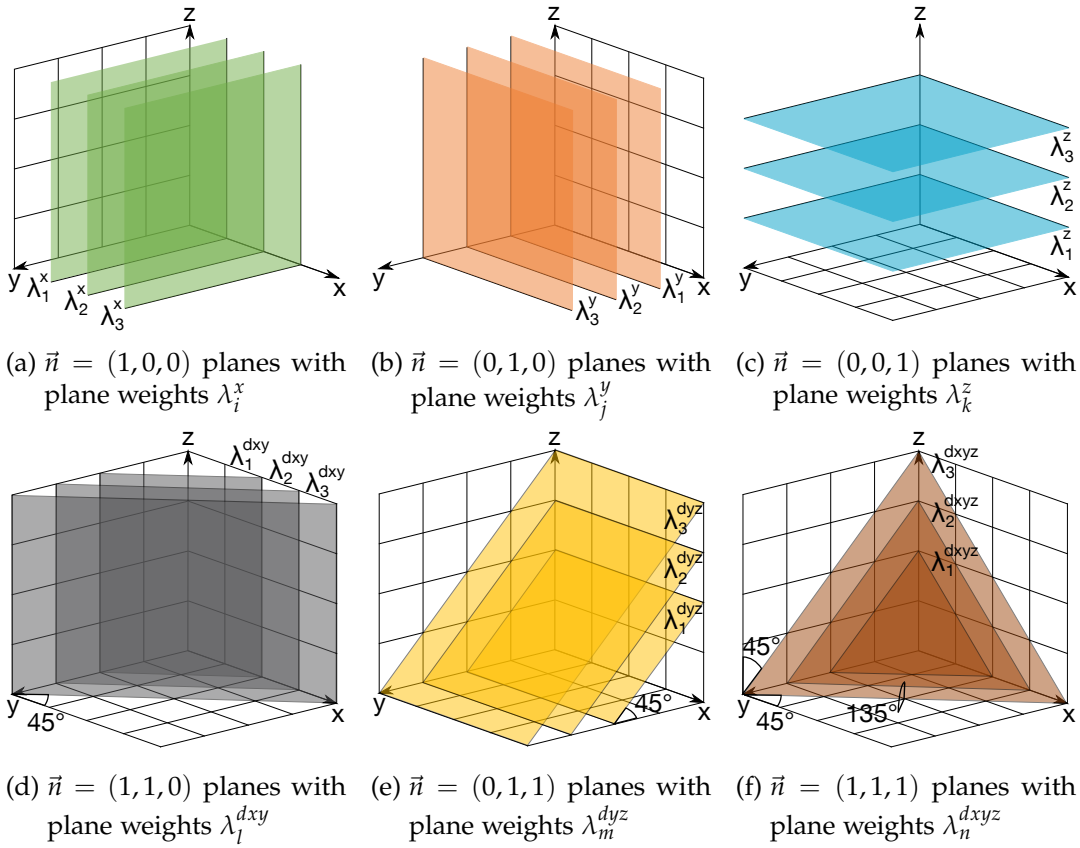

(a) $\vec{n} = (1,0,0)$ planes with plane weights λ_i^x

(b) $\vec{n} = (0,1,0)$ planes with plane weights λ_j^y

(c) $\vec{n} = (0,0,1)$ planes with plane weights λ_k^z

(d) $\vec{n} = (1,1,0)$ planes with plane weights λ_l^{dxy}

(e) $\vec{n} = (0,1,1)$ planes with plane weights λ_m^{dyz}

(f) $\vec{n} = (1,1,1)$ planes with plane weights λ_n^{dxyz}

Figure 4.8 – Partitioning of the three-dimensional domain space of a function $f(x,y,z)$ with planes into six directions; planes are defined by their normal vector $\vec{n}$

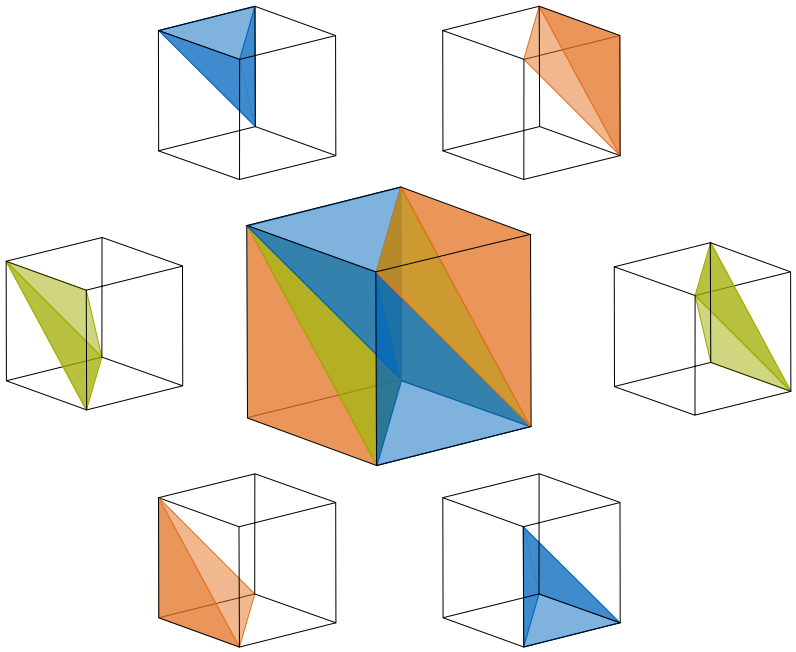

Figure 4.9 – Six different types of tetrahedrons stemming from partitioning of the domain space of a function $f(x,y,z)$ with planes into six directions

The following set of equations describes the interpolation of points on a three-dimensional function $f(x, y, z)$:

$$\hat{x} = \sum_{i,j,k} w_{i,j,k} \cdot x_i \tag{4.63}$$

$$\hat{y} = \sum_{i,j,k} w_{i,j,k} \cdot y_j \tag{4.64}$$

$$\hat{z} = \sum_{i,j,k} w_{i,j,k} \cdot z_k \tag{4.65}$$

$$\hat{f}(\hat{x}, \hat{y}, \hat{z}) = \sum_{i,j,k} w_{i,j,k} \cdot f(x_i, y_j, z_k) \tag{4.66}$$

$$\sum_i \lambda_i^x = 1 \tag{4.67}$$

$$\sum_j \lambda_j^y = 1 \tag{4.68}$$

$$\sum_k \lambda_k^z = 1 \tag{4.69}$$

$$\sum_l \lambda_l^{dxy} = 1 \tag{4.70}$$

$$\sum_m \lambda_m^{dyz} = 1 \tag{4.71}$$

$$\sum_n \lambda_n^{dxyz} = 1 \tag{4.72}$$

$$\lambda_i^x = \sum_{j,k} w_{i,j,k} \tag{4.73}$$

$$\lambda_j^y = \sum_{i,k} w_{i,j,k} \tag{4.74}$$

$$\lambda_k^z = \sum_{i,j} w_{i,j,k} \tag{4.75}$$

$$\lambda_l^{dxy} = \sum_{(i,j,k):\, i+j-1=l} w_{i,j,k} \tag{4.76}$$

$$\lambda_m^{dyz} = \sum_{(i,j,k):\, j+k-1=m} w_{i,j,k} \tag{4.77}$$

$$\lambda_n^{dxyz} = \sum_{(i,j,k):\, i+j+k-2=n} w_{i,j,k} \tag{4.78}$$

$$w_{i,j,k} \geq 0 \tag{4.79}$$

$$\lambda_i^x, \lambda_j^y, \lambda_k^z, \lambda_l^{dxy}, \lambda_m^{dyz}, \lambda_n^{dxyz} \geq 0 \tag{4.80}$$

$$\lambda_i^x, \lambda_j^y, \lambda_k^z, \lambda_l^{dxy}, \lambda_m^{dyz}, \lambda_n^{dxyz} \quad SOS2. \tag{4.81}$$

Analogously to the two-dimensional interpolation discussed in Section 4.5.2, $w_{i,j,k}$ indicate the point weights of the grid points forming the tetrahedron, which are interpolated. The plane weights for the planes in the six different directions are specified by the various λ's. As all λ's are SOS2 variables, only two adjacent planes in each direction can be

non-zero (and thus activated) at the same time. The approximated point we are looking for $(\hat{x},\, \hat{y},\, \hat{z},\, \hat{f}(\hat{x},\hat{y},\hat{z}))$ is computed in equations (4.63) to (4.66), using four points of the underlying function $(x_i,\, y_j,\, z_k,\, f(x_i,y_j,z_k))$ and their corresponding point weights $w_{i,j,k}$. Equations (4.67) to (4.72) select the six pairs of adjacent grid planes, while the upper indices of the λ's state the direction of the plane according to the nomenclature given in Figure 4.8. In equations (4.73) to (4.78), the plane weights λ are tied to the corresponding point weights $w_{i,j,k}$ on the specific plane.

4.5.4 Application of 3-D Interpolation to a Non-Convex 3-D Battery Ageing Function

The approach of three-dimensional interpolation of a three-dimensional function is now applied to the battery ageing function. Assuming the three-dimensional cycle ageing function $e_{fade,cha}(SOC_{start}, SOC_{end}, r_{cha})$ is non-convex, the function can be linearised by means of interpolation with SOS2 variables. The linearisation of the cycle ageing function is important in order to solve the charging optimisation problem.

When reviewing the optimisation problem formulated in Section 4.4, only the cycle ageing cost constraint in equation (4.39) needs to be adapted:

$$C_{ageCyc}(a,i) \geq \frac{h_1(k)\cdot SOC_{start}(a,i) + h_2(k)\cdot SOC_{end}(a,i) + h_3(k)\cdot r_{cha}(a,i) + h_4(k)}{1-f_{EOL}} \cdot C_{batt}(a) \qquad \forall\, a,i,k \tag{4.39}$$

The constraint determines the cycle ageing cost for each vehicle a's parking event i. So far, the cycle ageing cost constraint contained k tangent hyperplane equations approximating the (convex) cycle ageing function $e_{fade,cha}(SOC_{start}, SOC_{end}, r_{cha})$. The hyperplane equations yielding the approximated energy fade value can be found in the numerator of the fraction.

Dealing with a non-convex cycle ageing function requires the replacement of the tangent hyperplane equations by the interpolated energy fade value $\hat{e}_{fade,cha}(a,i)$:

$$C_{ageCyc}(a,i) \geq \frac{\hat{e}_{fade,cha}(a,i)}{1-f_{EOL}} \cdot C_{batt}(a) \qquad \forall\, a,i \tag{4.82}$$

In order to obtain the approximated energy fade value $\hat{e}_{fade,cha}(a,i)$, four points on the three-dimensional (non-convex) cycle ageing function $e_{fade,cha}(SOC_{start}, SOC_{end}, r_{cha})$ are interpolated by means of SOS2 variables. This necessitates additional constraints, which are developed analogously to the derivation of interpolation of a 3-D function in Section 4.5.3.

$$\hat{SOC}_{start}(a,i) = \sum_{\alpha,\beta,\gamma} w_{\alpha,\beta,\gamma}(a,i) \cdot SOC_{start\alpha} \qquad \forall\, a,i \qquad (4.83)$$

$$\hat{SOC}_{end}(a,i) = \sum_{\alpha,\beta,\gamma} w_{\alpha,\beta,\gamma}(a,i) \cdot SOC_{end\beta} \qquad \forall\, a,i \qquad (4.84)$$

$$\hat{r}_{cha}(a,i) = \sum_{\alpha,\beta,\gamma} w_{\alpha,\beta,\gamma}(a,i) \cdot r_{cha\gamma} \qquad \forall\, a,i \qquad (4.85)$$

$$\hat{e}_{fade,cha}(a,i) = \sum_{\alpha,\beta,\gamma} w_{\alpha,\beta,\gamma}(a,i) \cdot e_{fade,cha}(SOC_{start\alpha}, SOC_{end\beta}, r_{cha\gamma}) \qquad \forall\, a,i \qquad (4.86)$$

Constraints (4.83) to (4.86) compute the interpolated values analogously to equations (4.63) to (4.66) in Section 4.5.3. The three axes of the three-dimensional domain of the cycle ageing function are SOC_{start}, SOC_{end}, and r_{cha}. Those axes are partitioned into regular segments marked by indices α, β, and γ, forming a three-dimensional structure of grid points. $w_{\alpha,\beta,\gamma}(a,i)$ indicate the point weights of the interpolated grid points for each BEV a and parking i.

$$\sum_{\alpha} \lambda_{\alpha}^{SOC_{start}}(a,i) = 1 \qquad \forall\, a,i \qquad (4.87)$$

$$\sum_{\beta} \lambda_{\beta}^{SOC_{end}}(a,i) = 1 \qquad \forall\, a,i \qquad (4.88)$$

$$\sum_{\gamma} \lambda_{\gamma}^{r_{cha}}(a,i) = 1 \qquad \forall\, a,i \qquad (4.89)$$

$$\sum_{\delta} \lambda_{\delta}^{d110}(a,i) = 1 \qquad \forall\, a,i \qquad (4.90)$$

$$\sum_{\varepsilon} \lambda_{\varepsilon}^{d011}(a,i) = 1 \qquad \forall\, a,i \qquad (4.91)$$

$$\sum_{\zeta} \lambda_{\zeta}^{d111}(a,i) = 1 \qquad \forall\, a,i \qquad (4.92)$$

The plane weights λ for the six pairs of planes, defining the tetrahedron for interpolation as elaborated in Section 4.5.3 and displayed in Figures 4.8 and 4.9, are selected by constraints (4.87) to (4.92). The lower indices α to ζ note the position or ordinal number of the respective plane. The upper indices specify the orientation of the planes by naming the axes orthogonal to the plane or, for the diagonal planes marked with a d, the normal vector. The formulation of these constraints is analogous to equations (4.67) to (4.72).

$$\lambda_{\alpha}^{SOC_{start}}(a,i) = \sum_{\beta,\gamma} w_{\alpha,\beta,\gamma}(a,i) \qquad \forall\, a,i \tag{4.93}$$

$$\lambda_{\beta}^{SOC_{end}}(a,i) = \sum_{\alpha,\gamma} w_{\alpha,\beta,\gamma}(a,i) \qquad \forall\, a,i \tag{4.94}$$

$$\lambda_{\gamma}^{r_{cha}}(a,i) = \sum_{\alpha,\beta} w_{\alpha,\beta,\gamma}(a,i) \qquad \forall\, a,i \tag{4.95}$$

$$\lambda_{\delta}^{d110}(a,i) = \sum_{(\alpha,\beta,\gamma):\, \alpha+\beta-1=\delta} w_{\alpha,\beta,\gamma}(a,i) \qquad \forall\, a,i \tag{4.96}$$

$$\lambda_{\varepsilon}^{d011}(a,i) = \sum_{(\alpha,\beta,\gamma):\, \beta+\gamma-1=\varepsilon} w_{\alpha,\beta,\gamma}(a,i) \qquad \forall\, a,i \tag{4.97}$$

$$\lambda_{\zeta}^{d111}(a,i) = \sum_{(\alpha,\beta,\gamma):\, \alpha+\beta+\gamma-2=\zeta} w_{\alpha,\beta,\gamma}(a,i) \qquad \forall\, a,i \tag{4.98}$$

Constraints (4.93) to (4.98) distribute the plane weights λ among the corresponding point weights w on the respective plane, equivalent to equations (4.73) to (4.78).

Constraints (4.99) and (4.100) ensure that the plane and point weights are positive, meaning that the interpolated values can only lie inside the tetrahedrons. Constraint (4.101) defines all λ's as SOS2 variables so that only two adjacent planes can be selected for the interpolation.

$$w_{\alpha,\beta,\gamma}(a,i) \geq 0 \qquad \forall\, a,i \tag{4.99}$$

$$\lambda_{\alpha}^{SOC_{start}}(a,i),\ \lambda_{\beta}^{SOC_{end}}(a,i),\ \lambda_{\gamma}^{r_{cha}}(a,i),\ \lambda_{\delta}^{d110}(a,i),\ \lambda_{\varepsilon}^{d011}(a,i),\ \lambda_{\zeta}^{d111}(a,i) \geq 0 \qquad \forall\, a,i \tag{4.100}$$

$$\lambda_{\alpha}^{SOC_{start}}(a,i),\ \lambda_{\beta}^{SOC_{end}}(a,i),\ \lambda_{\gamma}^{r_{cha}}(a,i),\ \lambda_{\delta}^{d110}(a,i),\ \lambda_{\varepsilon}^{d011}(a,i),\ \lambda_{\zeta}^{d111}(a,i)\ SOS2 \qquad \forall\, a,i \tag{4.101}$$

Summing up, in case of a non-convex cycle ageing function, the cycle ageing cost constraint in equation (4.39) of the charging optimisation problem stated in Section 4.4 has to be replaced by constraints (4.82) to (4.101). Thereby, a more general form of the charging optimisation model is created, which is capable of including battery ageing functions of any form. However, because of the numerous additional SOS2 variables, which hold attributes of binary variables, the need for computational resources increases substantially. A scenario with a large amount of BEVs and a longer time horizon becomes extremely complex and costly. Hence, it is desirable – as mentioned earlier in this chapter – to obtain a convex cycle ageing function which can be approximated by regular linear constraints, leading to higher computational efficiency when solving the charging optimisation model.

Chapter 5

Applied Charging Optimisation and Results

The charging optimisation model elaborated in the preceding Chapter 4 – containing the battery ageing model developed in Chapter 3 – is applied to a sample of simulated BEVs in Singapore using the mobility model from Chapter 2. This use case of the optimisation model exemplifies the effects of intelligent charging taking into account the interrelation of power system conditions, BEV charging processes and battery ageing behaviour.

The simulation of the BEVs' driving and parking behaviour is conducted by means of the mobility model described in Chapter 2. A sample of 300 BEVs over a simulation period of four weeks is used. Given the daily travel routines of the BEVs as well as their vehicle parameters, the battery ageing model, and power system data, the charging optimisation allocates when and how the BEVs are recharged in an optimal way.

In this chapter, the input parameters and data are defined first. Next, the results of the applied charging optimisation are discussed. Therefore, various scenarios with different input parameter sets – e. g. the base scenario, a scenario including future battery cost development, or a scenario with different battery ageing parameters – are computed to analyse the influence of specific properties or assumptions. A summary of the recommended charging strategies will be given.

If not stated otherwise, monetary values marked with a $ sign in this chapter are given in the currency of Singapore Dollar (SGD).

5.1 Assumptions and Input Parameters

5.1.1 Mobility Behaviour of Battery Electric Vehicles

The mobility behaviour elaborated in Chapter 2 is now used as input for the scenario calculations with the charging optimisation model. A simulation with the mobility model was conducted with a sample of 300 BEVs for a simulation period of four weeks. The simulation resulted in a total of 26 121 trips with a total mileage of 317 244 km, during which an energy amount of 53 MWh is consumed. On average, each BEV drives 1058 km in four weeks and 37.8 km in one day with 3.1 trips per day. The average trip distance is 12.1 km.

The input parameters for the charging optimisation model from the mobility model are E_{nom}, E_{cons}, and b_{park}. The nominal energy content of a BEV's battery $E_{nom}(a)$ is a specific value for each BEV. The energy consumption during each trip $E_{cons}(a,i)$ is generated by the mobility model simulation and depends on the BEV's specific consumption and the trip duration. Last, the input parameter $b_{park}(a,i,t)$ is derived from the mobility model simulation, which indicates at what time steps each BEV is parking and able to be charged.

The simulation period of four weeks is split into four single weeks and the generated input data are divided accordingly. With this data, the charging optimisation model is run four times, each solving the optimisation model for one week of the simulation period.

It is assumed that charging stations are available at any point of time and location.

5.1.2 Battery Price

For the determination of the battery cost of each BEV, the specific battery price $C_{specBatt}$ is required. Nykvist and Nilsson (2015) name industry-wide cost for battery packs of 410 USD per kWh in 2014. Specific battery cost of 380 EUR per kWh on system level for the year 2015 is given by Plötz, Gnann, Kühn, and Wietschel (2014, p. 53) for their base scenario. Pillot (2015) states 400 USD per kWh for 2015. For the calculation of a base scenario in this work, the average of these values is taken and converted into the currency of Singapore Dollar (SGD)[1], yielding 575 SGD per kWh as specific battery cost.

In order to consider and evaluate the influence of falling battery prices, a scenario including future battery cost is computed with the charging optimisation model. As forecast of battery pack cost in 2020, Plötz et al. (2014, p. 53) propose 280 EUR/kWh, Pillot (2015) 250 USD/kWh, and Nykvist and Nilsson (2015) a range from 150 USD/kWh to 500 USD/kWh. Averaging and converting those values results in 413 SGD/kWh. For the calculation of the future battery cost scenario of the charging optimisation model, future battery pack cost of 400 SGD/kWh is assumed.

Furthermore, the resale factor of a battery pack at the end of its life as a traction battery in a BEV plays a role in the calculation of the battery cost. The end of life of an electric vehicle battery was first defined by USABC and DOE National Laboratories (1996) as a residual battery capacity of 80 %. This definition is widely accepted and assumed in many publications (Fischhaber et al., 2016, p. 35). Hence, the factor defining the battery's end of life in the charging optimisation model f_{EOL} is set to 80 %.

Fischhaber et al. (2016) analyse second life utilisation of lithium-ion batteries of BEVs. They mention cost for a new battery pack of 366 EUR/kWh in 2015 and 100 EUR/kWh for one at its end of life as electric vehicle battery, resulting in a resale factor of 27 %. Until 2030, the cost for a new battery is assumed to fall to 219 EUR/kWh, raising the resale factor to 46 % (Fischhaber et al., 2016, pp. 85–86, 95). The resale factor of used traction batteries in the optimisation model f_{resale} is set to 25 % for the base scenario and to 50 % for the future battery cost scenario.

[1] with exchange rates of 1.5323 SGD/EUR and 1.4085 SGD/USD as of 22 April 2016 (Monetary Authority of Singapore, 2016)

The following values serve as input data for the determination of the battery cost within the charging optimisation model:

- specific battery cost $C_{specBatt} = 575\,\text{SGD/kWh}$ for base scenario
  $C_{specBatt} = 400\,\text{SGD/kWh}$ for future battery cost scenario,
- resale factor at end of life $f_{resale} = 25\,\%$ for base scenario
  $f_{resale} = 50\,\%$ for future battery cost scenario,
- end of life factor $f_{EOL} = 80\,\%$.

These assumptions imply higher cost for second life batteries in the future than now. This can be explained by non-linear ageing behaviour of lithium-ion batteries after they have exceeded their end of life in a BEV as defined above. While the batteries have a remaining capacity between 100 % and 80 %, the ageing behaviour can be approximated by a linear function as shown in Chapter 3. However, after the batteries have exceeded the 80 % threshold, a significant loss of capacity in a very short time period can occur at any point of time, resulting in a complete outage of the battery (Schuster et al., 2015). At the moment, it is unsure when the breakdown will occur and therefore, a high risk accompanies second life batteries. But with enhancing battery technology in the future, also the cycle stability during a battery's second life is expected to improve. This results in increasing quality of second life batteries and thus a higher price. Furthermore, the gain in lifetime as well as a larger number of possible applications will raise the demand for second life batteries and therewith the price.

5.1.3 Electricity Price

In order to obtain cost optimal charging strategies generated by the charging optimisation model, one precondition is to include the fluctuating electricity prices of the wholesale electricity market in Singapore. Conducting a charging optimisation using a fixed electricity price for all time periods would be pointless as there is no incentive to temporally shift the charging process and the electricity cost of the charging process would be the same for all possible charging strategies. The fluctuating electricity price is called Uniform Singapore Energy Price (USEP). It is the weighted average of all nodal prices within Singapore's power grid for each half hour of a day and depends on the current electricity demand and supply (Energy Market Authority, 2010, p. 9-4). Since the USEP shows a rough correlation to the electricity demand, the minimisation of charging electricity cost can lead to a smoother electricity demand curve which is a favourable effect. Figure 5.1 displays the USEP as well as the electricity demand in Singapore for one week (Monday, 30 November 2015 to Sunday, 6 December 2015) and it can be observed that peaks and valleys of electricity price and demand coincide.

While small consumers (non-contestable consumers) have to buy electricity at a fixed electricity tariff, consumers with a monthly consumption exceeding 2000 kWh are eligible to be contestable consumers and have the choice to buy from the wholesale electricity market at fluctuating prices (Energy Market Authority, 2015, 2010, p. 4-2). Simulations with the mobility model described in Chapter 2 show that 11 BEVs consume

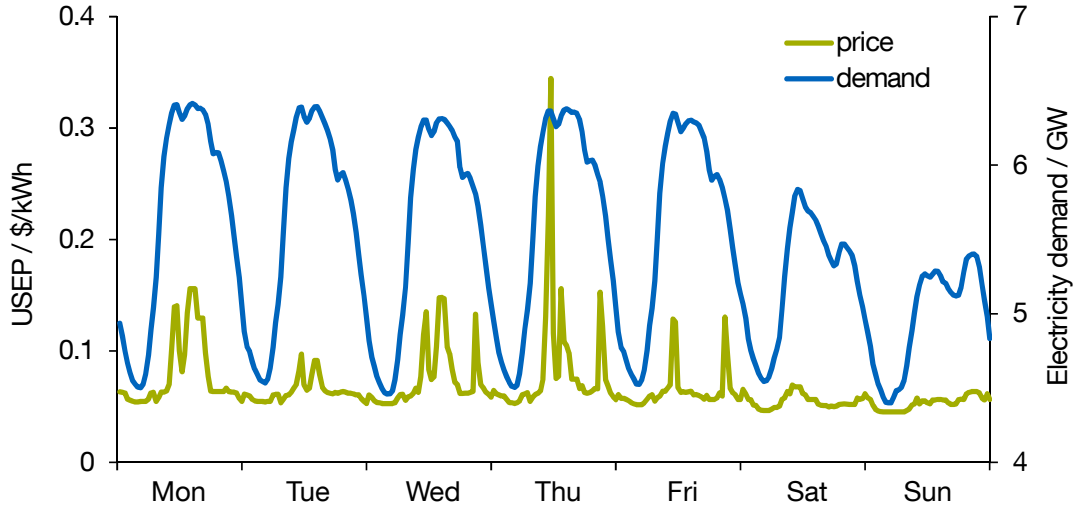

Figure 5.1 – Uniform Singapore Energy Price (USEP) and electricity demand in Singapore for one week (Source: Energy Market Company, 2016b)

roughly 2000 kWh within a month to fulfil their journeys. This means that a charging infrastructure operator providing services for the electricity demand of 11 BEVs already qualifies as a contestable consumer.

Component	Price
Wholesale Electricity Price[2]	fluctuating every half hour
Transmission Charges[3]	peak period (7:00–23:00): 5.26 ct/kWh off-peak period (23:00–7:00): 3.94 ct/kWh
Market Support Service (MSS) Charges[4]	
Billing & connection	0.53 $ per bill (monthly)
MSS basic services	2.89 $ per account (monthly)
Meter reading and data management	2.18 $ per meter (monthly)
Retail market system related charges	0.20236 ct/kWh
Retail settlement uplift	0.12090 ct/kWh
Monthly meter charge	1.83 $ per single phase meter 2.49 $ per three phase meter capped at 12.50 $ per month
Vesting Contract Debits/Credits[5]	a share of consumption is covered by vesting contracts; net benefits or costs associated therewith are allocated to contestable consumers after each month

Table 5.1 – Composition of electricity price and charges for contestable consumers

[2] Available at Energy Market Company (2016b).
[3] See SP PowerAssets Ltd. (2015).
[4] See SP Services Ltd. (2015).
[5] See Energy Market Authority (2010, p. 8-1), Energy Market Authority (2014, p. 19).

Hence, it is a reasonable assumption to use the fluctuating electricity prices of the wholesale market within the charging optimisation. Contestable consumers can buy electricity directly from the wholesale market or indirectly through the Market Support Services Licensee SP Services Ltd. (Energy Market Authority, 2010, p. 4-2). The second option is more common for smaller contestable consumers like a charging infrastructure operator (Energy Market Authority, 2010, p. 11-1).

The price a charging infrastructure operator as a contestable consumer has to pay for the consumed electricity comprises the fluctuating wholesale electricity price[6] as well as some additional fees and charges. Table 5.1 summarises the different components whereof some are consumption-based and some are monthly charges. All prices are given in SGD and subject to goods and services tax (GST) of 7 % (Inland Revenue Authority of Singapore, 2015, p. 1).

Further non-recurring charges add to the monthly recurring charges displayed in Table 5.1. The non-recurring charges apply only when a specific event occurs and can be found in Appendix C.

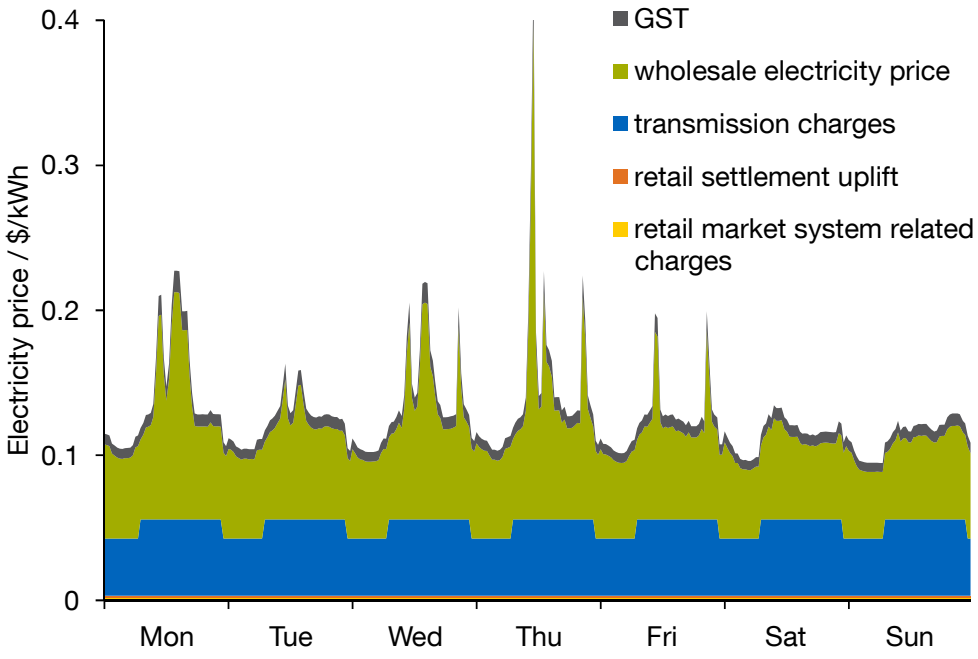

Figure 5.2 – Electricity price for one week

Within the charging optimisation model, only the consumption-based components are considered, since only those can influence the cost for electricity of the charging process. Hence, the term "electricity price" in this work and especially in context of the charging optimisation model refers to the sum of wholesale electricity price, transmission charges, retail market system related charges, retail settlement uplift, and GST. The fluctuating electricity price $pr_{el}(t)$ used as input data for the charging optimisation model is pictured

[6]The wholesale electricity price consists of USEP (which is by far the main part), allocated regulation price, hourly and monthly energy uplift charges, market administration fees, and power system operator fees (Energy Market Company, 2016a).

in Figure 5.2 for the first week of the simulation period. The electricity prices for the entire simulation period of four weeks from Monday, 30 November 2015 to Sunday, 27 December 2015 were downloaded from the Energy Market Company (2016b).

5.1.4 Other Input Parameters

The efficiency factors regarding the charging process – i. e. the battery efficiency η_{batt} and the charging station efficiency η_{chaSt} – obtain the values $\eta_{batt} = 85\,\%$ and $\eta_{chaSt} = 93\,\%$ derived in Section 3.2.1.

The transmission loss factor $f_{traLoss}$ holds a value of 1.038304 according to SP Services Ltd. (2014).

The coefficients h_1, h_2, h_3, h_4 of the cycle ageing constraint (4.39) can be found in Appendix B. The coefficients h_5, h_6 of the calendar ageing constraint (4.44) stem from equation (4.16).

The maximum charge rate $r_{cha,max}$ is set to 1.5 P, as mentioned in Section 4.4.5. With this and constraint (4.32), the maximum allowed charge power P_{max} for each BEV is defined.

The BEVs can be charged with a minimal charge power P_{min} of 2.99 kW, which is the power available at a regular household power socket in Singapore of British Standards BS 1363 at 13 A and 230 V.

The SOC_0 at the beginning of the simulations is set to 50 %. The operating range for the battery SOC is limited by 100 % as natural upper boarder for SOC_{max} and 10 % for SOC_{min}. The lower limit of 10 % is chosen in order to avoid break-downs of BEVs due to depleted batteries as well as to minimise faster battery degradation due to deep discharge.

The time step duration Δt is 0.5 h since the fluctuating electricity price changes half-hourly, as explained earlier in Section 5.1.3.

Table 5.2 summarises the assumptions for the input parameters for the charging optimisation.

5.2 Optimisation Results

5.2.1 Base Scenario

The base scenario is run for 300 BEVs and four weeks simulation period with the input parameters given in Table 5.2. It serves also as reference scenario for the comparison with other scenarios, where input parameters were changed. The simulation period was split into four single weeks and the charging optimisation was conducted separately for each week. One week was chosen as optimisation horizon as a trade-off between computation time and flexibility in the optimisation. Optimising the entire simulation horizon of four weeks would result in very high computation times. Also, the forecasting of travel schedules for a shorter time period is more realistic than for four weeks. On the other hand, when selecting an even shorter optimisation horizon, computation times would decline further, but the flexibility and ability of shifting the charging processes between different points of time is smaller. Hence, the solver has less freedom and the

η_{batt}	85 %
η_{chaSt}	93 %
$b_{park}(a,i,t)$	derived from mobility simulations
$C_{batt}(a)$	see equation (4.33)
$C_{specBatt}$	575 $/kWh (base scenario), 400 $/kWh (future battery cost scenario)
$E_{cons}(a,i)$	derived from mobility simulations
$E_{nom}(a)$	derived from mobility simulations
f_{EOL}	80 %
f_{resale}	25 % (base scenario), 50 % (future battery cost scenario)
$f_{traLoss}$	1.038304
h_1, h_2, h_3, h_4	see Appendix B
h_5, h_6	see equation (4.16)
$P_{max}(a)$	see equation (4.32)
$P_{maxSys}(t)$	derived from electricity load
P_{min}	2.99 kW
$pr_{el}(t)$	retrieved from Energy Market Company (2016b)
$r_{cha,max}$	1.5 P
SOC_0	50 %
SOC_{min}	10 %
SOC_{max}	100 %
Δt	0.5 h

Table 5.2 – Overview of input parameters for the charging optimisation

optimisation results are less precise than with a longer optimisation horizon. Due to these reasons, the optimisation horizon of one week was used.

The results are presented for the entire simulation horizon as well as for each week individually and are summarised in Table 5.3.

The base scenario contains 25 972 trips and parking events respectively during the four week long simulation period with 300 BEVs. During those trips, a total of 53 207 kWh is consumed. Only for 14 075 of the parking events, the charging optimisation model allocates a charging process. During these charging processes, 62 598 kWh are charged to the BEVs. The discrepancy between energy consumed and energy charged derives from the losses within the battery pack. In order to charge the BEVs with 62 598 kWh, 69 887 kWh are drawn from the power system, including transmission losses and losses within the charging station. As a result of the charging optimisation, minimum total charging costs of 9117.12 $ arise, consisting of 7267.61 $ for electricity and 1849.50 $ for battery ageing.

Figure 5.3 illustrates the cost components of the total charging costs. While the electricity cost represent the major share in cost of the charging processes, the battery ageing accounts for around 20 %, both for the entire simulation period and for each week separately. The battery ageing costs are further divided into cycle ageing and calendar ageing costs, of which the calendar ageing cost is roughly 10 times as much as the cycle ageing cost.

This large difference can be attributed to the definitions of cycle and calendar ageing

	Week 1 to 4	Week 1	Week 2	Week 3	Week 4
Number of parking events / –	25 972	6371	6600	6525	6476
Number of charging processes / –	14 075	3375	3472	3618	3610
Energy consumption / kWh	53 207	13 176	13 241	13 468	13 323
Energy charged / kWh	62 598	15 501	15 577	15 845	15 675
Energy from power system / kWh	69 887	17 306	17 391	17 690	17 500
Total cost / $	9117.12	2334.88	2247.65	2249.41	2285.17
Electricity cost / $	7267.61	1871.85	1797.85	1789.17	1808.73
Total ageing cost / $	1849.50	463.03	449.80	460.24	476.44
Cycle ageing cost / $	172.34	38.53	39.55	55.63	38.63
Calendar ageing cost / $	1677.16	424.50	410.25	404.61	437.81
Average charge rate / –	0.21	0.21	0.21	0.21	0.21
Average SOC_{start} / –	0.12	0.12	0.12	0.12	0.13
Average SOC_{end} / –	0.32	0.33	0.32	0.32	0.32
Average ΔSOC / –	0.20	0.21	0.20	0.20	0.20
Average charge power / kW	117.11	119.24	112.07	104.93	115.25

Table 5.3 – Results overview for base scenario

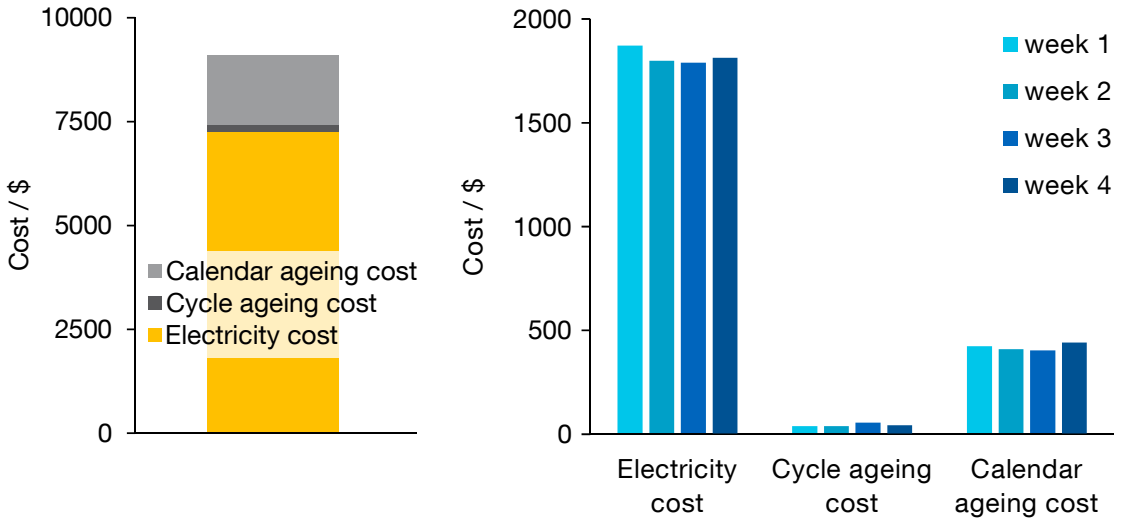

(a) for entire simulation horizon

(b) for week 1 to week 4

Figure 5.3 – Electricity, cycle ageing, and calendar ageing cost for base scenario

elaborated in the battery ageing model in Chapter 3. The methodology developed for the separation of cycle and calendar ageing effects can be found in Section 3.3.2. Therein, the energy fade related to calendar ageing includes calendar ageing effects not only when a BEV is resting without being charged, but also during the charging process itself. The energy fade due to cycle ageing contains only those ageing effects related purely to the charging process. Hence, when a BEV is charged, both cycle and battery ageing effects occur. As long as it is not charged, only calendar ageing can happen. While charging a battery, the cycle ageing is much higher than calendar ageing, with a declining

influence of cycle ageing for lower charge rates (cf. Table 3.4, columns $e_{fade,cal}$ / cycle^{-1} and $e_{fade,cyc}$ / cycle^{-1}, as well as Figure 3.8). However, the BEVs spend on average 22.8 h per day parking but only 1.6 h thereof charging. Also, the average charge rate in the base scenario is rather low (0.21 P), resulting in relatively small cycle ageing effects. All this explains why the calendar ageing cost is that much higher than the cycle ageing cost. A scenario where this relation is turned around can be found in Section 5.2.2, where the charge rate is set to a value of 1 P.

On average, the BEVs are charged with a charge rate of 0.21 P, which is equivalent to a charge time of roughly 5 h for a full charge. Figure 5.4 contains the histogram of the distribution of the charge rates for all 14 075 charging processes. Within all histograms in this chapter, the border value between two bins is included in the lower bin. The big majority of the BEVs is charged rather slowly, with charge rates below 0.4 P. 52 % of the charging processes are operated at a charge rate below 0.2 P and another 45 % at a charge rate between 0.2 and 0.4 P. Only 3 % obtain a charge rate of 0.4 to 0.6 P and less than 1 % of 0.6 to 0.8 P. Charge rates of more than 0.8 P up to the maximum allowed charge rate of 1.5 P are reached in only two out of the 14 075 charging processes. The distribution of the charge rates for the four individual weeks (blue bars) looks similar to the one for the entire simulation period (green bars). When regarding the influence of the charge rate on cycle ageing in Figure 3.10 in Section 3.3.2, one can see that it is relatively small until a charge rate of 0.5 P and increases rapidly thereafter. This explains the small number of charging processes between 0.4 and 0.6 P and the even smaller number above 0.6 P. High charge rates are avoided, because the influence of fast charging on battery ageing is immense.

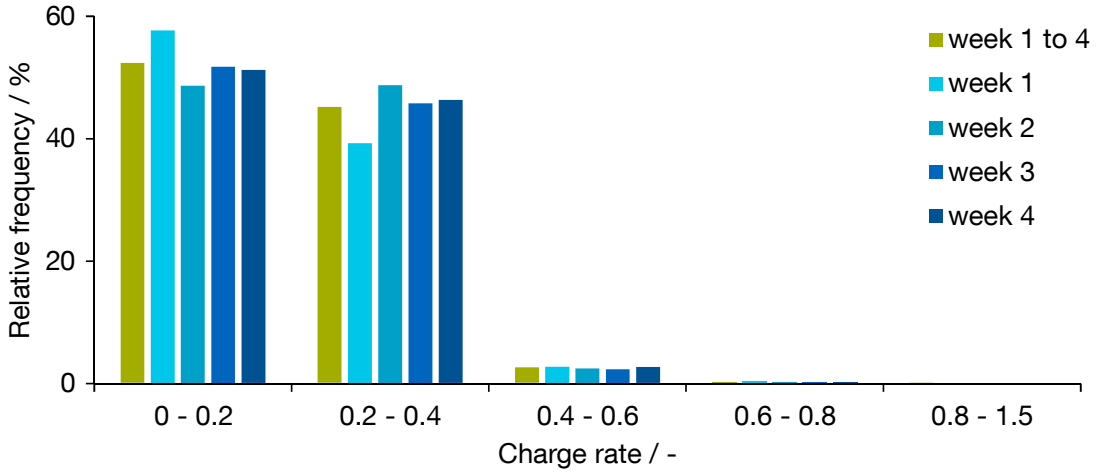

Figure 5.4 – Histogram of charge rates for base scenario

Over 97 % of the charging processes have a ΔSOC of 50 % or less. This means that in almost all cases, no use is made of the full range of the BEVs' batteries but rather little energy is charged in order save battery ageing cost. The average ΔSOC charged during a charging process is 20 %. Figure 5.5 pictures this situation with a histogram of the ΔSOC distribution for the different charging processes in the base scenario. A small ΔSOC

leads to lower cycle ageing cost. This can be derived from Figure 4.5 in Section 4.2.2, which depicts the energy fade depending on SOC_{start}, SOC_{end}, and ΔSOC. The ΔSOC is indicated by diagonals in the graph and the smaller the ΔSOC becomes, the lower the energy fade and therewith the cycle ageing cost gets. Hence, the charging optimisation chooses low ΔSOCs.

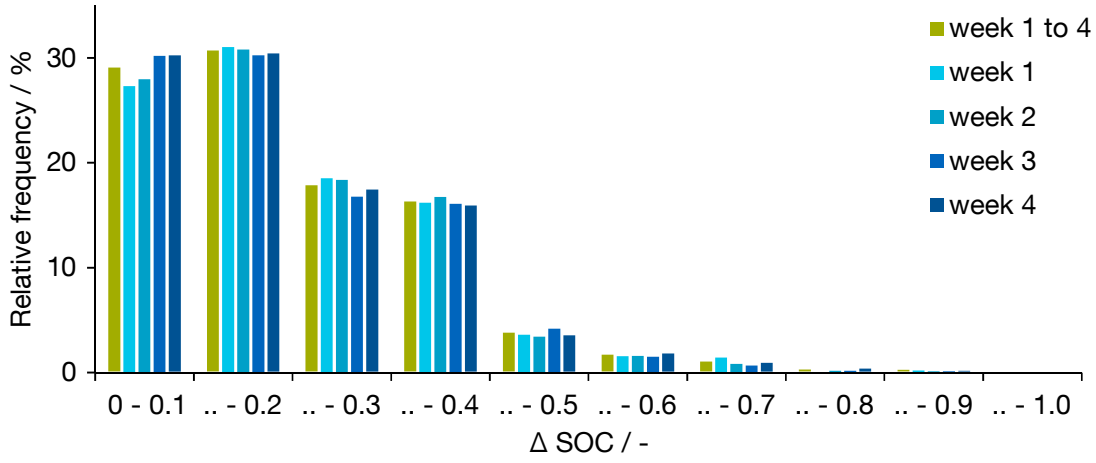

Figure 5.5 – Histogram of ΔSOC for base scenario

Not only the ΔSOC of a charging process has an impact on battery ageing, but also the range of SOCs. On average, the BEVs in the base scenario are charged from an SOC_{start} of 12 % to an SOC_{end} of 32 %. Most of the charging processes (63 %) start at the minimum allowed SOC of 10 %, as indicated by the first bin in Figure 5.6[7]. Thereby, the average SOC is kept low and the calendar ageing cost declines with a lower average SOC. On the other hand, moving the SOC_{start} towards 0 % rapidly increases the cycle ageing cost (see Figure 4.5). However, for an SOC_{start} of 10 % this increase is still moderate and the reduction in calendar ageing cost outweighs the increase in cycle ageing cost. It is interesting to see that the charging strategies generated by the optimisation are contrary to current user behaviour where it is very unusual to operate ICE vehicles always close to an empty fuel tank. Regarding the SOC_{end} distribution in Figure 5.7, 91 % of the charging processes reach an SOC_{end} between 10 % and 50 %. A low SOC_{end} leads both to lower calendar and cycle ageing costs.

For ΔSOC, SOC_{start}, as well as SOC_{end}, the distributions for the entire simulation period, as indicated by the green bars in Figures 5.5 to 5.7, look very similar to the distributions for each individual week, represented by different blue bars.

Figure 5.8 presents the total charge power for all 300 BEVs of the base scenario as well as the electricity price. Figure 5.8a shows this data for the entire simulation period of four weeks, while b displays an extract of Wednesday and Thursday of the first week.

During each day, a peak in charge power appears when the electricity price is at its daily minimum. This can be clearly observed in Figure 5.8b. The peaks occur between

[7] The first bin from 0 % to 10 % actually includes only SOC_{start} values of exactly 10 % due to the minimum allowed SOC.

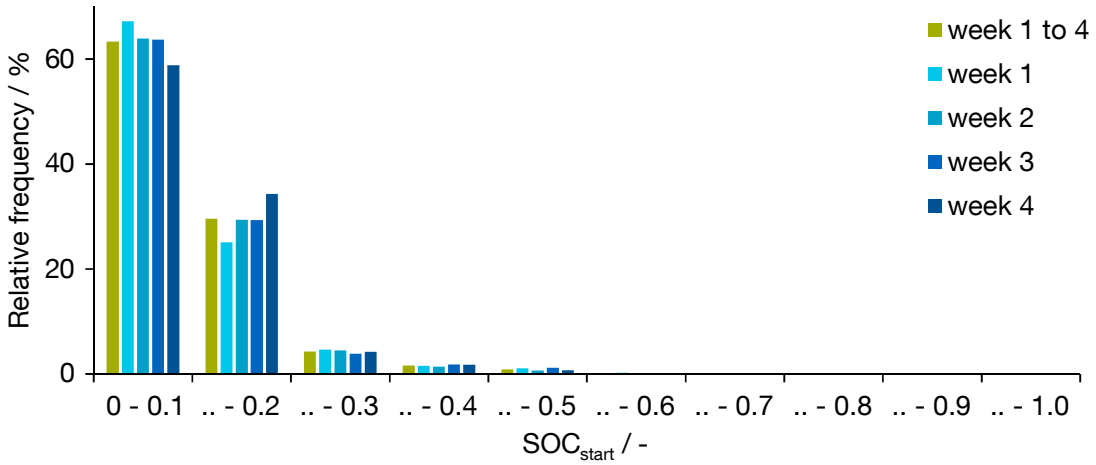

Figure 5.6 – Histogram of SOC_{start} for base scenario

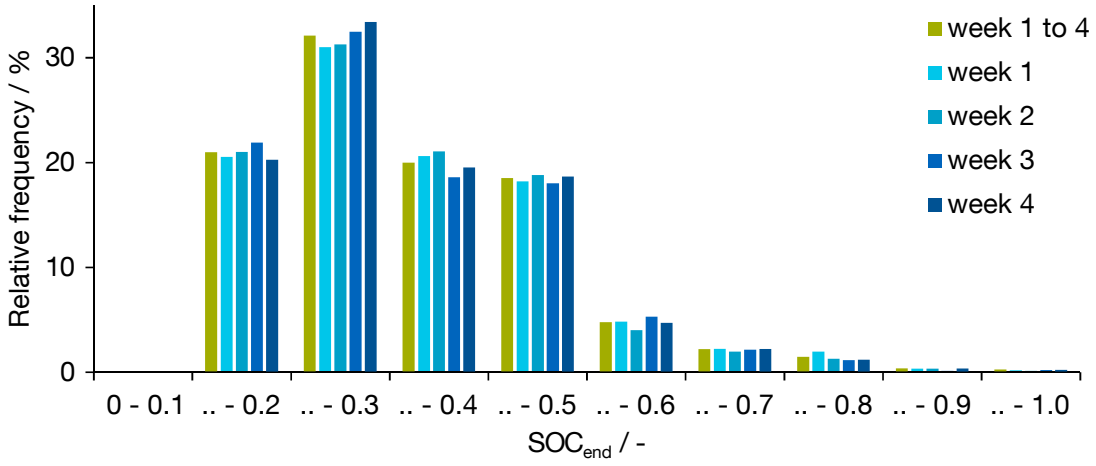

Figure 5.7 – Histogram of SOC_{end} for base scenario

4:00 and 6:00 in the morning, followed by another lower peak between 6:00 and 8:00. The first peak can be explained by the low electricity prices in the early morning hours. In order to keep the average SOC and therewith calendar ageing cost as low as possible, the BEVs are charged during the cheap time steps, but as late as possible before they leave in the morning. The decline of the first peak is due to vehicles starting to leave in the morning between 6:00 and 6:30, corresponding to the analysis of driving behaviour in Singapore elaborated in Chapter 2. When the first vehicles to leave arrive at their destination, they are immediately recharged as electricity prices are still low, leading to a second increase in charge power. Until 8:00 to 8:30, the majority of the vehicles has left and also electricity prices are increasing now, so it is not favourable anymore to charge during the following time steps. Therefore, the total charge power drops to almost zero. Most of those morning peaks reach values between 900 kW and 1500 kW. When all BEVs charge during the cheapest time steps of the day, these values correlate to

an average charge power between 3 kW and 5 kW per vehicle. These low charge power values correspond to the low charge rates discussed earlier.

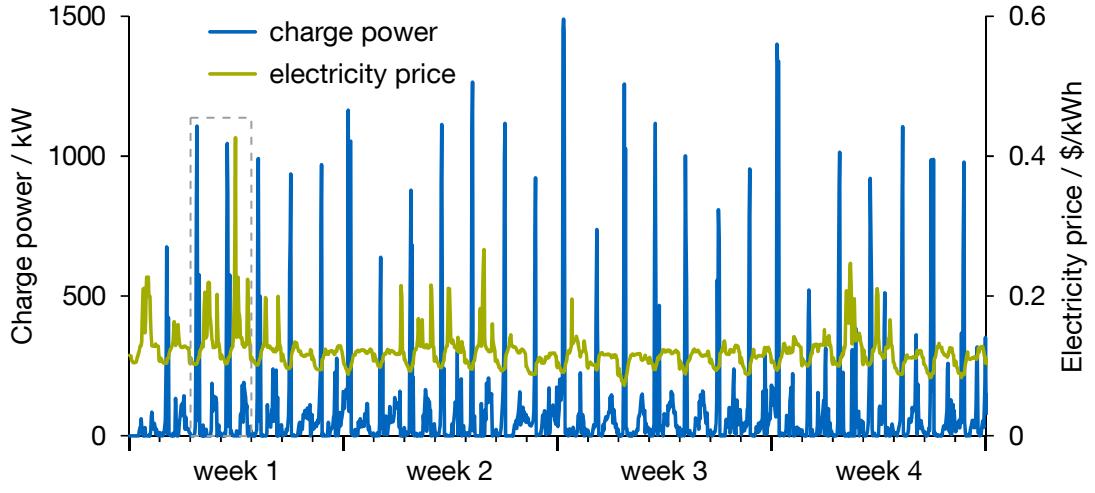

(a) entire simulation period

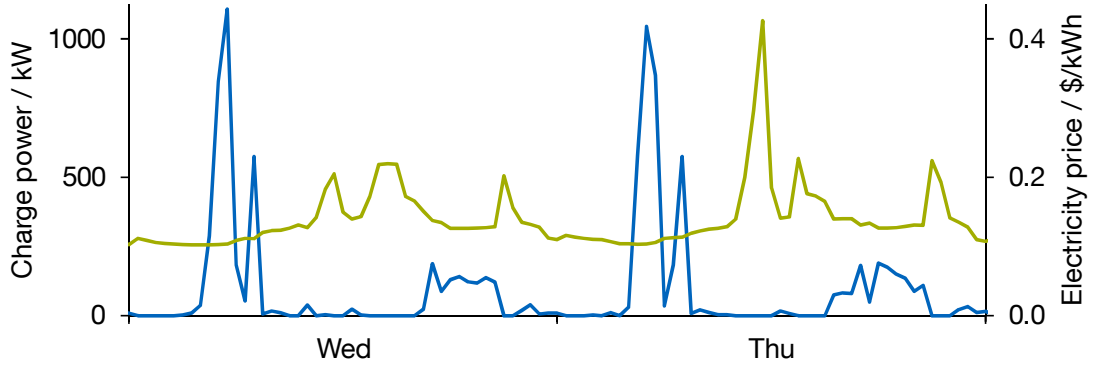

(b) extract of Wednesday and Thursday of week 1

Figure 5.8 – Charge power of all 300 BEVs in the base scenario as well as electricity price

In the further course of the day, several smaller peaks of the charge power coincide with valleys in the electricity price. At night, most BEVs are parking and leave within a relatively narrow time frame in the morning. Compared to this, the travel schedules disperse throughout the day and all the trips are scattered over a longer time period. Hence, the single BEVs do not charge all at once, but distributed more evenly across the day, and the charge power peaks are lower. Compared with the early morning peaks, smaller, but wider peaks of the total charge power occur between roughly 16:00 and 20:00. Within this time frame, electricity prices remain relatively constant at a lower level. Additionally, many trips after work are conducted at some point within this time frame and vehicles can be recharged afterwards at low electricity cost.

During 77 % of the time, BEVs are charged and the average charge power during this time is 117 kW.

To sum up, the analysis of the base scenario suggests to charge slowly, between low

SOCs, during low electricity price periods, and as late as possible before departure.

5.2.2 Scenario Analysis

Scenario Definitions

Since the optimisation results for the base scenario presented in the preceding section show similar results for all four weeks of the simulation periods, the following scenarios are analysed only for the first week of the simulation period. Within the scenario analysis of the charging optimisation model, four different scenarios are compared:

- base scenario,
- scenario including future battery cost development,
- scenario including future battery performance,
- scenario with a high charge rate.

The base scenario includes all assumptions and input parameters as mentioned beforehand in Section 5.1.

For the future battery cost scenario, the specific battery cost is assumed to be lower than for the base scenario in order to mirror the expected enhancement of battery technology in the field of BEV application. Also, the resale factor of a battery pack at the end of its life as a traction battery in a BEV is thought to change in the future. The value of a depleted traction battery for utilisation in a second life appliance is expected to rise due to improved cycle stability also during the second life of a lithium-ion battery. The assumptions and exact values of specific battery cost and resale factor for the future battery cost scenario can be found in Section 5.1.2 as well as Table 5.2. The remaining assumptions and input data are adopted unchanged from the base scenario.

Another anticipated future development is the enhancement of battery performance with increased cycle stability at high charge rates. This allows for higher power when charging and discharging a battery without extensive battery ageing. The scenario including future battery performance reflects this aspect by adapting the battery ageing factor depending on the charge rate as elaborated in Section 3.3.2 and illustrated in Figure 3.10. For the base scenario, the exponential function derived from the battery ageing tests is the basis for the charging optimisation (see Figure 5.9a), whereas within the future battery performance scenario, the ageing factor for charge rates higher than 0.75 P continues linearly with the same gradient as between 0.5 P and 0.75 P, (see Figure 5.9b). As a result, the battery ageing constraints within the optimisation problem have to be recalculated according to the adjusted ageing factor. Other than this, the equations and values remain the same as in the base scenario.

Within the last scenario, the charge power constraints are adapted compared to the base scenario. In this case, the charge rate cannot be chosen freely up to limit a of 1.5 P, but is set to a value of 1 P.

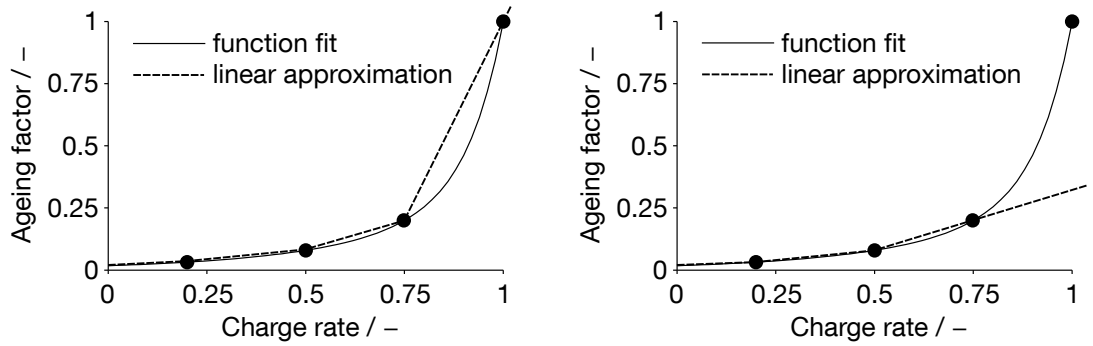

(a) ageing factor for base scenario

(b) ageing factor for future battery performance scenario

Figure 5.9 – Adjustment of ageing factor for future battery performance scenario

Results Summary

Table 5.4 contains the results of all four scenarios. Since the input data regarding the

	Base	Future battery cost	Future battery performance	High charge rate
Number of parking events / –	6371	6371	6371	6371
Number of charging processes / –	3375	2989	3381	4469
Energy consumption / kWh	13 176	13 176	13 176	13 178
Energy charged / kWh	15 501	15 501	15 503	15 504
Energy from power system / kWh	17 306	17 306	17 308	17 310
Total cost / $	2334.88	2068.15	2353.34	3425.08
Electricity cost / $	1871.85	1789.28	1875.62	1889.68
Total ageing cost / $	463.03	278.87	477.72	1535.40
Cycle ageing cost / $	38.53	21.98	35.99	1107.42
Calendar ageing cost / $	424.50	256.89	441.72	427.97
Average charge rate / –	0.21	0.23	0.20	0.66
Average SOC_{start} / –	0.12	0.13	0.13	0.16
Average SOC_{end} / –	0.33	0.36	0.33	0.32
Average ΔSOC / –	0.21	0.23	0.21	0.16
Average charge power / kW	119.24	159.80	119.25	132.89

Table 5.4 – Results overview for different scenarios

300 BEVs stemming from the mobility model are the same for all four scenarios, some values as number of parking events, energy consumption, energy charged, and energy drawn from the power system are unaffected by the different scenario specifications and are equal apart from rounding errors. Within the first three scenarios, the vehicles are charged on average during every second parking event. For the scenario with a high charge rate, this is happening more often (roughly during two out of three parking events), but for a shorter time.

Results on Costs

The total cost of charging lies within the same range for the base and for the future battery performance scenario. This is also the case when the total costs are split up into electricity cost, cycle and calendar ageing cost, as visualised in Figure 5.10. One

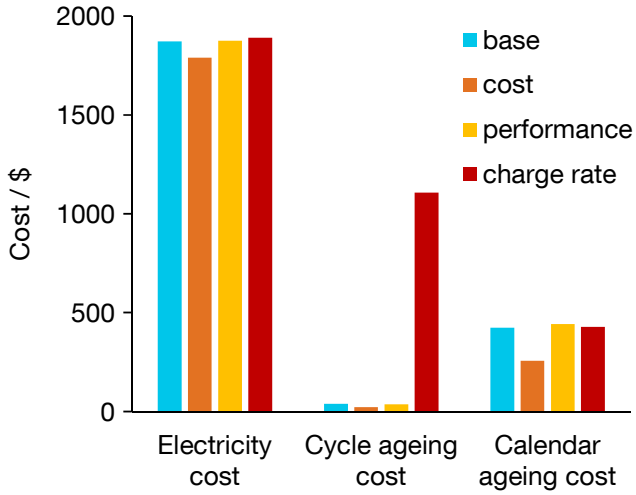

Figure 5.10 – Electricity, cycle ageing, and calendar ageing cost for four scenarios

might expect that for the scenario with future battery performance, where high charge rates affect the battery ageing less severely than in the base scenario, it is charged faster. However, also for the future performance scenario only low charge rates are chosen by the charging optimisation (see Figure 5.11) and therefore, it is only charged at conditions that are the same for the base and the future performance scenario. So, even with the smaller battery ageing effects for high charge rates, the increase in battery ageing cost due to higher charge rates cannot be outweighed by possible savings in electricity cost due to higher amounts of energy charged in cheap periods. This is because there are sufficient low-price periods to complete the charging processes even with low charge rates, which are correlated to low ageing cost.

This leads to the expectation of total cost in the future battery performance scenario being the same or slightly lower than in the base scenario. However, the total cost in the future performance scenario is even 0.8 % higher than in the base scenario.

An explanation can be found in the CPLEX parameter specifying the feasibility tolerance. It indicates how much the variables are allowed to violate their bounds. This parameter can be set to a higher value when there are problems in finding a feasible solution during an optimisation. Then it might happen that the solution is not truly optimal. Setting the tolerance too low might cause CPLEX to find a problem falsely infeasible (IBM, 2016). The feasibility tolerance was set to $1 \cdot 10^{-4}$ in the base and future performance scenario. Therefore, it is possible that there exist slightly better solutions for these two scenarios, with the future performance scenario underbidding the base scenario.

Within the charging optimisation model, the default value for the feasibility tolerance

was increased due to problems in finding a solution. As a result, the solver might have stopped as soon as the tolerances were met and might have led to an objective value of the future performance scenario that is not optimal and therefore larger than the objective value of the base scenario.

Considering future battery cost development, the total cost decreases by 11 % compared to the base scenario. While there is no considerable saving in electricity cost (only 4 %), the reduction in battery cost has an obvious influence on the battery ageing cost: a drop of 43 % of the cycle ageing cost and of 39 % of the calendar ageing cost.

Regarding the scenario where all the BEVs are charged with a high charge rate of 1 P, a substantial rise in total cost is observed (+ 47 %), caused by the tremendous cycle ageing cost being 29 times as high as in the base scenario. This is due to the exponential dependency of the cycle ageing and charge rate (cf. Figure 5.9). As a result, the battery ageing costs account for 45 % of total cost in the high charge rate scenario, while the same cost component has a share of only 20 % in total cost in the base and future performance scenario and merely 13 % in the future cost scenario.

Results on Charge Rates

Figure 5.11 displays the distribution of the charge rates among all charging processes for the four different scenarios. As explained before, the base and future battery performance

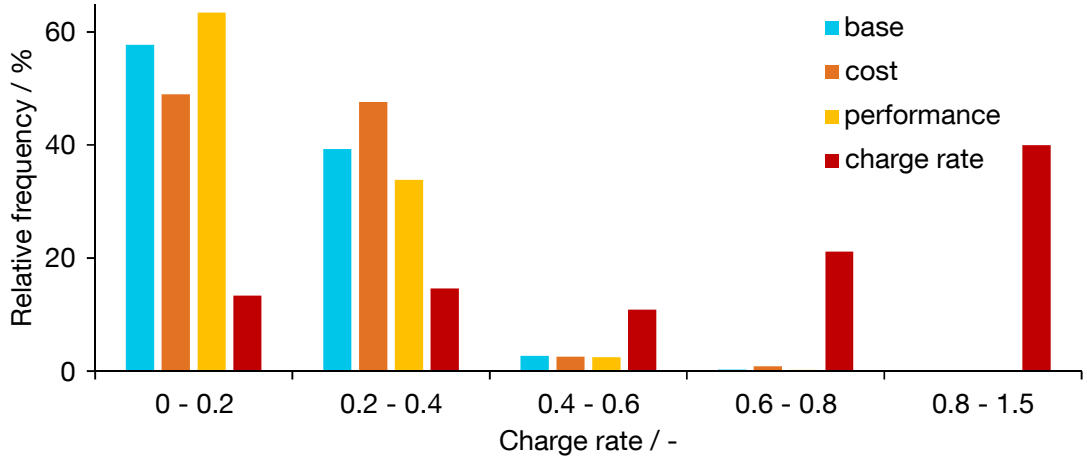

Figure 5.11 – Histogram of charge rates for four scenarios

scenarios indicate similar values, with the lowest charge rates being the most frequently used ones. In the future performance scenario, slightly more vehicles are charged with the slowest charge rates (0 to 0.2 P). This is also mirrored by the slightly slower average charge rate of 0.20 P for the future performance scenario, compared to 0.21 P in the base scenario. In the future battery cost scenario, charge rates in the range of 0 to 0.2 P and 0.2 to 0.4 P exhibit approximately the same frequency. So, in comparison to the other two aforementioned scenarios, more vehicles are charged faster, which is also expressed by the higher average charge rate of 0.23 P. Charge rates over 0.4 P occur only seldomly for all three scenarios (base, future cost, and future performance). Generally speaking,

charge rates are relatively low for all three scenarios due to the bad effects of fast charging on the battery (even with the weakened effects in the future performance scenario).

An obvious deviation can be seen in the high charge rate scenario. Even though the charge rate is set to 1 P in the charging optimisation for this scenario, the histogram displays frequencies different from zero for lower charge rates. This is because the step size of the time intervals is not sufficiently small to fulfil the exact energy demand requirements by the BEVs. For example, when a BEV is already at a relatively high SOC and is charged with 1 P for a further time step, it might happen that it exceeds the maximum SOC of 100 %. Hence, it is not charged for the entire duration of a time step, but only part of it. Consequently, a charge rate of 1 P, which corresponds to a charge power level of say 12 kW during half a time step, results in an average power of 6 kW or a charge rate of 0.5 P for the entire time step. Since the charging optimisation can calculate only for entire time steps, the evaluation of the results presents charge rates lower than 1 P, even though the charge rate is set to 1 P in this scenario. In order to reduce this effect, the high charge rate scenario was calculated with time step size of 10 min instead of 30 min as for the other scenarios. An even smaller time step size would increase computation time further, but would not generate more information on the recommended charging strategy. Since the external electricity price signal has a 30 min resolution, a smaller time step resolution within the charging optimisation would only lead to transforming average values for charge power or charge rate into finely graduated values, but no difference in the objective value (the total charging cost) would be yielded. The bar marking a 40 % frequency in the bin from 0.8 to 1.5 P represents the time intervals charged with 1 P, as higher charge rates are not allowed in this scenario.

Results on SOCs

In all scenarios, the BEVs are most frequently charged with a ΔSOC between 10 % and 20 %, followed by ΔSOCs between 0 % and 10 %, as visualised in Figure 5.12. So, it

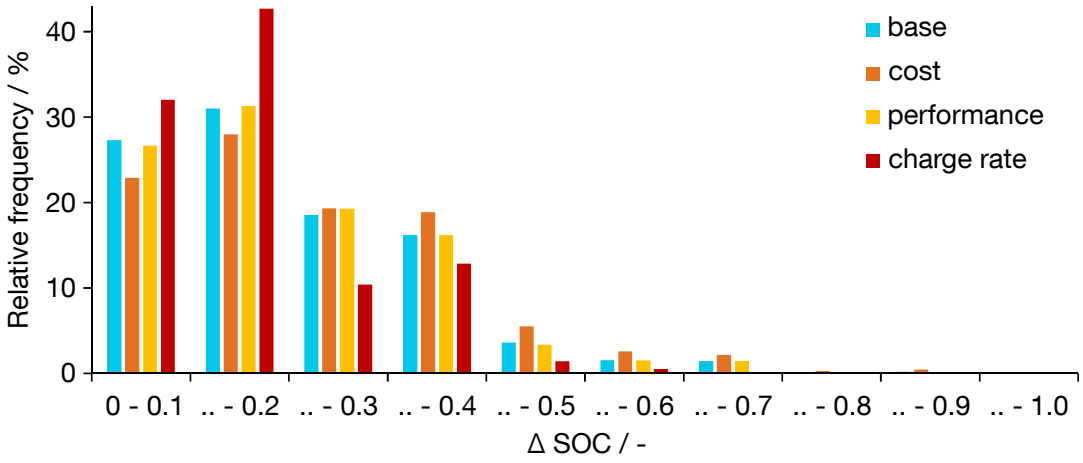

Figure 5.12 – Histogram of ΔSOC for four scenarios

is favourable to recharge only small amounts of energy during each charging process.

Concerning the future battery cost scenario, larger ΔSOCs occur more often, as battery ageing costs have a smaller impact compared to the other scenarios. In contrast to this, the high charge rate scenario proposes more often smaller ΔSOCs. Since the battery ageing cost for a fixed charge rate of 1 P is quite high and cannot be reduced by lowering the charge rate, the optimisation makes use of other options to reduce battery ageing effects. Only very few ΔSOCs above 70 % occur, mainly in the future battery cost scenario, where battery ageing cost is generally on a lower level. There is no ΔSOC above 90 % at all, because the minimum SOC of 10 % and the maximum SOC of 100 % allow a maximum ΔSOC of 90 %.

Examining the histograms of SOC_{start} and SOC_{end} in Figures 5.13 and 5.14, a rather similar distribution is found for the base, future cost, and future performance scenario. Most BEVs are discharged to the minimum SOC of 10 % or at least to an SOC between

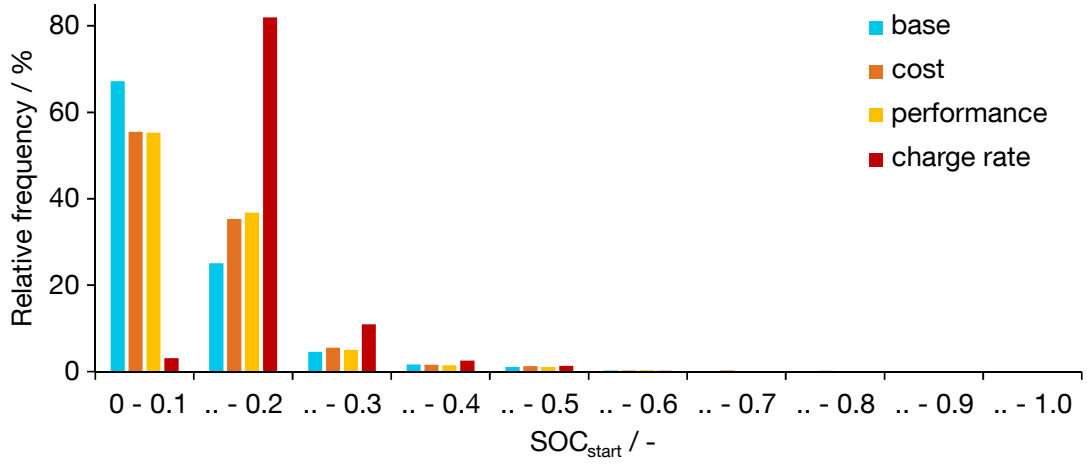

Figure 5.13 – Histogram of SOC_{start} for four scenarios

10 % and 20 % before the charging process is started. Always discharging to low SOCs leads to a decreased average SOC, which has the positive effect of reduced calendar ageing. Also, the SOC_{end} is kept rather low, i. e. below 50 % in more than 90 % of the cases in the base and future performance scenario and more than 85 % in the future cost scenario. This again leads to a low average SOC. Besides keeping the average SOC low to reduce calendar ageing, charging processes up to a very high SOC_{end} are avoided because of the exponential form of the cycle ageing function towards an SOC_{end} of 100 % (cf. Figure 3.11). Only very few charging processes (below 1 % for all scenarios) reach an SOC_{end} between 90 % and 100 %. An operation range within low SOCs is also beneficial in terms of cycle ageing. As long as the batteries are not discharged below 10 %, which is guaranteed by the minimum SOC constraint of the charging optimisation model, cycle ageing effects remain at a low level (cf. Figure 3.11). The future cost scenario has a small shift in frequencies from lower to higher SOC_{end} compared to the base and future performance scenario, because due to the cheaper batteries in this scenario, extended battery ageing effects become affordable.

This picture looks a little different for the high charge rate scenario. The tendency

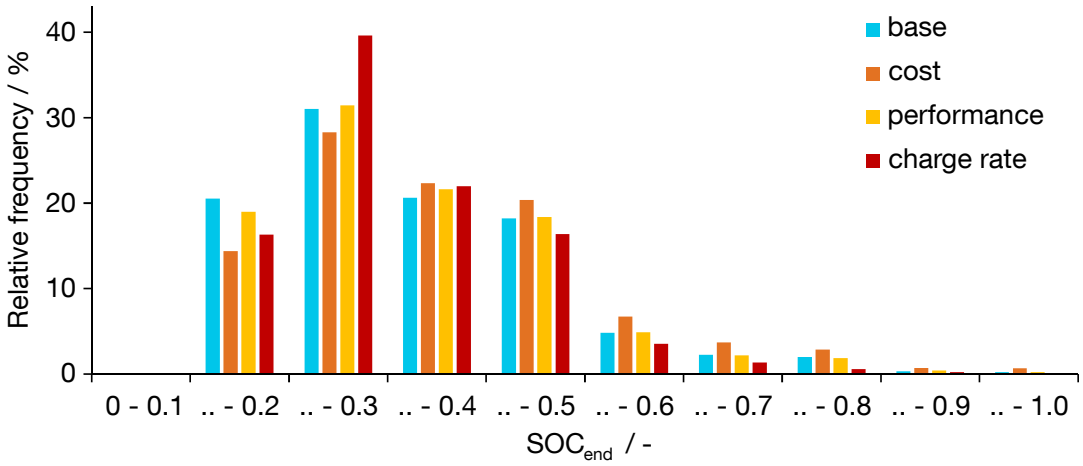

Figure 5.14 – Histogram of SOC_{end} for four scenarios

to keep the values for SOC_{start} and SOC_{end} and therewith also ΔSOC as low as possible during the charging processes is even more distinct than in the other scenarios, because the battery ageing cost due to the high charge rate of 1 P cannot be reduced and therefore other opportunities are taken, as explained before.

Results on Charge Power

The charge power curve for all 300 BEVs is displayed in Figure 5.15 for the four different scenarios. For reasons of enhanced visualisation, the charge power curves of the four scenarios were separated by adding distances of 100 kW between two curves, i. e. adding 100, 200, and 300 kW to each point of the future cost, future performance, and high charge rate curve, respectively. The four curves show similar patterns and parallel behaviour over the course of time with peaks occurring during the same time steps. The reasons for the appearance of the different peaks during the course of day (clearly visible in Figure 5.15b) was explained in detail in Section 5.2.1 for the base scenario. These reasons apply also to the other scenarios discussed within this section.

The difference between the charge power curves of the scenarios lies in the width and height of the peaks. The high charge rate scenario exhibits the highest peaks. The early morning peaks are not only higher, but also narrower compared to the other scenarios. With the high charge rate, more energy can be charged within shorter time and therefore, the time periods with low electricity prices are better utilised.

Observing the future battery cost scenario, the early morning peaks are very pronounced, just like for the high charge rate scenario. Another peak higher than the other scenarios appears in the late afternoon to evening. During the rest of the day, the future battery cost scenario implements less charging power compared to the other scenarios. Due to the lower battery price in this scenario, it has to be taken less care of battery preserving charging and the applied charging strategy can take advantage of the low electricity price periods.

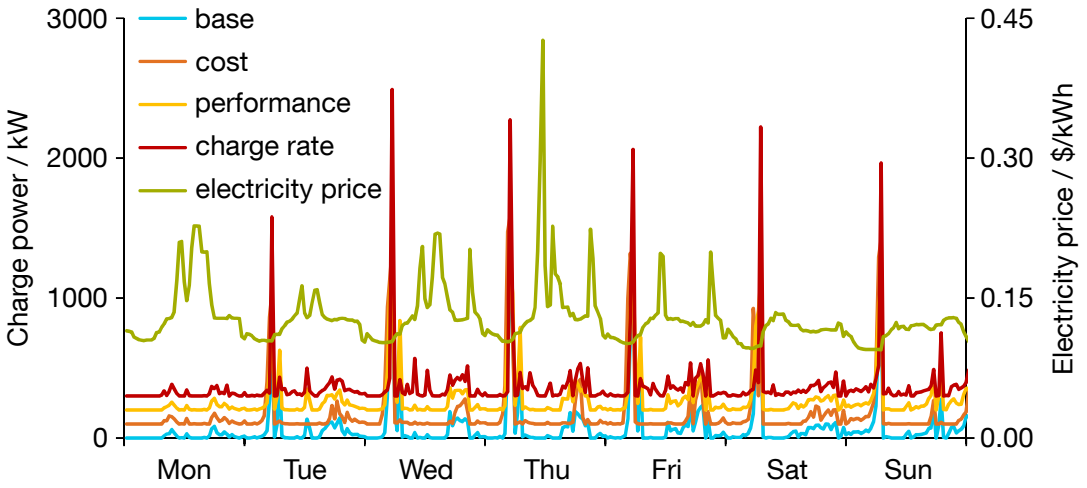

(a) week 1

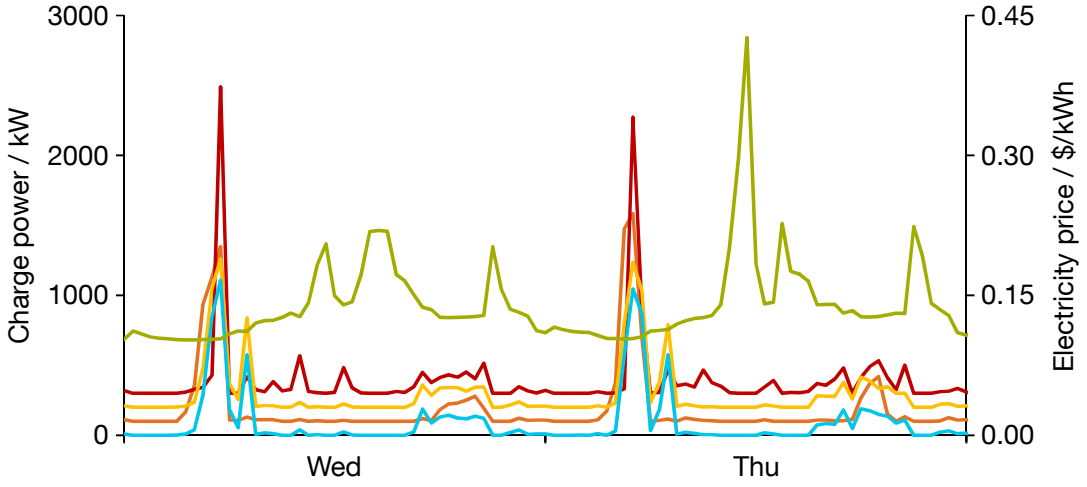

(b) Wednesday and Thursday of week 1

Figure 5.15 – Charge power of all 300 BEVs for four scenarios as well as electricity price. Please note that the curves in both figures were separated by 100 kW for purpose of illustration

Comparing the base and the future battery performance scenario, no significant deviation can be identified, as it was the case for the other charging optimisation results discussed earlier.

Resulting from the charge power curves, the average charge power for the sum of 300 BEVs yields a value of 119 kW for the base and future performance scenario in which 70 % of the time is used for charging. The second highest average charge power of 133 kW occurs within the high charge rate scenario. Consequently, the time for charging is less (62 %), which corresponds to higher but narrower peaks of the red charge power curve. The future battery cost scenario presents the highest value of 160 kW. Due to lower cost for battery ageing, only 52 % of the time is used for charging. This results from the course of the orange charge power curve, which contains more time steps with a value of 0 kW than the other three scenarios, but the peaks in the early morning and in the evening are higher.

When looking at the charge power profiles together with the electricity demand of Singapore in Figure 5.16, it is obvious that the highest peaks in charge power coincide with the deepest demand valleys. Also, the other charge power peaks occur during

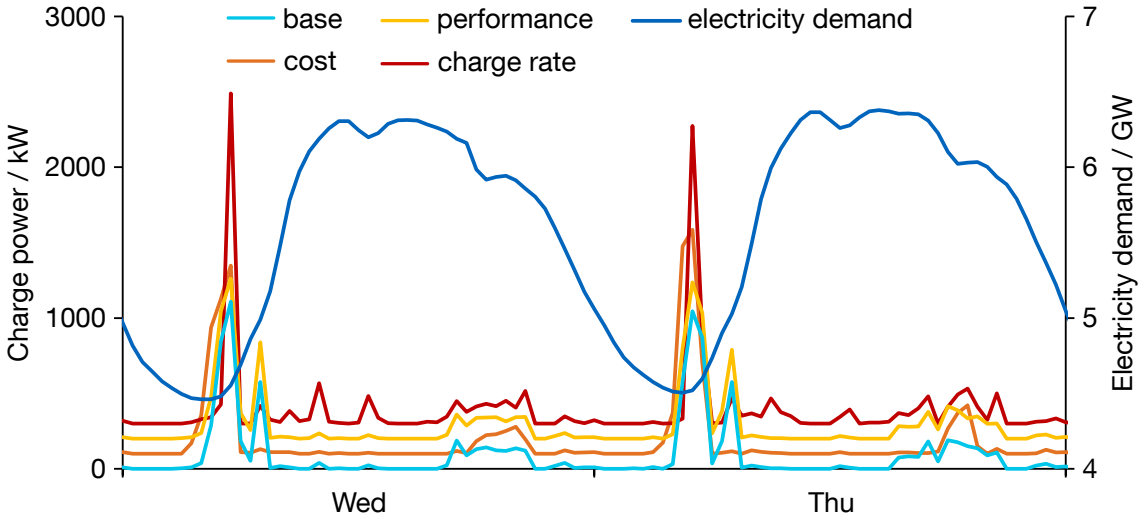

Figure 5.16 – Charge power for four scenarios as well as electricity demand for Wednesday and Thursday of week 1

smaller demand valleys or at least during times of relatively lower demand. Hence, the charging optimisation under consideration of electricity prices additionally leads to valley-filling and therefore has a favourable effect on the power system load. However, when a very large amount of BEVs is charging according to the elaborated charging strategies, the risk of new demand peaks due to extensive BEV charging during low-priced periods arises. To counteract this effect, a power system load constraint was implemented in the charging optimisation problem (see equation (4.45) in Section 4.4). Thereby, a limit for the total charge power of all BEVs together is introduced and the BEVs may not be allowed anymore to charge all at the same time. Thus, additional load peaks caused by charging of a very large number of BEVs can be avoided. The power system load constraint was not used in the presented scenarios with 300 BEVs,

as it would have no influence. For scenarios with a larger number of BEVs, like the total vehicle population of 602 311 cars in Singapore in 2015 (Land Transport Authority, 2015b), it would take effect but for such a scenario, more computing power is needed.

5.3 Solver and Computation

The computational programming of the optimisation problem was conducted in a GAMS (General Algebraic Modeling System) 24.1.2 environment. In order to solve the different scenarios of the charging optimisation problem, GAMS calls the IBM ILOG CPLEX Optimizer version 12.6. The pre- and post-processing of the data was performed in MATLAB 2014a.

The scenario calculations were performed on a windows workstation with a Windows 7 Professional SP1 64-bit operating system, an Intel(R) Core(TM) i7-3770 CPU @ 3.40 GHz, and 32 GB RAM.

Table 5.5 gives an overview of computation times for the different scenarios. Differences in computation time can be explained by different input data from the mobility model (as it is the case for the different weeks), which can cause the solver to take differently long to find a feasible solution. The MIP tolerance was set to $1 \cdot 10^{-5}$ for all scenarios, while the feasibility tolerances were set according to Table 5.5. The feasibility tolerances were adapted in cases where the solver had difficulties in finding a feasible solution.

Scenario	Feasibility tolerance	Computation time
Base (week 1)	$1 \cdot 10^{-4}$	1:07:59
Base (week 2)	$1 \cdot 10^{-4}$	1:17:40
Base (week 3)	$1 \cdot 10^{-3}$	7:14:48
Base (week 4)	$1 \cdot 10^{-3}$	4:19:09
Future battery cost	$1 \cdot 10^{-3}$	0:26:50
Future battery performance	$1 \cdot 10^{-4}$	0:28:09
High charge rate	$1 \cdot 10^{-3}$	0:41:48

Table 5.5 – Computation times and feasibility tolerances for different scenarios

5.4 Recommended Charging Strategies

The battery ageing cost accounts for one fifth of the total charging costs in the base and future battery performance scenario. This is a substantial share in total cost and is very likely to be much higher when no charging optimisation including battery ageing effects is applied. In the scenario where a future decrease in battery cost is assumed, the share lessens to 13 % but still plays a role. When the charge rate is not a variable but set to a value of 1 P, the battery ageing cost rises to a share of even 45 %. Therefore, it is crucial to involve the aspect of battery ageing into a charging optimisation model for BEVs.

The scenario analysis demonstrates that the SOC range in which a BEV is operated should be kept rather low. In roughly 90 % of the simulated charging processes, the charging optimisation generates optimal charging strategies with an operation range within 10 % to 50 % SOC. Thereby, calendar ageing effects can be minimised. Also cycle ageing effects are kept at a low level as long as a deep discharge below 10 % SOC is avoided. This is prevented anyway by the minimum SOC limit of 10 % allowed by the charging optimisation model.

In all scenarios in which the charge rate is flexible (base, future battery cost, and future battery performance scenario) and can be optimally allocated by the charging optimisation, only low charge rates are chosen. Even for the scenario with future battery performance, where the effect of fast charging is assumed to be less severe, no fast charging is applied. When charging with higher power, a larger share of the energy required by the BEVs can be recharged during periods of low electricity prices and thus electricity cost can be lowered. However, the high charge power is attached to increased battery ageing cost (namely cycle ageing cost). The direct link between charge power and cycle ageing cost makes this a major effect and explains the avoidance of fast charging. The scenario analysis shows that the increased battery ageing costs are not outweighed by the reduction in electricity cost, not even in the future battery performance scenario. Consequently, an improved ageing behaviour for higher charge rates does not have an effect on the charging strategies. Only when the energy fade increases even slower for higher charge rates than in the future performance scenario, the electricity cost saving effect might prevail. Summing up, it is favourable to charge the BEVs with a low charge power for a time period of 2.5 h to 5 h or even more (relating to a full charge).

Regarding the point of time for recharging the BEVs, the charging optimisation indicates periods of low electricity prices as preferable. The most desired charging time is in the early morning hours from 4:00 to 6:00. During the night hours, the electricity price is at its daily minimum. The vehicles are charged when electricity prices are still low, but as late as possible in order to keep the average SOC low. Other options for recharging the batteries are in the course of a day whenever valleys in the electricity price curve occur. A larger number of BEVs also use the time in the morning after they arrive at work and before electricity prices rise severely (between 6:00 and 8:00). Also in the late afternoon and evening (16:00 to 20:00), when electricity prices are constantly at a relatively low level, a lot of BEVs are charging to compensate for the energy consumption of their trips after work.

These recommended charging strategies apply to the example of Singapore, as the mobility behaviour used as input for the charging optimisation model stems from data concerning Singapore. However, they can still be used as a general instruction for charging battery electric vehicles.

As trip distances are relatively short due to the bounded dimensions of the island of Singapore, the limited range of BEVs satisfies all mobility requirements. Hence, one could assume that it is sufficient to charge only once in several days. However, the charging optimisation shows that the BEVs are charged more often with smaller amounts of energy, given that sufficient charging stations are available. Thus, Singapore's supposed advantage for BEVs due to its short travel distances is not utilised. It is charged even

when unnecessary in terms of remaining travel range. Since the charging optimisation proposes numerous recharging processes, the recommended charging strategies can also be applied to other locations where distances are longer and thus more frequent charging is necessary.

Chapter 6

Conclusion and Outlook

Controlled charging of battery electric vehicles (BEVs) is intensely discussed and a focus of current research. The temporal and spatial flexibility of the electricity demand stemming from battery electric vehicles can be used advantageously for the power system. However, also battery ageing effects occur during charging of a BEV. Hence, the costs for charging BEVs consist of electricity cost as well as battery ageing cost. Due to the substantial share of the battery cost in the total cost of a BEV, it is crucial to consider the battery ageing effects during the charging process besides electricity price or other power system restrictions.

This thesis presented a mathematical optimisation model, proposing optimal charging strategies for BEVs while taking battery ageing behaviour as well as fluctuating electricity prices into account. While considering vehicle parameters and travel requirements of the BEV users, charging profiles at minimal cost were generated. The aim of the charging optimisation model was to find the optimal trade-off between electricity price induced charging and saving battery lifetime.

In order to simulate the travel requirements of the BEVs, which shall be optimised in the charging optimisation, an agent-based mobility model was developed, representing the driving and parking behaviour in Singapore. The model was based on statistical data on travel behaviour in Singapore. It comprises a vehicle model for calculation of energy consumption of BEVs, based on vehicle parameters of currently available BEV models. A BEV population corresponding to the current vehicle population in Singapore was generated. Travel schedules and corresponding energy consumptions of a sample of BEVs were simulated over a specific time period and served as input for the calculations of the charging optimisation model.

To model the battery ageing behaviour taking place during the charging process of a BEV, battery ageing tests were conducted. Both cycle and calendar ageing tests were performed in order to analyse the ageing effects during operation and storage of a battery. The physical quantity of energy content was chosen to measure the battery ageing effects, including both capacity fade and impedance rise.

During the cycle ageing tests, the test cells were cycled between different states of charge (SOCs) and with different charge rates. Thereby, different influence factors were examined. In some of the tests, different charge rates were applied, while the SOC range

was kept constant. In other cycle ageing tests, the charge rate remained unchanged and the SOC range in which the cells were cycled was varied. The development of the energy fade depending on the different influence factors was fitted with two different functions: one exponential function of the charge rate as well as another exponential function depending on the SOC_{start} and SOC_{end} of the charging process. The combination of these two fitted functions resulted in a multidimensional cycle ageing function, indicating the energy fade for any combination of SOC_{start}, SOC_{end}, and charge rate. The analysis of the cycle ageing tests showed that higher charge rates as well as charging to high SOCs or discharging to low SOCs accelerates cycle ageing.

For the calendar ageing tests, cells were stored at different temperatures and different SOCs and measured after regular time intervals. The energy fade during storage at different SOCs was approximated by two linear equations. The calendar ageing tests yielded higher energy fade for higher SOCs.

Both the multidimensional cycle ageing function as well as the two linear functions approximating the calendar ageing behaviour were integrated in the charging optimisation model. The ageing functions provided the basis for the calculation of the battery ageing costs (divided into cycle and calendar ageing costs) as part of the objective function. The objective function minimised the total charging costs, consisting of electricity cost and ageing cost. To reach this objective, the optimisation model allocated the charging processes by deciding how the BEVs were recharged: during which parking event and specifically during which time steps thereof, from what SOC_{start} to what SOC_{end} and at what charge rate. Thereby, the travel requirements of the BEVs had to be met: The BEVs always had to be able to fulfil the subsequent trips and they were not allowed to violate a minimum SOC limit representing a buffer. The charging optimisation model yielded charging strategies for BEVs which made use of periods with low electricity prices and preserved the batteries' lifetime at the same time.

The optimisation problem was initially formulated as a mixed-integer non-linear programme. By applying the reformulation-linearisation technique to the charge power term, the non-linear constraints containing this term were reformulated as linear constraints. Also the non-linear, convex cycle ageing function was piecewise-linearly approximated by tangent hyperplanes. Thereby, the mathematical formulation of the optimisation problem could be transformed into a mixed-integer linear programme. The linearisation led to increased performance during solving the optimisation problem.

In case of non-convex battery ageing data, an alternative solution for the piecewise linear approximation of the multidimensional cycle ageing function was elaborated. A theoretical approach of multidimensional interpolation by means of SOS2 variables was derived and included in the charging optimisation problem. Thus, the charging optimisation model was made available for a general application with any cell chemistry which might feature non-convex ageing behaviour.

The developed charging optimisation model was used to find optimal charging strategies for a sample of 300 BEVs. The travel schedules and corresponding energy consumption of the BEVs were generated by the mobility model. The optimisation horizon was set to one week and different scenarios were analysed. The scenarios included a base scenario, a scenario with future battery cost development, a scenario

with future battery performance, as well as a scenario with a high charge rate.

The battery ageing costs resulted in a share of 13 % to 45 % of the total charging costs, depending on the scenario. Even for the most optimistic scenario with 13 % (future battery cost scenario), this is a substantial share which should not be omitted when optimising charging strategies. Especially because the cost of battery ageing will rise even more when not considered in the charging optimisation model. Also, the batteries of BEVs would reach their end of life much earlier if battery ageing is omitted and only power system related aspects are optimised.

The results of the scenario analysis showed that the BEVs should be operated within a SOC range of 10 % to 50 % to keep calendar ageing and also cycle ageing effects at a minimum. Substantial damage to the battery due to deep discharge below 10 % is avoided by the minimum SOC limit. Fast charging was applied only very seldomly due to its considerable influence on battery ageing and mostly low charge rates, resulting in charging times of 2.5 h to 5 h (relating to a full charge), were applied. Thereby, the cycle ageing cost remained at a low level. Even for the scenario with future battery performance, in which fast charging had a less severe effect on battery ageing, the possible savings in electricity cost due to charging more energy in low-priced periods could not outweigh the increased battery ageing cost. An improved ageing behaviour at higher charge rates does not have an effect on the charging strategies, unless this improvement is far superior than assumed in the scenario analysis conducted in this work. The effect of fast charging became obvious in the scenario in which the BEVs were charged at a charge rate of 1 P (equalling a full charge in 1 h). In this scenario, the battery ageing cost rose to a value more than three times as high as in the base scenario and reached a share of 45 % in the total charging costs.

Another outcome of the calculations of the charging optimisation model was that most BEVs were charged in the early morning hours when electricity prices and also the electricity demand in Singapore were at their minima. The BEVs were charged when electricity price and demand were still low, but as late as possible before they departed in order to keep the average SOC and therewith calendar ageing low. Other points of time used for charging coincided with smaller valleys in electricity price and demand or periods with relatively low values of the aforementioned. As a consequence, charging electricity cost were kept at a low level and valley-filling effects occurred in the power system.

When a very large amount of BEVs shall be optimised in terms of their charging processes, the additional constraint on the power system load, implemented in the charging optimisation model, will take effect. Additional load peaks due to excessive BEV charging at the same time can be avoided and the charging processes are distributed over a longer time window. The power system load constraint can also be applied to single planning areas, thereby implementing different load restrictions for different areas of Singapore and representing, for example, possible local bottlenecks at substations or the distribution grid. The mobility model already assigned the trips and parking locations to the different planning areas of Singapore during simulation of the travel schedules. Another effect of a large number of BEVs charging at the same time can be rising prices during these periods and, as a consequence thereof, a shift in charging load

to other periods.

The charging optimisation model can be expanded to include further ageing parameters as, for example, varying battery temperature. To integrate additional ageing parameters, the battery ageing function can be extended by another dimension reflecting the influence of an extra parameter. Both the approach of piecewise linear approximation by tangential hyperplanes (for convex ageing functions) and by means of SOS2 variables (for non-convex ageing functions) is applicable to ageing functions of even more dimensions. The tangential hyperplanes then would have as many dimensions as ageing parameters. Also the dimensions and quantity of SOS2 variables and corresponding constraints are scaled up according to the number of ageing parameters.

Another aspect to be analysed is the optimal battery dimensioning in terms of energy content in order to fulfil the travel requirements of BEV users. Larger batteries have additional weight, resulting in a higher energy consumption of the BEVs. This effect was already incorporated in the mobility model. However, smaller batteries need to be operated closer to their limits in order to still fulfil all travel requirements and thus experience increased ageing. Hence, in future research, a coupling of the charging optimisation with an optimisation for battery dimensioning makes sense to find the optimal trade-off between reducing battery cost due to smaller batteries and increasing ageing effects because of more extreme battery operation.

Even though the charging optimisation model indicated that it is best to operate one's BEV always close to the lower SOC limit, many users might not feel comfortable by doing so and privilege their personal preferences over the optimal charging patterns in terms of battery ageing and electricity cost. To reflect this, user preferences can be embraced in the definition of the agents' travel behaviour in the mobility model.

Instead of optimising the charging processes for a fixed time horizon, whereat one cannot be totally sure about the exact travel schedules of the agents, the approach of a receding horizon can be used. The Energy Market Company (2016b) provides a forecast of the electricity prices for 24 h to 36 h, which is updated every 30 min. With this forecast and the current prognosis of the travel schedules, the next 24 h can be optimised. After 30 min, the following 24 h are optimised, including updated electricity prices and travel schedules. Thereby, short-term changes in travel schedules can be considered and a real-time application of the charging optimisation model becomes possible. In contrast to the simulation horizon of one week, the flexibility to shift charging processes among different parking events decreases due to the shorter optimisation horizon. However, computation times will shorten which is important for real-time applications. The charging optimisation can take place separately for each vehicle and the intelligence can be located within each vehicle. However, when a very large amount of BEVs shall be optimised and power system restrictions come into play, the charging load of all optimised BEVs needs to be coordinated and distributed over space and time. Therefore, all BEVs have to be connected and the control will take place within this network or cloud.

Another possible application of the battery ageing model and the battery ageing constraints derived therefrom is within a load aggregator, which combines flexible loads of BEVs to take part in a demand response programme as it was done by Recalde Melo,

Trippe, Gooi, and Massier (2016).

Instead of optimising the charging strategies for traction batteries in BEVs, the optimisation model could also be applied to stationary battery storage systems for the power grid. Replacing the input generated by the mobility model, which represents the BEVs' energy requirements resulting from their travel schedules, with profiles of power system load and renewable energy production, optimal charge and discharge profiles for the stationary batteries can be elaborated.

Summing up, the battery ageing costs occurring during charging processes which were analysed and determined within this work exhibit the necessity to include battery ageing behaviour into a charging optimisation model. The way of charging a BEV has an immense influence on the lifetime of the battery. Recommended charging strategies regarding only power system aspects should be reconsidered. When omitting battery ageing effects during the optimisation of charging strategies, battery ageing costs will rise and BEVs will reach their end of life sooner. Slow charge rates and operation in low to moderate SOC ranges proved to be advantageous charging strategies. Charging processes were predominantly scheduled during periods of low electricity prices, coinciding with valleys or low levels of electricity demand. The benefit of the charging optimisation model elaborated in this work is that also battery ageing aspects are considered and formulated as part of a comprehensive mathematical optimisation model for charging strategies of battery electric vehicles.

Appendix A

Additional Ageing Data

In the work of Trippe et al. (2014), cells of the model CGR18650CH LITHIUM ION from Panasonic were aged with full cycles with different charge modes. Some cells were charged with constant power (1 P and 2 P charge rate) and some with constant current (1 C and 2 C charge rate). All cells were discharged with constant current at 1 C. Figure A.1 shows that there is no significant discrepancy between the ageing behaviour of constant power and constant current charging.

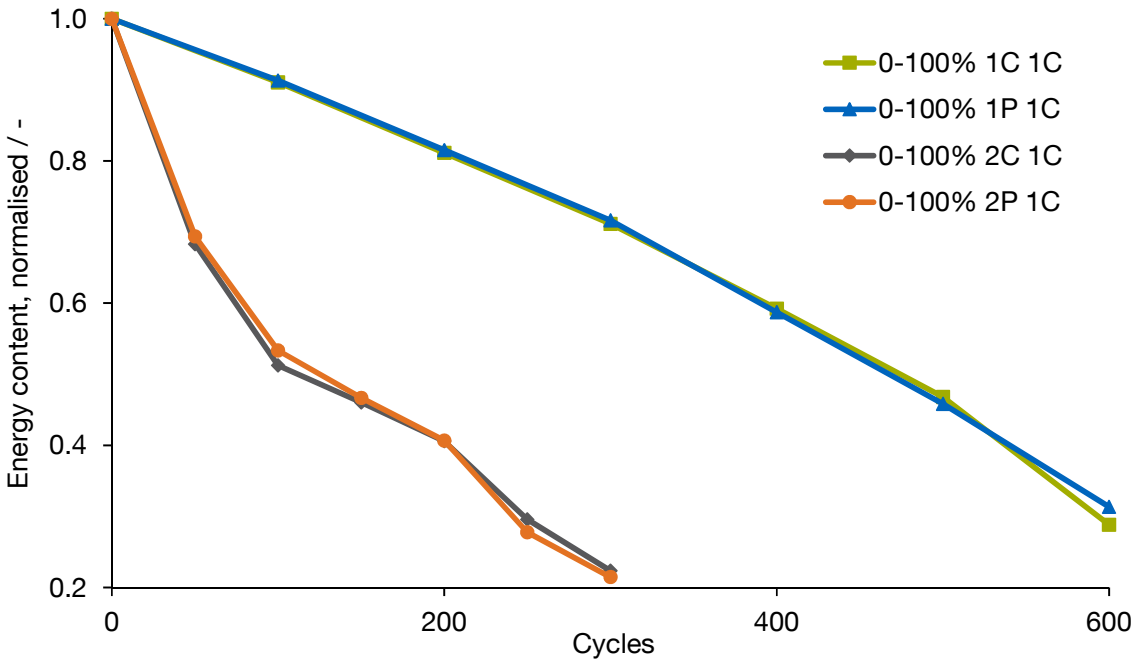

Figure A.1 – Energy content of test cells versus full cycles for different charge modes

Figure A.2 displays the normalised capacity versus the accumulated energy throughput for cycle ageing tests no. 5 to 10. The development of the capacity resembles the energy content development (cf. Figure 3.4).

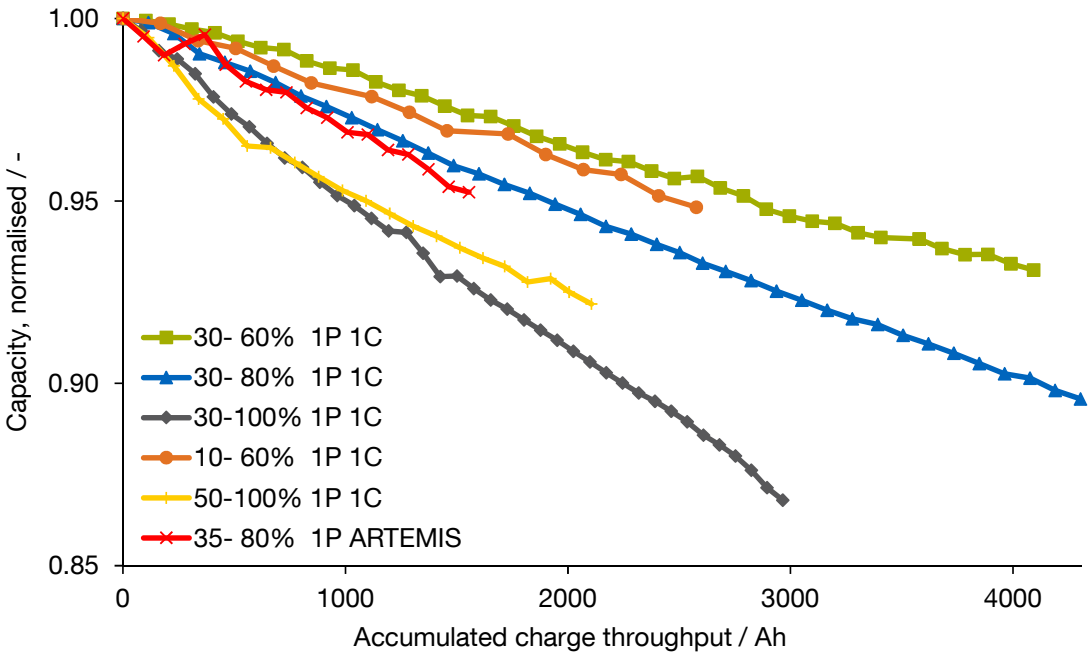

Figure A.2 – Capacity of test cells versus accumulated charging charge throughput for different SOCs

Figure A.3 to A.5 show the normalised energy content over the course of time for the calendar ageing tests no. 11 to 15, 21 to 25, and 26 to 30 at 20 °C, 40 °C, and 60 °C.

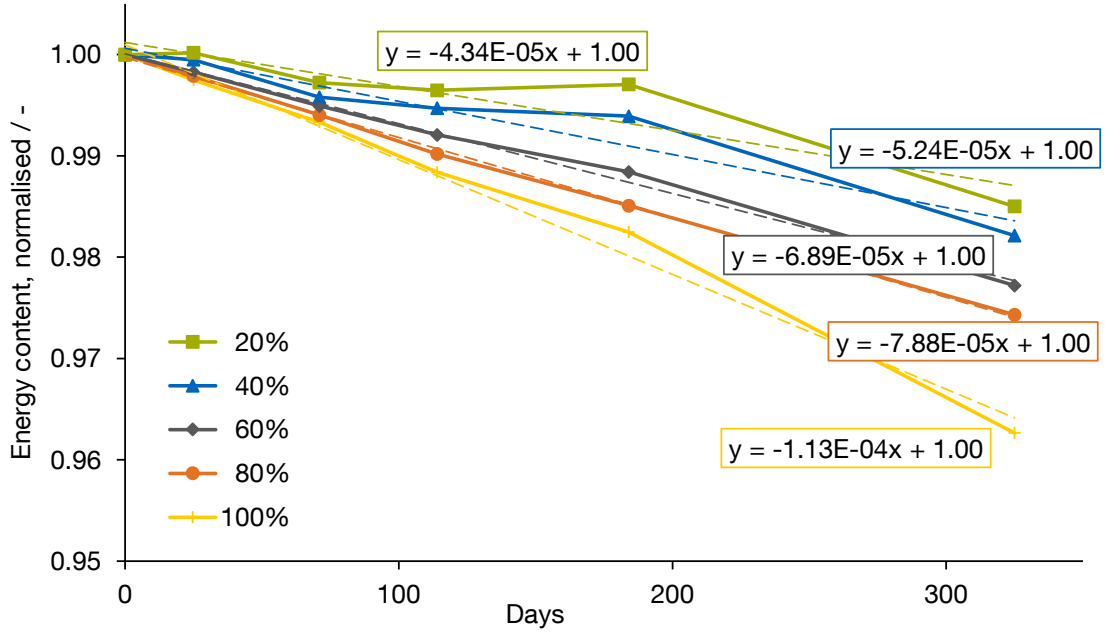

Figure A.3 – Energy content of test cells versus time for different static SOCs at 20 °C

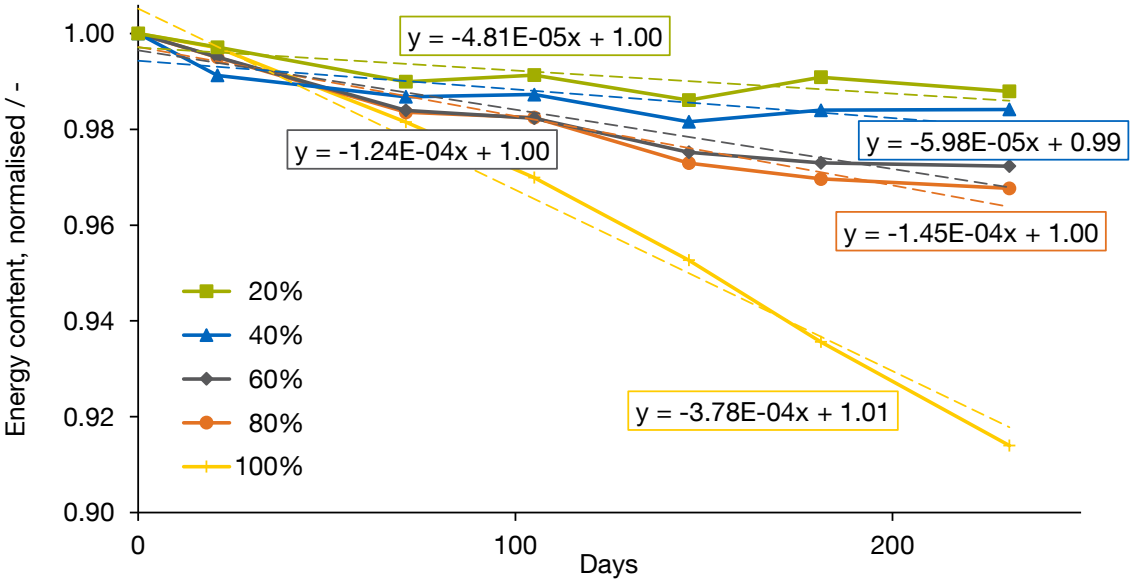

Figure A.4 – Energy content of test cells versus time for different static SOCs at 40 °C

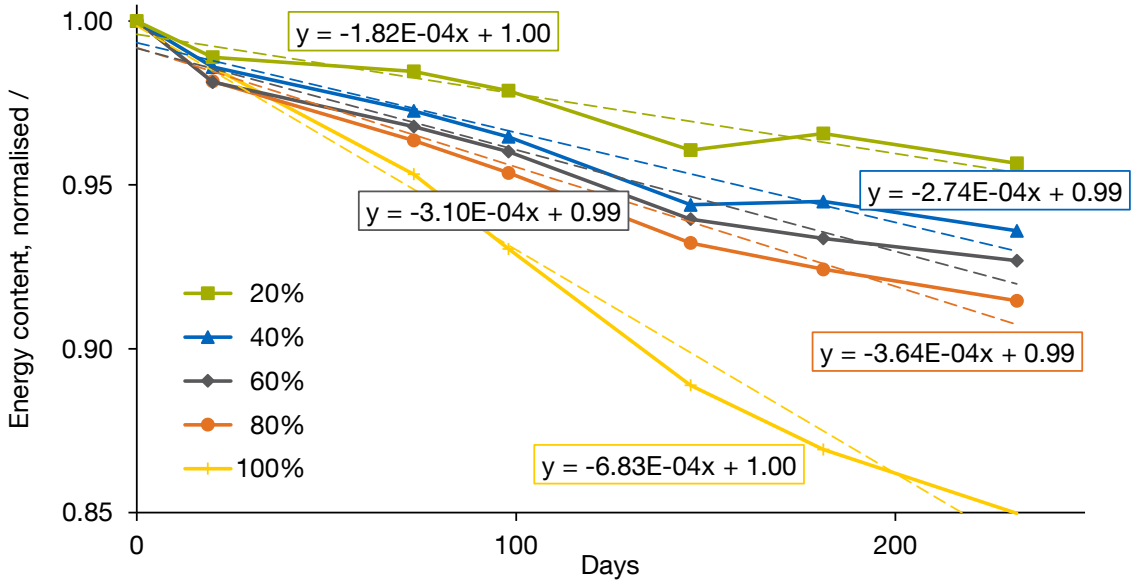

Figure A.5 – Energy content of test cells versus time for different static SOCs at 60 °C

Appendix B

Equations for Approximated Cycle Ageing Function

The functional equations of the tangent hyperplanes which approximate the three-dimensional cycle ageing function have the form

$$\begin{aligned} e^{tanHyp}_{fade,cha}(x) = \quad & \text{coefficient}^{\,x}_{SOC_{start}} \cdot SOC_{start} \\ & + \text{coefficient}^{\,x}_{SOC_{end}} \cdot SOC_{end} \\ & + \text{coefficient}^{\,x}_{r_{cha}} \cdot r_{cha} \\ & + \text{constant} \end{aligned}$$

as in equation (4.14). $\text{Coefficient}^{\,x}_{SOC_{start}}$, $\text{coefficient}^{\,x}_{SOC_{end}}$, $\text{coefficient}^{\,x}_{r_{cha}}$, and constant are referred to as h_1, h_2, h_3, and h_4 in equation 4.39. There are 142 hyperplane equations. The coefficients and the constant for x or $k = 1, \ldots, 142$ are given in the following table:

x or k	$\text{coefficient}^{\,x}_{SOC_{start}}$ or h_1	$\text{coefficient}^{\,x}_{SOC_{end}}$ or h_2	$\text{coefficient}^{\,x}_{r_{cha}}$ or h_3	constant or h_4
1	-1.87E-04	1.00E-06	1.36E-05	1.54E-06
2	-4.67E-04	2.51E-06	3.63E-05	-7.53E-06
3	-1.17E-03	6.29E-06	1.30E-04	-7.08E-05
4	-5.87E-03	3.15E-05	1.23E-03	-1.09E-03
5	-1.88E-04	1.48E-06	1.40E-05	1.30E-06
6	-4.69E-04	3.69E-06	3.73E-05	-8.44E-06
7	-1.18E-03	9.27E-06	1.34E-04	-7.45E-05
8	-5.88E-03	4.63E-05	1.26E-03	-1.13E-03
9	-1.88E-04	2.18E-06	1.45E-05	8.71E-07
10	-4.70E-04	5.44E-06	3.87E-05	-9.95E-06
11	-1.18E-03	1.37E-05	1.39E-04	-8.04E-05
12	-5.90E-03	6.83E-05	1.31E-03	-1.19E-03
13	-1.89E-04	3.21E-06	1.53E-05	1.40E-07
14	-4.73E-04	8.02E-06	4.08E-05	-1.24E-05
15	-1.19E-03	2.01E-05	1.46E-04	-8.96E-05

16	-5.94E-03	1.01E-04	1.38E-03	-1.28E-03
17	-1.91E-04	4.75E-06	1.65E-05	-1.10E-06
18	-4.77E-04	1.19E-05	4.40E-05	-1.65E-05
19	-1.20E-03	2.98E-05	1.57E-04	-1.04E-04
20	-5.98E-03	1.49E-04	1.48E-03	-1.42E-03
21	-1.93E-04	7.12E-06	1.82E-05	-3.23E-06
22	-4.82E-04	1.78E-05	4.86E-05	-2.33E-05
23	-1.21E-03	4.46E-05	1.74E-04	-1.28E-04
24	-6.05E-03	2.23E-04	1.64E-03	-1.63E-03
25	-1.97E-04	1.12E-05	2.09E-05	-7.23E-06
26	-4.90E-04	2.79E-05	5.57E-05	-3.55E-05
27	-1.23E-03	6.99E-05	2.00E-04	-1.69E-04
28	-6.16E-03	3.50E-04	1.88E-03	-1.98E-03
29	-2.01E-04	2.03E-05	2.54E-05	-1.69E-05
30	-5.03E-04	5.07E-05	6.77E-05	-6.34E-05
31	-1.26E-03	1.27E-04	2.42E-04	-2.56E-04
32	-6.31E-03	6.37E-04	2.29E-03	-2.66E-03
33	-3.45E-06	1.00E-06	9.43E-07	7.09E-08
34	-8.62E-06	2.51E-06	2.52E-06	-6.11E-07
35	-2.16E-05	6.29E-06	9.01E-06	-5.13E-06
36	-1.08E-04	3.15E-05	8.50E-05	-7.69E-05
37	-3.93E-06	1.48E-06	1.31E-06	-1.70E-07
38	-9.80E-06	3.69E-06	3.49E-06	-1.52E-06
39	-2.46E-05	9.27E-06	1.25E-05	-8.81E-06
40	-1.23E-04	4.64E-05	1.18E-04	-1.15E-04
41	-4.63E-06	2.18E-06	1.85E-06	-5.97E-07
42	-1.15E-05	5.45E-06	4.93E-06	-3.04E-06
43	-2.90E-05	1.37E-05	1.77E-05	-1.47E-05
44	-1.45E-04	6.84E-05	1.67E-04	-1.74E-04
45	-5.66E-06	3.24E-06	2.65E-06	-1.34E-06
46	-1.41E-05	8.08E-06	7.06E-06	-5.56E-06
47	-3.54E-05	2.03E-05	2.53E-05	-2.41E-05
48	-1.77E-04	1.01E-04	2.38E-04	-2.64E-04
49	-7.17E-06	4.89E-06	3.84E-06	-2.67E-06
50	-1.79E-05	1.22E-05	1.02E-05	-9.88E-06
51	-4.49E-05	3.06E-05	3.67E-05	-3.94E-05
52	-2.25E-04	1.53E-04	3.46E-04	-4.06E-04
53	-9.40E-06	7.88E-06	5.69E-06	-5.38E-06
54	-2.35E-05	1.97E-05	1.52E-05	-1.82E-05
55	-5.89E-05	4.94E-05	5.44E-05	-6.74E-05
56	-2.95E-04	2.47E-04	5.13E-04	-6.46E-04
57	-1.27E-05	1.55E-05	8.97E-06	-1.30E-05
58	-3.17E-05	3.87E-05	2.39E-05	-4.00E-05
59	-7.95E-05	9.70E-05	8.57E-05	-1.35E-04

60	-3.98E-04	4.85E-04	8.08E-04	-1.16E-03
61	-1.04E-06	1.01E-06	7.77E-07	-1.90E-07
62	-2.59E-06	2.51E-06	2.07E-06	-1.12E-06
63	-6.49E-06	6.30E-06	7.42E-06	-5.79E-06
64	-3.25E-05	3.15E-05	7.00E-05	-7.11E-05
65	-1.51E-06	1.48E-06	1.14E-06	-4.34E-07
66	-3.77E-06	3.70E-06	3.05E-06	-2.04E-06
67	-9.47E-06	9.30E-06	1.09E-05	-9.48E-06
68	-4.73E-05	4.65E-05	1.03E-04	-1.09E-04
69	-2.21E-06	2.21E-06	1.69E-06	-8.75E-07
70	-5.52E-06	5.51E-06	4.50E-06	-3.59E-06
71	-1.38E-05	1.38E-05	1.61E-05	-1.55E-05
72	-6.92E-05	6.91E-05	1.52E-04	-1.69E-04
73	-3.24E-06	3.37E-06	2.50E-06	-1.71E-06
74	-8.09E-06	8.41E-06	6.68E-06	-6.36E-06
75	-2.03E-05	2.11E-05	2.39E-05	-2.55E-05
76	-1.01E-04	1.06E-04	2.26E-04	-2.63E-04
77	-4.76E-06	5.64E-06	3.80E-06	-3.62E-06
78	-1.19E-05	1.41E-05	1.01E-05	-1.22E-05
79	-2.98E-05	3.54E-05	3.63E-05	-4.51E-05
80	-1.49E-04	1.77E-04	3.43E-04	-4.32E-04
81	-6.99E-06	1.22E-05	6.27E-06	-9.96E-06
82	-1.74E-05	3.05E-05	1.67E-05	-3.01E-05
83	-4.38E-05	7.64E-05	5.99E-05	-9.94E-05
84	-2.19E-04	3.82E-04	5.65E-04	-8.37E-04
85	-1.00E-06	1.01E-06	7.75E-07	-1.99E-07
86	-2.51E-06	2.52E-06	2.07E-06	-1.15E-06
87	-6.30E-06	6.32E-06	7.41E-06	-5.83E-06
88	-3.15E-05	3.16E-05	6.99E-05	-7.13E-05
89	-1.48E-06	1.51E-06	1.15E-06	-4.57E-07
90	-3.69E-06	3.76E-06	3.06E-06	-2.10E-06
91	-9.27E-06	9.44E-06	1.09E-05	-9.63E-06
92	-4.64E-05	4.72E-05	1.03E-04	-1.10E-04
93	-2.18E-06	2.34E-06	1.71E-06	-9.88E-07
94	-5.44E-06	5.84E-06	4.56E-06	-3.89E-06
95	-1.36E-05	1.47E-05	1.63E-05	-1.63E-05
96	-6.83E-05	7.33E-05	1.54E-04	-1.74E-04
97	-3.21E-06	4.13E-06	2.63E-06	-2.40E-06
98	-8.01E-06	1.03E-05	7.02E-06	-8.18E-06
99	-2.01E-05	2.59E-05	2.51E-05	-3.06E-05
100	-1.01E-04	1.29E-04	2.37E-04	-2.96E-04
101	-4.72E-06	9.97E-06	4.54E-06	-7.94E-06
102	-1.18E-05	2.49E-05	1.21E-05	-2.36E-05
103	-2.96E-05	6.25E-05	4.34E-05	-7.66E-05

104	-1.48E-04	3.12E-04	4.09E-04	-6.30E-04
105	-1.00E-06	1.03E-06	7.79E-07	-2.16E-07
106	-2.51E-06	2.58E-06	2.08E-06	-1.19E-06
107	-6.29E-06	6.47E-06	7.45E-06	-5.96E-06
108	-3.15E-05	3.24E-05	7.02E-05	-7.21E-05
109	-1.48E-06	1.64E-06	1.17E-06	-5.63E-07
110	-3.69E-06	4.10E-06	3.12E-06	-2.38E-06
111	-9.27E-06	1.03E-05	1.12E-05	-1.04E-05
112	-4.63E-05	5.14E-05	1.05E-04	-1.16E-04
113	-2.18E-06	3.10E-06	1.84E-06	-1.67E-06
114	-5.44E-06	7.74E-06	4.90E-06	-5.70E-06
115	-1.36E-05	1.94E-05	1.76E-05	-2.13E-05
116	-6.82E-05	9.71E-05	1.66E-04	-2.06E-04
117	-3.21E-06	8.45E-06	3.37E-06	-6.71E-06
118	-8.00E-06	2.11E-05	9.00E-06	-1.96E-05
119	-2.01E-05	5.30E-05	3.22E-05	-6.20E-05
120	-1.00E-04	2.65E-04	3.04E-04	-4.93E-04
121	-1.00E-06	1.17E-06	8.02E-07	-3.23E-07
122	-2.51E-06	2.91E-06	2.14E-06	-1.47E-06
123	-6.29E-06	7.31E-06	7.66E-06	-6.76E-06
124	-3.15E-05	3.65E-05	7.23E-05	-7.74E-05
125	-1.48E-06	2.40E-06	1.30E-06	-1.25E-06
126	-3.69E-06	5.99E-06	3.47E-06	-4.19E-06
127	-9.27E-06	1.50E-05	1.24E-05	-1.55E-05
128	-4.63E-05	7.52E-05	1.17E-04	-1.48E-04
129	-2.18E-06	7.42E-06	2.58E-06	-5.99E-06
130	-5.44E-06	1.85E-05	6.88E-06	-1.71E-05
131	-1.36E-05	4.65E-05	2.46E-05	-5.28E-05
132	-6.82E-05	2.33E-04	2.32E-04	-4.04E-04
133	-2.51E-06	4.81E-06	2.49E-06	-3.29E-06
134	-6.29E-06	1.21E-05	8.91E-06	-1.18E-05
135	-3.15E-05	6.03E-05	8.40E-05	-1.10E-04
136	-1.48E-06	6.72E-06	2.04E-06	-5.56E-06
137	-3.69E-06	1.68E-05	5.45E-06	-1.56E-05
138	-9.27E-06	4.21E-05	1.95E-05	-4.69E-05
139	-4.63E-05	2.11E-04	1.84E-04	-3.45E-04
140	-2.51E-06	1.56E-05	4.47E-06	-1.47E-05
141	-6.29E-06	3.92E-05	1.60E-05	-4.32E-05
142	-3.15E-05	1.96E-04	1.51E-04	-3.07E-04

Table B.1 – Coefficients of hyperplane equations

Appendix C

Charges Related to Electricity Consumption

Further non-recurring transmission service charges (exclusive of GST) are as follows (SP PowerAssets Ltd., 2015):

- Attendance charges for power failure caused by fault within consumer's installation: 30 $ per attendance
- Reconnection charges for involuntary disconnection and reconnection: 15 $ per connection (office hours), 100 $ per connection (after office hours)
- Charges for voluntary temporary disconnection and reconnection: 100 $ per low tension feeder (after office hours)
- Re-appointment charges for energisation of service connection: 45 $ per connection
- Meter service charges:
  - Site testing of meter: 30 $ per meter per trip
  - Additional charges for site testing: 150 $ per trip (weekday after office hours), 300 $ per trip (weekend, public holiday)
  - Auditing of meter data: 100 $ per man-day
  - Express service for meter installation: 150 $ per man-day per site (weekday), 300 $ per man-day per site (weekend, public holiday)
  - Meter installation / replacement of metering transformers: 150 $ per man-day per site (weekday after office hours), 300 $ per man-day per site (weekend, public holiday)

Further non-recurring market support service charges (exclusive of GST) are as follows (SP Services Ltd., 2015):

- Supply of historical consumption data: 40 $ per account per request
- Account closure: 40 $ per account per request

- Confirmation of balance: 4.67 $ per request
- Request for statement of account: 4.67 $ per monthly statement request
- Search fee (for copy of bill): 4.67 $ per copy

References

ABB EV Charging Infrastructure. (2014). *Product Leaflet Electric Vehicle Charging Infrastructure Terra multi-standard DC charging station 23* (Tech. Rep.). Retrieved 2015-11-30, from http://new.abb.com/ev-charging/single-standard/terra-23-c 46

Amiri, M., Esfahanian, M., Hairi-Yazdi, M. R., & Esfahanian, V. (2009, May). Minimization of power losses in hybrid electric vehicles in view of the prolonging of battery life. *Journal of Power Sources*, *190*(2), 372–379. doi: doi.org/10.1016/j.jpowsour.2009.01.072 21

André, M. (2004). The ARTEMIS European driving cycles for measuring car pollutant emissions. *Science of the Total Environment*, *334-335*, 73–84. doi: doi.org/10.1016/j.scitotenv.2004.04.070 45

Barré, A., Deguilhem, B., Grolleau, S., Gérard, M., Suard, F., & Riu, D. (2013, Jun). A review on lithium-ion battery ageing mechanisms and estimations for automotive applications. *Journal of Power Sources*, *241*, 680–689. doi: doi.org/10.1016/j.jpowsour.2013.05.040 39

Bashash, S., Moura, S. J., & Fathy, H. K. (2011). On the aggregate grid load imposed by battery health-conscious charging of plug-in hybrid electric vehicles. *Journal of Power Sources*, *196*(20), 8747–8754. doi: doi.org/10.1016/j.jpowsour.2011.06.025 21

Bashash, S., Moura, S. J., Forman, J. C., & Fathy, H. K. (2011, Jan). Plug-in hybrid electric vehicle charge pattern optimization for energy cost and battery longevity. *Journal of Power Sources*, *196*(1), 541–549. doi: doi.org/10.1016/j.jpowsour.2010.07.001 21

Beale, E. M. L., & Forrest, J. J. H. (1976). Global optimization using special ordered sets. *Mathematical Programming*, *10*(1), 52–69. doi: doi.org/10.1007/BF01580653 79

Beale, E. M. L., & Tomlin, J. A. (1970). Special facilities in a general mathematical programming system for nonconvex problems using ordered sets of variables. In J. Lawrence (Ed.), *Proceedings of the Fifth International Conference on Operational Research* (pp. 447–454). London: Tavistock Publications. 79

Bernhart, W. (2014). The Lithium-Ion Battery Value Chain—Status, Trends and Implications. In *Lithium-ion batteries* (pp. 553–565). Elsevier. doi: doi.org/10.1016/B978-0-444-59513-3.00024-8 21

BMW AG. (2016). *Der BMW i3 - Technische Daten.* Retrieved 2016-12-22, from http://www.bmw.de/dam/brandBM/marketDE/countryDE/newvehicles/allfacts/catalogue/BMW_i3_Katalog.pdf?download.1424447309599.pdf 19, 45

Boyd, S., & Vandenberghe, L. (2004). *Convex Optimization*. Cambridge University Press. 59, 63, 64

Braess, H.-H., & Seiffert, U. (Eds.). (2011). *Vieweg Handbuch Kraftfahrzeugtechnik*. Vieweg+Teubner Verlag. doi: doi.org/10.1007/978-3-8348-8298-1 34, 35

Braithwaite, J. W., Gonzales, A., Nagasubramanian, G., Lucero, S. J., Peebles, D. E., Ohlhausen, J. A., & Cieslak, W. R. (1999, Oct). Corrosion of lithium-ion battery current collectors. *Journal of The Electrochemical Society*, *146*(2), 448–456. doi: doi.org/10.1149/1.1391627 40

Broussely, M., Biensan, P., Bonhomme, F., Blanchard, P., Herreyre, S., Nechev, K., & Staniewicz, R. J. (2005, May). Main aging mechanisms in Li ion batteries. *Journal of power sources*, *146*(1), 90–96. doi: doi.org/10.1016/j.jpowsour.2005.03.172 39

BRUSA Elektronik AG. (2015). *NLG513 - On-Board-Charger.* Retrieved 2015-11-30, from http://www.brusa.eu/en/products/energy/chargers-400-v.html 46

Choi, W., & Manthiram, A. (2006, Jul). Comparison of metal ion dissolutions from lithium ion battery cathodes. *Journal of The Electrochemical Society*, *153*(9), A1760–A1764. doi: doi.org/10.1149/1.2219710 39

Conejo, A. J., Castillo, E., Mínguez, R., & García-Bertrand, R. (2006). *Decomposition Techniques in Mathematical Programming: Engineering and Science Applications*. Springer-Verlag Berlin Heidelberg. 61

Dahn, J. R. (1991, Nov). Phase diagram of Li_xC_6. *Physical Review B*, *44*(17), 9170. doi: doi.org/10.1103/PhysRevB.44.9170 38

Department of Statistics Singapore. (2013). *Yearbook Of Statistics Singapore, 2013* (Tech. Rep.). Singapore: Ministry of Trade and Industry. Retrieved 2015-09-15, from http://www.singstat.gov.sg/publications/publications_and_papers/reference/yearbook_of_stats_2013.html 28

Department of Statistics Singapore. (2015). *Yearbook Of Statistics Singapore, 2015* (Tech. Rep.). Singapore: Ministry of Trade and Industry. Retrieved 2015-09-15, from http://www.singstat.gov.sg/publications/publications-and-papers/reference/yearbook-of-statistics-singapore 28

Energy Market Authority. (2010, Oct). *Introduction to the National Electricity Market of Singapore, Version 6* (Tech. Rep.). Singapore. Retrieved 2016-02-01, from https://www.ema.gov.sg/cmsmedia/Handbook/NEMS_111010.pdf 89, 90, 91

Energy Market Authority. (2014, Jan). *Market Support Services Code* (Tech. Rep.). Singapore. Retrieved 2016-02-01, from https://www.ema.gov.sg/cmsmedia/Licensees/MSS_Code_Jan14.pdf 90

Energy Market Authority. (2015, Oct). *Singapore's Electricity Market & You* (Tech. Rep.). Singapore. Retrieved 2016-02-01, from https://www.ema.gov.sg/Handbook_and%20Educational_Materials.aspx 89

Energy Market Company. (2016a). *Guide To Prices.* Retrieved 2016-02-03, from https://www.emcsg.com/marketdata/guidetoprices 91

Energy Market Company. (2016b). *Price Information.* Retrieved 2016-02-01, from https://www.emcsg.com/marketdata/priceinformation 90, 92, 93, 114

EPA United States Environmental Protection Agency. (2015, Sep). *Dynamometer Drive Schedules.* Retrieved 2015-09-14, from http://www3.epa.gov/nvfel/testing/dynamometer.htm 35

Fischhaber, S., Regett, A., Schuster, S. F., & Hesse, H. (2016). *Studie: Second-Life-Konzepte*

für Lithium-Ionen-Batterien aus Elektrofahrzeugen (Tech. Rep.). Forschungsstelle für Energiewirtschaft e. V.; Lehrstuhl für Elektrische Energiespeichertechnik, Technische Universität München. Retrieved 2016-02-15, from https://www.ffe.de/download/article/620/StudieSecondLifeKonzepte.pdf 88

Floudas, C. A. (1995). *Nonlinear and Mixed-Integer Optimization: Fundamentals and Applications.* Oxford University Press, USA. 61

Fortenbacher, P., Mathieu, J. L., & Andersson, G. (2014, Aug). Modeling, identification, and optimal control of batteries for power system applications. In *2014 Power Systems Computation Conference* (pp. 1–7). IEEE. doi: doi.org/10.1109/PSCC.2014.7038360 23

Goebel, C., Hesse, H., Schimpe, M., Jossen, A., & Jacobsen, H.-A. (2016). Model-based Dispatch Strategies for Lithium-Ion Battery Energy Storage applied to Pay-as-Bid Markets for Secondary Reserve. *IEEE Transactions on Power Systems*, *8950*(c), 1–1. doi: doi.org/10.1109/TPWRS.2016.2626392 24

Gonzalez Vaya, M., & Andersson, G. (2015, Sep). Optimal Bidding Strategy of a Plug-In Electric Vehicle Aggregator in Day-Ahead Electricity Markets Under Uncertainty. *IEEE Transactions on Power Systems*, *30*(5), 2375–2385. doi: doi.org/10.1109/TPWRS.2014.2363159 20

Google. (2015). *Google Maps.* Retrieved 2015-02-05, from http://maps.google.com/ 30

Guenther, C., Schott, B., Hennings, W., Waldowski, P., & Danzer, M. A. (2013, Oct). Model-based investigation of electric vehicle battery aging by means of vehicle-to-grid scenario simulations. *Journal of Power Sources*, *239*, 604–610. doi: doi.org/10.1016/j.jpowsour.2013.02.041 22

Hoke, A., Brissette, A., Maksimović, D., Pratt, A., & Smith, K. (2011). Electric vehicle charge optimization including effects of lithium-ion battery degradation. In *2011 ieee vehicle power and propulsion conference, vppc 2011.* doi: doi.org/10.1109/VPPC.2011.6043046 23

Hoke, A., Brissette, A., Smith, K., Pratt, A., & Maksimovic, D. (2014). Accounting for Lithium-Ion Battery Degradation in Electric Vehicle Charging Optimization. *IEEE Journal of Emerging and Selected Topics in Power Electronics*, *2*(3), 691–700. doi: doi.org/10.1109/JESTPE.2014.2315961 23

Huber, M., Trippe, A., Kuhn, P., & Hamacher, T. (2012, Oct). Effects of Large Scale EV and PV Integration on Power Supply Systems in the Context of Singapore. In *3rd IEEE PES International Conference and Exhibition on Innovative Smart Grid Technologies (ISGT Europe)* (pp. 1–8). Berlin. doi: doi.org/10.1109/ISGTEurope.2012.6465831 32

IBM. (2016). *Parameters of CPLEX: feasibility tolerance.* Retrieved 2016-12-29, from http://www.ibm.com/support/knowledgecenter/SS9UKU_12.4.0/com.ibm.cplex.zos.help/Parameters/topics/EpRHS.html 101

Inland Revenue Authority of Singapore. (2015, Feb). *IRAS e-Tax Guide, GST Guide for the Market Participants in the National Electricity Market of Singapore (NEMS)* (Tech. Rep.). Singapore. Retrieved 2016-02-02, from https://www.iras.gov.sg/irashome/uploadedFiles/IRASHome/e-Tax_Guides/GST_Guide%20for%20the%20market%20participants%20in%20the%20NEMS.pdf 91

Jossen, A., & Weydanz, W. (2006). *Moderne Akkumulatoren richtig einsetzen*. Reichardt

Verlag. 47, 57

Keil, P., Schuster, S. F., Wilhelm, J., Travi, J., Hauser, A., Karl, R. C., & Jossen, A. (2016, Jul). Calendar Aging of Lithium-Ion Batteries. *Journal of The Electrochemical Society*, *163*(9), A1872–A1880. doi: doi.org/10.1149/2.0411609jes 48

Kempton, W., & Tomić, J. (2005a, Jun). Vehicle-to-grid power fundamentals: Calculating capacity and net revenue. *Journal of Power Sources*, *144*(1), 268–279. doi: doi.org/10.1016/j.jpowsour.2004.12.025 21

Kempton, W., & Tomić, J. (2005b, Jun). Vehicle-to-grid power implementation: From stabilizing the grid to supporting large-scale renewable energy. *Journal of Power Sources*, *144*(1), 280–294. doi: doi.org/10.1016/j.jpowsour.2004.12.022 21

Koller, M., Borsche, T., Ulbig, A., & Andersson, G. (2013, Jun). Defining a degradation cost function for optimal control of a battery energy storage system. In *2013 IEEE Grenoble Conference* (pp. 1–6). IEEE. doi: doi.org/10.1109/PTC.2013.6652329 23

Land Transport Authority. (2014a). *Car Population by CC Rating* (Tech. Rep.). Singapore: Customer Services Division. Retrieved 2015-09-21, from `www.lta.gov.sg/content/ltaweb/en/publications-and-research.html` 34

Land Transport Authority. (2014b). *Total Car Population by Make* (Tech. Rep.). Singapore: Customer Services Division. Retrieved 2015-09-21, from `www.lta.gov.sg/content/ltaweb/en/publications-and-research.html` 34

Land Transport Authority. (2015a). *Motor Vehicle Population by Type of Fuel Used* (Tech. Rep.). Singapore: Customer Services Division. Retrieved 2016-12-27, from `www.lta.gov.sg/content/ltaweb/en/publications-and-research.html` 34

Land Transport Authority. (2015b). *Motor Vehicle Population by Vehicle Type* (Tech. Rep.). Singapore: Customer Services Division. Retrieved 2015-09-15, from `www.lta.gov.sg/content/ltaweb/en/publications-and-research.html` 28, 34, 108

Land Transport Authority. (2016). *Taxis: Fares & Payment Methods.* Retrieved 2016-12-28, from `https://www.lta.gov.sg/content/ltaweb/en/public-transport/taxis/fares-and-payment-methods.html` 31

Lehrstuhl für Energiewirtschaft und Anwendungstechnik, Technische Universität München, Jan Vincke. (2013, Oct 25). *Measurements of charging profiles conducted within the project InCharge.* Personal communication. (http://www.smartup.ei.tum.de/en/previous-project-incharge/) 41

Lunz, B., Walz, H., & Sauer, D. U. (2011, Sep). Optimizing vehicle-to-grid charging strategies using genetic algorithms under the consideration of battery aging. In *2011 IEEE Vehicle Power and Propulsion Conference* (pp. 1–7). IEEE. doi: doi.org/10.1109/VPPC.2011.6043021 23

Lunz, B., Yan, Z., Gerschler, J. B., & Sauer, D. U. (2012, Jul). Influence of plug-in hybrid electric vehicle charging strategies on charging and battery degradation costs. *Energy Policy*, *46*, 511–519. doi: doi.org/10.1016/j.enpol.2012.04.017 23

Ma, Z., Callaway, D. S., & Hiskens, I. A. (2013, Jan). Decentralized Charging Control of Large Populations of Plug-in Electric Vehicles. *IEEE Transactions on Control Systems Technology*, *21*(1), 67–78. doi: doi.org/10.1109/TCST.2011.2174059 21

Madhavi, S., Rao, G. S., Chowdari, B., & Li, S. (2001, Aug). Effect of aluminium doping on cathodic behaviour of $LiNi_{0.7}Co_{0.3}O_2$. *Journal of power sources*, *93*(1), 156–162.

doi: doi.org/10.1016/S0378-7753(00)00559-0 39

Marongiu, A., Roscher, M., & Sauer, D. U. (2014). Influence of the vehicle-to-grid strategy on the aging behavior of lithium battery electric vehicles. *Applied Energy*, *137*, 899–912. doi: doi.org/10.1016/j.apenergy.2014.06.063 22

Ministry Of Manpower. (2013). *Singapore Yearbook of Manpower Statistics, 2013* (Tech. Rep.). Singapore: Manpower Research and Statistics Department. Retrieved 2015-09-15, from http://stats.mom.gov.sg/Pages/Singapore-Yearbook-Of-Manpower-Statistics-2013.aspx 28

Misener, R., & Floudas, C. A. (2010). Piecewise-linear approximations of multidimensional functions. *Journal of Optimization Theory and Applications*, *145*(1), 120–147. doi: http://dx.doi.org/10.1007/s10957-009-9626-0 79

Moecker, S. (2014). *Driving Profile and Energy Demand Analysis for Electrical Vehicles based on GPS Trajectories* (Master's thesis, Technische Universität München). Retrieved 2015-08-13, from https://mediatum.ub.tum.de/node?id=1254546 30, 35

Monetary Authority of Singapore. (2016). *Exchange Rates.* Retrieved 2016-04-22, from https://secure.mas.gov.sg/msb/ExchangeRates.aspx 88

Nykvist, B., & Nilsson, M. (2015, Mar). Rapidly falling costs of battery packs for electric vehicles. *Nature Climate Change*, *5*(4), 329–332. doi: doi.org/10.1038/nclimate2564 19, 88

Padhi, A. K., Nanjundaswamy, K. S., & Goodenough, J. B. (1997, Apr). Phospho-olivines as positive-electrode materials for rechargeable lithium batteries. *Journal of the electrochemical society*, *144*(4), 1188–1194. doi: doi.org/10.1149/1.1837571 39

Pan, C.-c., Banks, C. E., Song, W.-x., Wang, C.-w., Chen, Q.-y., & Ji, X.-b. (2013, Dec). Recent development of $LiNi_xCo_yMn_zO_2$: Impact of micro/nano structures for imparting improvements in lithium batteries. *Transactions of Nonferrous Metals Society of China*, *23*(1), 108–119. doi: doi.org/10.1016/S1003-6326(13)62436-X 39

Peabody, C., & Arnold, C. B. (2011, Oct). The role of mechanically induced separator creep in lithium-ion battery capacity fade. *Journal of Power Sources*, *196*, 8147-8153. doi: doi.org/10.1016/j.jpowsour.2011.05.023 40

Pillot, C. (2015). Battery Market Development for Consumer Electronics, Automotive, and Industrial: Materials Requirements and Trends. In *5th Israeli Power Sources Conference* (pp. 1–40). Herzelia. 19, 21, 88

Plötz, P., Gnann, T., Kühn, A., & Wietschel, M. (2014). *Markthochlaufszenarien für Elektrofahrzeuge* (Tech. Rep.). Fraunhofer ISI. Retrieved 2016-04-22, from http://www.isi.fraunhofer.de/isi-wAssets/docs/e/de/publikationen/Fraunhofer-ISI-Markthochlaufszenarien-Elektrofahrzeuge-Langfassung.pdf 88

Quantum Inventions. (2012). *Singapore Live Traffic.* Retrieved 2012-06-06, from www.livetraffic.sg 32, 33

Recalde Melo, D., Trippe, A., Gooi, H. B., & Massier, T. (2016). Robust electric vehicle aggregation for ancillary service provision considering battery aging. *IEEE Transactions on Smart Grid*, *PP*(99), 1–11. doi: doi.org/10.1109/TSG.2016.2598851 114, 115

SAE International. (2012). *Battery Electric Vehicle Energy Consumption and Range Test*

Procedure (No. SAE J 1634). Retrieved 2015-09-23, from http://standards.sae.org/j1634_201210/ 35

Safari, M., & Delacourt, C. (2011, Aug). Aging of a commercial graphite/$LiFePO_4$ cell. *Journal of The Electrochemical Society*, *158*(10), A1123–A1135. doi: doi.org/10.1149/1.3614529 40

Samsung SDI Co., Ltd. (2008, Aug). *Specification of Product for Lithium-ion Rechargeable Cell Model : ICR18650-22FM* (Tech. Rep.). Battery Business Division. 40, 54

Schuster, S. F., Bach, T., Fleder, E., Müller, J., Brand, M., Sextl, G., & Jossen, A. (2015, Jun). Nonlinear aging characteristics of lithium-ion cells under different operational conditions. *Journal of Energy Storage*, *1*(1), 44–53. doi: doi.org/10.1016/j.est.2015.05.003 89

Scrosati, B., & Garche, J. (2010, Nov). Lithium batteries: Status, prospects and future. *Journal of Power Sources*, *195*(9), 2419–2430. doi: doi.org/10.1016/j.jpowsour.2009.11.048 22

Sherali, H. D., & Adams, W. P. (1994, Jul). A hierarchy of relaxations and convex hull characterizations for mixed-integer zero—one programming problems. *Discrete Applied Mathematics*, *52*(1), 83–106. doi: doi.org/10.1016/0166-218X(92)00190-W 72

Sortomme, E., & El-Sharkawi, M. A. (2011, Mar). Optimal Charging Strategies for Unidirectional Vehicle-to-Grid. *IEEE Transactions on Smart Grid*, *2*(1), 131–138. doi: doi.org/10.1109/TSG.2010.2090910 20

Sortomme, E., & El-Sharkawi, M. A. (2012, Mar). Optimal Scheduling of Vehicle-to-Grid Energy and Ancillary Services. *IEEE Transactions on Smart Grid*, *3*(1), 351–359. doi: doi.org/10.1109/TSG.2011.2164099 21

SP PowerAssets Ltd. (2015, Apr). *Transmission Service Rate Schedule* (Tech. Rep.). Singapore. Retrieved 2016-02-02, from http://www.singaporepower.com.sg/irj/go/km/docs/wpccontent/Sites/SP%20PowerGrid/Site%20Content/Resources/documents/trans-service-rate-schedule.pdf 90, 125

SP Services Ltd. (2014). *Transmission Loss Factors.* Retrieved 2016-02-24, from https://www.mypower.com.sg/About/Transmission_Loss_Factors.html 92

SP Services Ltd. (2015). *Schedule of Market Support Service ("MSS") Charges for Contestable Consumers with Advanced Metering Infrastructure ("AMI") Electricity Meter* (Tech. Rep.). Singapore. Retrieved 2016-02-03, from https://www.mypower.com.sg/About/MSS_Charges.html 90, 125

Sundstrom, O., & Binding, C. (2012, Mar). Flexible Charging Optimization for Electric Vehicles Considering Distribution Grid Constraints. *IEEE Transactions on Smart Grid*, *3*(1), 26–37. doi: doi.org/10.1109/TSG.2011.2168431 20

The MathWorks, Inc. (2014). *MATLAB Release 2014a.* Natick, Massachusetts, United States. 27

Trippe, A. E., Arunachala, R., Massier, T., Jossen, A., & Hamacher, T. (2014). Charging Optimization of Battery Electric Vehicles including Cycle Battery Aging. In *IEEE PES Innovative Smart Grid Technologies Conference Europe (ISGT-Europe)* (pp. 1–6). Istanbul. doi: doi.org/10.1109/ISGTEurope.2014.7028735 41, 64, 117

Trippe, A. E., Lopez Hidalgo, P., Lienkamp, M., & Hamacher, T. (2015, Sep). Mobility Model for the Estimation of the Spatiotemporal Energy Demand of Battery Electric

Vehicles in Singapore. In *IEEE 18th International Conference on Intelligent Transportation Systems* (pp. 578–583). Gran Canaria, Spain. doi: doi.org/10.1109/ITSC.2015.10127

Urban Redevelopment Authority. (2015). *URA Maps.* Retrieved 2015-09-16, from `https://www.ura.gov.sg/uramaps/?config=config_preopen.xml&preopen=PlanningBoundaries&pbIndex=1` 28

USABC, & DOE National Laboratories. (1996). *Electric Vehicle Battery Test Procedures Manual – Revision 2* (Tech. Rep.). Retrieved 2016-02-15, from `https://avt.inl.gov/sites/default/files/pdf/battery/usabc{_}manual{_}rev2.pdf` 88

Vetter, J., Novák, P., Wagner, M., Veit, C., Möller, K.-C., Besenhard, J., ... Hammouche, A. (2005, Mar). Ageing mechanisms in lithium-ion batteries. *Journal of Power Sources*, *147*(1–2), 269–281. doi: doi.org/10.1016/j.jpowsour.2005.01.006 39

Waraich, R. A., Galus, M. D., Dobler, C., Balmer, M., Andersson, G., & Axhausen, K. W. (2013, Mar). Plug-in hybrid electric vehicles and smart grids: Investigations based on a microsimulation. *Transportation Research Part C: Emerging Technologies*, *28*, 74–86. doi: doi.org/10.1016/j.trc.2012.10.011 21

Xu, K., Ding, S. P., & Jow, T. R. (1999, Jul). Toward reliable values of electrochemical stability limits for electrolytes. *Journal of The Electrochemical Society*, *146*(11), 4172–4178. doi: doi.org/10.1149/1.1392609 39